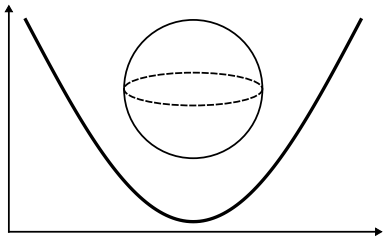

Aspects of decoherence in superconductor-semiconductor qubits

PhD thesis. Oscar Erlandsson, 2022.

Center for Quantum Devices, Niels Bohr Institute, University of Copenhagen.

Academic advisor: Charles M. Marcus

This thesis has been submitted to the
PhD School of The Faculty of Science, University of Copenhagen

Abstract

Hybrid superconductor-semiconductor devices offer unique advantages for solid-state quantum information processing. In particular, the gatemon qubit has proved to be a versatile experimental platform since its inception less than a decade ago. For all types of qubits, understanding and overcoming decoherence are important parts of the progression toward large-scale quantum computation. In this thesis, results from three different studies related to decoherence in gatemons are presented.

First, a gatemon formed in an InAs nanowire with a fully covering Al shell is studied in a finite magnetic field. Investigating this system in an applied field is motivated by the possible existence of Majorana zero modes, which could be used for protection against decoherence. A non-monotonic dependence of the qubit transition frequency on magnetic field is observed and interpreted as the destructive Little-Parks effect. No signature of finite Majorana coupling (E_M) is observed. By measuring the charge dispersion of the qubit, an upper bound is placed at $E_M/h < 10\,\mathrm{MHz}$.

Next, parity switching induced by quasiparticles in the nanowire gatemon is studied. Quasiparticle poisoning can lead to decoherence and is an important source of loss in superconducting qubits. At zero magnetic field, the switching is found to occur on a time scale of 100 ms. As either the temperature or magnetic field is increased, the switching rate is observed to be first constant and then increase exponentially, which is consistent with the conventional picture of coexisting non-equilibrium and thermal quasiparticles. Slow parity switching at zero magnetic field is promising for future development of gatemon coherence times.

Finally, early results from the study of a 2DEG-based gatemon with multiple gates close to the Josephson junction are presented. Precise gate control of the

potential could allow for novel ways to limit decoherence. Operation of multiple gates is demonstrated in both transport and circuit-QED measurements. The devices are found to have short relaxation times on the order of 0.1 μs. Directions for future research are discussed.

Resume

Hybrid superleder-halvleder devices har unikke fordele ved brug til solid-state kvante informations processering. I særdeleshed har "gatemon" kvantebit vist sig at være en versatil eksperimentel platform siden dens første demonstration for mindre end 10 år siden. For alle typer af qubits er det centralt at forstå dekohærens-mekanismer for at kunne udvikle dem frem i mod en stor-skala kvantecomputer. Denne phd omhandler 3 forskellige studier som omhandler dekohærens i gatemon qubits.

Det første studie omhandler en gatemon realiseret ved brug af en InAs nanowire som er fuldt dækket af en alumunium med et påtrykt magnet felt. Dette system blev studeret på grund af muligheden for at realisere majorana zero modes, som kan bruges til at beskytte imod dekohærens. Vi observerede en ikke-monoton afhængighed af qubit frekvensen som funktion af det eksternt påtrykte felt, en effekt der kunne tilskrives den destruktive Little-Parks effekt. Vi fandt ingen tegn på Majorana koblingen (E_M) i systemet. Ved at måle qubittens ladnings-dispersion kunne vi upper-bounde E_M koblingen til at være $E_M/h < 10\,\mathrm{MHz}$.

Det andet studie omhandlede paritets-skift induceret af kvasipartikler i en nanowire gatemon. Kvasipartikel forstyrrelse kan lede til dekohærens og er en vigtig kilde til informations-tab i superledende kvantebits. Ved 0 magnet felt er paritets-skifte-tiden på en tidsskala af 100 ms. Hvis enten temperaturen eller magnetfeltet øges observeres at tidsskalaen først er konstant, men senere stiger eksponentielt, konsistent med en konventiel fortolkning af sameksistent af ikke-ækvilibrium og termiske kvasipartikler. Langsom paritets-skift tid ved 0 magnet felt er en vigtig ingrediens for fremtidige udviklinger i gatemon kohærens tider.

Slutteligt præsenteres tidlige resultater på en gatemon realiseret ved hjælp af to-dimensionel elektrongas, hvor adskillige elektrostatiske gates overlapper med Josephson junction. Præcis gate-kontrol af potentialet i Josephson junction kan

lede til nye metoder til at begrænse kohærensen i den resulterende gatemon qubit. Der demonstreres både transport- og circuit-QED målinger på dette device. Devices som dette viste sig at have kort relaxation tider, i størrelsesordenen $0.1\,\mu s$. Slutteligt diskuteres fremtidige forskningsretninger relateret til dette projekt.

List of publications

This thesis covers the following publications

1. "Destructive Little-Parks effect in a full-shell nanowire-based transmon" (2020) by D. Sabonis*, **O. Erlandsson***, A. Kringhøj*, B. van Heck, T. W. Larsen, I. Petkovic, P. Krogstrup, K. D. Petersson, C. M. Marcus. *Physical Review Letters*, 125(15):156804.
   * These authors contributed equally to this work.

2. "Parity switching in a full-shell superconductor-semiconductor nanowire qubit" (in review) by **O. Erlandsson***, D. Sabonis*, A. Kringhøj, T. W. Larsen, P. Krogstrup, K. D. Petersson, C. M. Marcus. *arXiv:2202.05974*, 2022.
   * These authors contributed equally to this work.

The present PhD project also contributed to the following publications, which are not covered by this thesis,

3. "Controlled dc monitoring of a superconducting qubit" (2020) by A. Kringhøj, T. W. Larsen, B. van Heck, D. Sabonis, **O. Erlandsson**, I. Petkovic, D. I. Pikulin, P. Krogstrup, K. D. Petersson, C. M. Marcus. *Physical Review Letters*, 124(5):056801.

4. "Suppressed charge dispersion via resonant tunneling in a single-channel transmon" (2020) by A. Kringhøj, B. van Heck, T. W. Larsen, **O. Erlandsson**, D. Sabonis, P. Krogstrup, L. Casparis, K. D. Petersson, C. M. Marcus. *Physical Review Letters*, 124(24):246803.

5. "Andreev modes from phase winding in a full-shell nanowire-based transmon" (2021) by A. Kringhøj, G. W. Winkler, T. W. Larsen,

D. Sabonis, **O. Erlandsson**, P. Krogstrup, B. van Heck, K. D. Petersson, C. M. Marcus. *Physical Review Letters*, 126(4):047701.

6. "Magnetic-field-compatible superconducting transmon qubit" (2021) by A. Kringhøj*, T. W. Larsen*, **O. Erlandsson**, W Uilhoorn, J. G. Kroll, M. Hesselberg, R. P. G. McNeil, P. Krogstrup, L. Casparis, C. M. Marcus. K. D. Petersson. *Physical Review Applied*, 15(5):054001.
   * These authors contributed equally to this work.

7. "Few-mode to mesoscopic junctions in gatemon qubits" (in review) by A. Danilenko*, D. Sabonis*, G. W. Winkler, **O. Erlandsson**, P. Krogstrup, C. M. Marcus. *arXiv:2209.03688*, 2022.
   * These authors contributed equally to this work.

Acknowledgements

There are many people who helped to make this thesis possible. I would first like to thank my advisor Charles Marcus for providing me with the opportunity to do my PhD project at the Center for Quantum Devices. Throughout my years at QDev, your supervision and physics expertise have been guiding me along my research. Among many things, I have learned from you to embrace an eagerness to discover the truth.

Morten Kjaergaard, you entered as a co-supervisor midway through my time as a PhD student. I learned a great amount from you about the hard and soft skills related to the field of experimental quantum information. In the earlier parts of my PhD project, Karl Petersson had a supervisory role. Karl, I was always inspired by your intelligence and attention to detail.

In the beginning of my time at QDev, I was fortunate to receive mentorship from Lucas Casparis, Anders Kringhøj and Thorvald Larsen, all being great role models in the lab. Deividas Sabonis, we worked together on the projects that ended up forming the core of this thesis. The time we spent together at the dilution refrigerator was among the most defining and enjoyable parts of my PhD project.

Many other collaborators and colleagues have been important to me as a PhD student. To name a few, José Manuel Chávez-Garcia, Alisa Danilenko, Asbjørn Drachmann, Michaela Eichinger, Kian Gao, Andreas Pöschl and Zhenhai Sun, you have all been a source of valueable knowledge and inspiration. In addition to people I have worked directly with, I have also benefited from interactions with many other colleagues, including office mates, lab duty partners, fellow teaching assistants, classmates and beyond, together forming a great environment in which to work and do research.

I enjoyed my experience with teaching and supervising students. As a teach-

ing assistant, I wish to thank all the students in my class for sparking interesting thoughts and showing patience with my slow explanations. In addition, I would like to extend a special thanks to Kim Splittorff in whose quantum mechanics class I had the opportunity to be a TA. I admire your approach to teaching physics. During my PhD project I had the chance to help supervise Amalie Faber Mygind for her Bachelor's thesis and Sofus Budtz for his Master's thesis. I greatly enjoyed both experiences and I can only hope you learned as much as I did from our work together.

For assistance related to the subtle and non-subtle arts of nanofabrication, I wish to thank Sangeeth Kallatt, Robert McNeil, Karolis Parfeniukas and Smitha Nair Themadath. Finally, I would like to thank the group of people at the Quantum Optics section with whom I interacted toward the end of my PhD project. I had a great experience discussing the role of our research in society with all of you.

Contents

List of Figures

The cover image depicts a Bloch sphere on top of a non-sinusoidal function.

Acronyms

- **2DEG** two-dimensional electron gas
- **ALD** atomic layer deposition
- **BCS** Bardeen Cooper Schrieffer
- **circuit-QED** circuit quantum electrodynamics
- **DAC** digital-to-analog converter
- **dc** direct current
- **DMM** digital multimeter
- **DOS** density of states
- **DUT** device under test
- **JJ** Josephson junction
- **MBE** molecular beam epitaxy
- **MZM** Majorana zero mode
- **PCB** printed circuit board
- **PSD** power spectral density
- **QP** quasiparticle
- **QPP** quasiparticle poisoning
- **RF** radio frequency
- **TEM** transmission electron microscopy
- **TWPA** traveling-wave parametric amplifier
- **VNA** vector network analyzer
- **VLS** vapor–liquid–solid

Chapter 1

Introduction

The relationship between humankind and technology is profound and multi-faceted. In the 20th century, the development of semiconductor devices such as the transistor has faciliated the rise of information technology, greatly impacting many parts of human societies. Moore's law describes the persistent ability to make smaller and smaller transistors, allowing for the construction of more powerful computers. A parallel development of human knowledge in the 20th century was the gradual discovery of quantum mechanics as a physical description of nature. In quantum mechanics, the behavior of particles are described by simple but sometimes counter-intuitive principles. For example, an electron can exist in a superposition of states, collapsing into a determined state only upon observation.

More recently, information technology and quantum mechanics have crossed paths. This can be seen as an inevitable consequence of transistor miniaturization reaching the domain where quantum mechanical descriptions are necessary. Seen from another perspective, there is no reason to limit the hardware of computers to effects that can be described by classical physics. The idea of a quantum computer was first introduced in the 1980s by physicist R. Feynman [1]. Since then, it has gone from an idea to an industry of research and development, spanning both academia and the private sector. Theory has showed that in some cases, quantum mechanical effects can provide exponential improvements to the speed of computation. If a universal quantum computer was realized to harness this exponential power, problems impossible to solve using classical computers could suddenly become solvable. The fundamental building block of a quantum

computer is called a quantum bit, or *qubit* for short. Similar to an electron, it exists in a superposition of 0 and 1 until its state is observed. As the research has progressed, devices with an increasing number of qubits have been manufactured. While a universal quantum computer has not yet been constructed, each breakthrough brings the dream closer to reality.

In general, technology offers a plethora of benefits to society, such as uses in communication, health care, industry, science and entertainment. On the other hand, it has also been used in warfare, mass surveillance and to promote unjustified concentrations of power. The impact on human lives is not inherent in the technology itself but is determined by the way in which it is used. These general observations apply also to quantum computers and highlights the importance of considering the role of research in society. An example of a questionable direction of technology development is the recent announcement by the Niels Bohr Institute of its plans to collaborate with a military alliance regarding quantum research [2]. It could be argued that this instance is part of a broader worrisome trend in decision-making at University of Copenhagen [3].

In summary, the development of quantum technology and the pursuit of universal quantum computation is a scientific challenge that may offer new insights into nature and benefits to people's lives. Like other collective undertakings, the success of the project and the extent to which it is used for the common good is determined by the people involved in the effort.

Many physical platforms have been considered for quantum computers, such as trapped ions, photons and superconducting circuits. This PhD thesis focuses on a specific variant of the latter, namely a superconductor-semiconductor hybrid qubit known as the *gatemon*. Three experiments related to the preservation of quantum information in the gatemon are discussed. The loss of quantum information to the surrounding environment is referred to as decoherence of the qubit. Hopefully, the results presented here sheds light on how to overcome decoherence in gatemons and contribute to the development of quantum technology.

Chapter 2

Background

In this chapter, theory and previous experiments are reviewed that form the background for subsequent chapters. The chapter starts with a brief overview of the basic solid-state physics of the types materials that play a central role for the thesis. It is then described how superconductors have been used as a platform for quantum computation. Mechanisms of decoherence and their visualization on the Bloch sphere is discussed. This is followed by an examination of the consequences of incorporating a semiconductor into a transmon qubit. The chapter concludes with a short description of Majorana zero modes.

2.1 Semiconductor and superconductor

Solid-state physics describes the behavior of electrons in crystals and how the crystal properties determine the type of material [4]. In particular, the electric properties of a material are governed by the conditions for transporting charged particles across it. The physical description of this is captured by the electronic density of states (DOS) in the material, illustrated in Figure 2.1. Finite density of states is associated with the conduction of electric currents because electrons, the charged particles that carry the current, need to occupy quantum mechanically available states as they propagate through the material.

Metals are crystals in which electrons (crystal quasiparticles with charge $1e$) have a finite DOS as depicted in Figure 2.1a, making them conductors of electric currents. In semiconductors (Figure 2.1b) the presence of a band gap in the DOS means that the device can act both as a conductor and an insulator, control-

lable by external conditions such as temperature and an applied electric field. At low temperatures, some metals enter into a superconducting state. This state of matter was discovered in the early 20th century and is associated with electric currents with zero resistance. A microscopic theory of the phenomenon was discovered decades later and is known as Bardeen Cooper Schrieffer (BCS) theory. Similar to semiconductors, the superconducting state is also associated with a gap in the quasiparticle DOS (Figure 2.1c), although the underlying physics is different. In superconductors, electrons can condensate into Cooper pairs with charge $2e$ and the energy cost to break such a pair forms the DOS gap. Cooper pairs form a macroscopic quantum state and enable the dissipationless flow of a supercurrent.

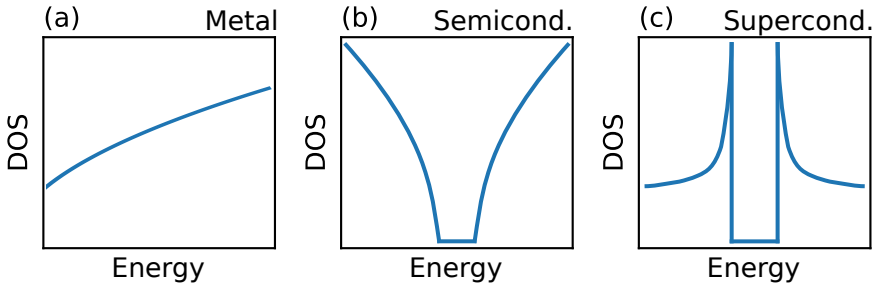

Figure 2.1: Quasiparticle density of states in three different types of materials. Qualitative illustration of the density of states for quasiparticles with charge $1e$ in a (a) metal, (b) semiconductor and (c) superconductor.

A structure with two superconductors separated by a non-superconductor is known as a Josephson junction (JJ) [5]. The non-superconducting element is called a weak link and is typically an insulator. Despite the weak link, this type of junction supports a supercurrent $I = I_c \sin\phi$, where I_c is a critical current and ϕ is the quantum mechanical phase difference between the two superconductors. The possibility of a supercurrent through a JJ can be thought of as resulting from a proximity effect whereby the superconducting state extends beyond its physical boundary. The proximity effect also enables a non-superconductor running parallel to the superconductor to support a supercurrent.

2.2 Superconducting circuit and qubit

Due to the dissipationless nature of currents associated with the superconducting state, superconducting circuits provide a suitable platform for quantum computation [6, 7]. Superconductors form one of the most prominent types of qubits, for example having been used to outperform a classical computer [8]. Many types of superconducting qubits exist, utilizing different degrees of freedom to define the qubit and operating in distinct regimes of parameter space.

One of the simplest possible superconducting circuits to consider is an inductor-capacitor circuit. The quantization of the expression for the energy stored in such a circuit leads to a Hamiltonian equivalent to the harmonic oscillator. While such an element is interesting (and serves as a model of superconducting resonators used in this thesis), the operation of superconducting qubits relies on finite anharmonicity, i.e. unevenly separated energy levels. This is required because in order to use the ground and excited state as a two-level system (qubit) the transition between these levels must be uniquely addressable. Replacing the inductor with a Josephson junction as described above serves to provide a non-linearity to the circuit, which produces an anharmonic oscillator. This system is described by the Hamiltonian [7]

$$\hat{H}_T = 4E_C(\hat{n} - n_g)^2 - E_J \cos(\hat{\phi}) \tag{2.1}$$

where $E_C = e^2/2C$ is the charging energy given by the capacitance across the JJ, $\hat{n}$ is the number operator corresponding to the difference in Cooper pairs between either side of the JJ, n_g is an effective offset charge accounting for all other charges affecting the potential, and $E_J = \hbar I_c/2e$ is the Josephson energy. The first two energy levels of $\hat{H}_T$ are plotted in Figure 2.2. Throughout this thesis, the frequency $(E_1 - E_0)/h$ corresponding to the transition between the ground and excited state is denoted by f_{01}. The first implementations of a qubit based on this Hamiltonian went by the name Cooper pair box and had a level spectrum similar to Figure 2.2a [9, 10]. A drastic improvement of qubit performance was achieved by operating the system at an increased ratio E_J/E_C as in Figure 2.2b-c [11]. The improvment in performance is due to suppressing the influence of charge noise on qubit coherence. Superconducting charge qubits operated around or above $E_J/E_C \sim 50$ are known as transmons.

In order to use a qubit for information processing, methods to manipulate and read out its state need to be implemented. For superconducting qubits, the dominating framework to this end is circuit-QED, where information about the state of

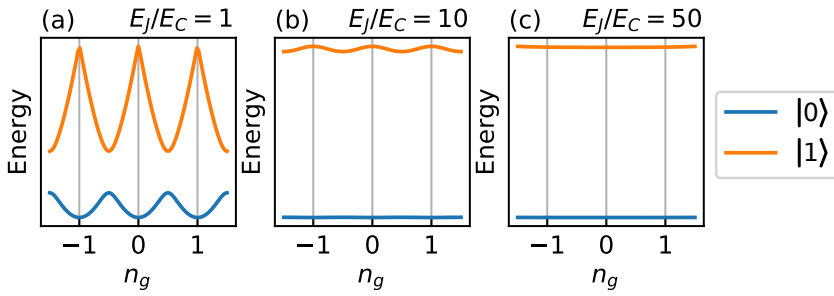

Figure 2.2: Energy level solutions for the transmon Hamiltonian. Panels show the dispersion of the ground and first excited state of the transmon in the effective offset charge n_g, for different values of the ratio E_J/E_C. (a) Cooper pair box regime, (b) offset-charge sensitive transmon regime and (c) conventional transmon regime. Figure inspired by Reference [11].

the qubit is obtained via the microwave transmission of a readout resonator [12]. Similar to an atom interacting with light in a reflective cavity, the interaction between the qubit and the resonator is governed by the Jaynes-Cummings Hamiltonian. By operating the qubit far away from the resonator (dispersive regime) the resonator frequency is shifted from its bare value and the magnitude of this shift depends both on the qubit frequency and its state [13]. Due to this qubit-state-dependent shift of the resonator frequency, readout of the qubit can be achieved by probing the transmission of microwave radiation through the resonator. In practice, readout resonators are often implemented as coplanar waveguides fabricated on the same sample as the qubit, or as a three-dimensional cavity.

2.3 Decoherence

The processing of a quantum computer is conventionally described as a sequence of gates acting on one or more qubits corresponding to the execution of an algorithm [14]. In this picture, the performance of the quantum computer is limited by the number of qubits available, the fidelity of the gates being used, as well as the degree to which individual qubits remain in the computational state prescribed by the algorithm. This last aspect is known as preserving the single-qubit coherence and represents a scientific challenge for any platform for quantum computation, including superconducting circuits [15].

The general state of a single qubit is a complex superposition of the ground state $|0\rangle$ and the excited state $|1\rangle$. A given qubit state can be visualized as a point on the Bloch sphere, as illustrated in Figure 2.3a. Loss of coherence represents uncontrolled movement on the Bloch sphere. This can happen via two principal mehanisms [7]. First, loss of energy from the qubit to the surrounding environment can cause a transition $|1\rangle \rightarrow |0\rangle$ shown in Figure 2.3b. The time scale on which this happens is called the relaxation time T_1. Second, noise in the parameters of the Hamiltonian results in fluctuations of f_{01} which randomizes the phase of the qubit as given by the azimuthal angle ϕ on the Bloch sphere. The time scale associated with this is called the dephasing time T_ϕ (Figure 2.3c). A combined quantity taking into account both energy relaxation and dephasing is called the coherence time T_2, defined by $1/T_2 = 1/(2T_1) + 1/T_\phi$. If pure dephasing is eliminated, the maximum coherence time is given by $T_2 \leq 2T_1$. Taken together, these mechanisms of quantum information loss suggest that to achieve a coherent qubit, it should be isolated from the environment and shielded from any noise. On the other hand, in order to apply gates and read out the qubit state, interaction between the qubit and laboratory equipment is necessary. Establishing the right compromise between these requirements define a significant part of the journey toward full-scale quantum computation.

In the context of superconducting qubits and circuit-QED, sequences of microwave pulses are used to probe a qubit for its T_1 and T_2 values, shown in Figure 2.3d-f. The practical details of implementing such an experiment is described in Section 3.3. A characterization of coherence time scales typically starts with a Rabi sequence (Figure 2.3d). Here, a drive pulse with frequency $f_d = f_{01}$ and of variable duration t_d induces oscillations of the qubit state between $|0\rangle$ and $|1\rangle$, which are recorded by a drive tone at a frequency f_{RO} close to the readout resonator f_R. As the state of the qubit is read out, it collapses into either $|0\rangle$ or $|1\rangle$ with probabilities $\cos\theta/2$ and $\sin\theta/2$, respectively. The average of repeated measurements reveal the oscillatory evolution of the quantum state resulting from the drive tone. Observing these Rabi oscillations is often taken as the condition for having realized a qubit and by inspecting the oscillation period, pulses that induce specific longitudinal movements on the Bloch sphere can be calibrated. In Figure 2.3c such a pulse with length t_π is used to excite the qubit. By varying the time t_w between excitation and readout, T_1 is determined by an exponential fit to averaged measurements. To measure T_2, two pulses with length $t_{\pi/2}$ and a variable separation t_w are used, as shown in Figure 2.3f. This is

known as a Ramsey sequence. The first pulse places the qubit state on the Bloch sphere equator, where it precesses due to its quantum mechanical time evolution, producing oscillations in the averaged measurements. Dephasing and energy relaxation cause the suppression of these oscillations and T_2 is extracted by a fit to an exponentially damped cosine function.

2.4 Superconductor–semiconductor qubit

The experiments in this thesis exclusively study superconductor-semiconductor qubits, where a semiconductor is used as the weak link in the JJ. The nature of a transmon qubit incorporating a semiconductor is altered in a number of ways. The current-phase relationship is no longer given by the sinusoidal Josephson relation but is governed by a small number of sub-gap energy levels. In the short-junction limit, the associated Josephson potential can be approximated by [17]

$$V(\phi) = -\Delta \sum_{\eta} \sqrt{1 - \eta \sin^2(\phi/2)} \tag{2.2}$$

where the sum is over channels with transparency η. These levels are called Andreev states and arise due to the possibility of an electron entering the superconductor as a Cooper pair, by being reflected as a hole, leading to bound states. In a superconductor-semiconductor qubit, the current-phase relationship in Equation 2.2 replaces the second term of the Hamiltonian in Equation 2.1. Using perturbation theory with a fourth-order series expansion of $V(\phi)$ (see e.g. References [18, 19]) yields approximate expressions for the transition frequency

$$hf_{01} \approx \sqrt{8E_C E_J} - E_C \left(1 - \frac{3}{4}\frac{\sum \eta^2}{\sum \eta}\right) \tag{2.3}$$

where

$$E_J = \frac{\Delta}{4} \sum \eta \tag{2.4}$$

and the anharmonicity (defined as $\alpha = E_{12} - E_{01}$)

$$\alpha \approx -E_C \left(1 - \frac{3}{4}\frac{\sum \eta^2}{\sum \eta}\right) . \tag{2.5}$$

The semiconductor field effect provides the ability of using a gate voltage to increase the carrier concentration of the semiconducting weak link, corresponding

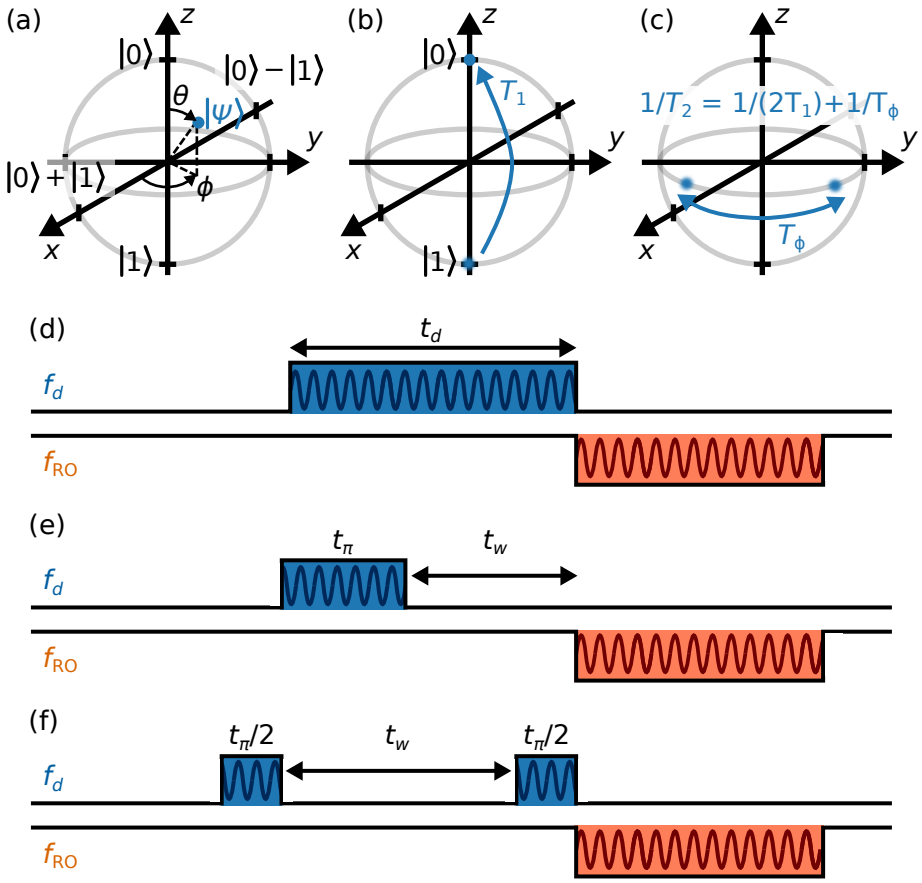

Figure 2.3: Time scales of decoherence and pulse sequences for their experimental determination. (a) The state $\Psi = \cos(\theta/2)\,|0\rangle + \exp(i\phi)\sin(\theta/2)\,|1\rangle$ indicated on the Bloch sphere. Visual representation of (b) energy relaxation and (c) dephasing, as well as the relation between T_ϕ, T_1 and T_2. (d) Rabi pulse sequence used for inducing oscillations between $|0\rangle$ and $|1\rangle$. (e) Relaxation sequence used to determine T_1 and (f) Ramsey sequence for determining T_2. Figure partially adapted from Reference [16] and inspired by Reference [7].

to increasing the number of channels and their transmissions in Equations 2.2 through 2.4. This means that in the superconductor-semiconductor transmon, both f_{01} and α can be altered using a gate, giving rise to the term "gatemon" for

this type of qubit. Experiments have shown that the channel transmissions often increase non-monotonically with gate voltage [20] and that a small number of channels with high transmissions can be expected in a nanowire gatemon [21].

Since initial demonstrations of gatemons in qubits formed in nanowires (NWs) less than a decade ago [22, 23] experimental progress has been remarkable [17], including the implementation of two-qubit gates [24] and characterization of coherence as a function of magnetic field [25]. Gatemons have been implemented in a two-dimensional electron gas [26] and in graphene [27]. Superconductor-semiconductor JJs in NW have been used to provide a tunable coupling between qubits [28]. The special current-phase relationship of gatemons have been leveraged to suppress charge disperion [29,30] and to construct a protected qubit [31]. By adding an extra JJ to the gatemon, *in situ* transport measurements have been incorporated into the circuit-QED architecture [32]. NW gatemons have been operated at magnetic fields as high as 1 T [33]. Furthermore, superconductor-semiconductor junctions have been used to study Andreev bound states [34, 35]. By taking advantage of the spin-orbit interaction in the NWs, they have enabled circuit-QED monitoring of quasiparticle spin [36].

Although the experiments described above have produced interesting insights into the nature of the superconductor-semiconductor JJ, gatemon T_1 remain on the order of $\sim 10\,\mu$s, while other types of superconducting qubits have approached $T_1 \sim 1\,$ms [37]. The usefulness of superconductor-semiconductor hybrids in quantum technology will require developing the gatemon coherence time or establishing niche roles involving gate tunability or the non-sinusoidal current-phase relationship.

2.5 Majorana zero modes

Some experiments described in this thesis are partially motivated by the prospects of a framework for quantum computation known as topological quantum computation (TQC) [38]. This framework has yet to be realized but could potentially offer powerful protection against decoherence. The scheme for achieving TQC relevant to the present thesis is the manipulation of Majorana zero modes (MZMs) in nanowires [39]. This scheme is based around mapping a toy model known as the Kitaev chain [40] to an *s*-wave superconductor proximitizing a semiconductor [41, 42].

Experiments using dc transport measurements have reported signatures com-

patible with MZMs in the same type of NWs used for the experiments in this thesis [43–45], although the question of whether MZMs exist and could be reliably produced in these systems remains unsettled. Theoretical proposals have indicated the possibility of interacting with MZMs in the microwave regime [46] as well as integrating MZMs into superconducting qubit architectures [47–51]. In Chapter 4 of the present thesis, circuit-QED measurements are used to search for a particular signature of MZMs.

Chapter 3

Experimental platforms

This chapter describes the implementation of the concepts introduced in Chapter 2, that will be used in the experiments described in subsequent chapters. The experiments feature qubits using two different realizations of the Josephson junction, namely the nanowire and the two-dimensional electron gas. The fabrication used to incorporate the Josephson junctions into a circuit-QED architecture for qubit control and readout is described. Finally, the experimental setup in which microwave and dc transport measurements are performed is discussed.

3.1 Vapor-liquid-solid nanowire gatemon

Nanowires (NWs) are nanotechnology components in the shape of a wire with a diameter on the nanometer scale and with a wide array of applications, including electronics and photovoltaics. The NWs used in the present thesis are synthesized by molecular beam epitaxy (MBE) using a technique called vapor-liquid-solid (VLS), where a Au particle acts as the growth catalyst. The NWs have a semiconducting InAs core with a fully surrounding Al shell, which is epitaxially matched to the core [52]. Transmission electron micrographs (TEMs) is shown in Figure 3.1. In Chapters 4-5, results of measurements on qubit devices are compared with the TEMs in this figure. For this comparison, it should be noted that variations in dimensions could result from aging (long time having passed between TEM and device measurement) and wafer position (while the NWs used in devices are from the same gworth batch as those in Figure 3.1, there might be systematic variations in the wire geometry depending on growth wafer position).

Furthermore, as shown by comparing the two NWs in Figure 3.1, variations between individual NWs are also present.

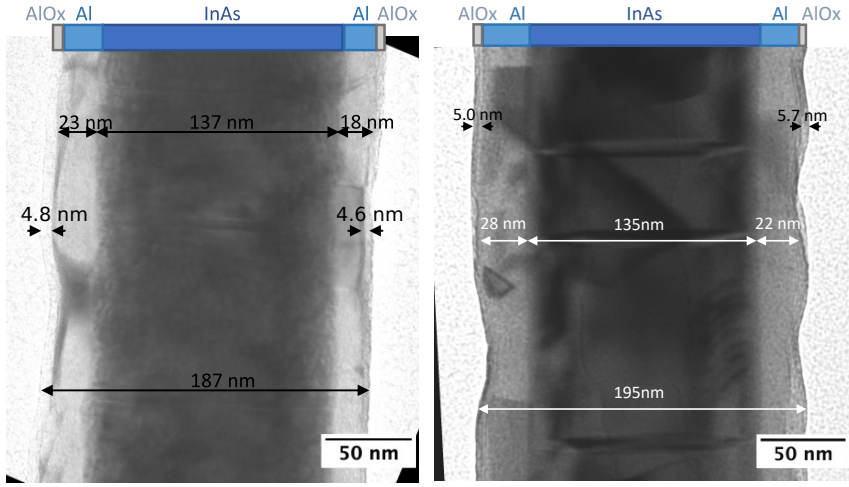

Figure 3.1: Transmission electron micrographs of VLS nanowires. The figure displays micrographs of cross-sections of two nanowires from the same growth batch as those used in Devices 1 and 2 in this thesis (although differences might still exist, see main text). Geometrical distances are indicated in the figure. Martin Espiñeira is acknowledged for the micrographs.

All device fabrication discussed in this thesis is performed by conventional planar methods of integrated-circuit technology on the nanometer up to millimeter scale. Patterns are defined lithographically by electron-beam lithography (EBL) on spin-coated layers of resist. In the context of this thesis, device fabrication generally refers to the following actions:

1. Taking a piece of superconductor-semconductor material, provided by growth specialists, and partially removing the superconductor, in order to form a Josephson junction.

2. Forming one or more gates around the junction, to be used for tuning qubit properties by the semiconductor field effect (see Section 2.4).

3. Forming a circuit-QED transmon control layer around the Josephson junction, for manipulation and readout of the qubit state.

4. Attaching and electrically connecting the finished sample to a holder suitable for low-temperature measurements.

The type of circuit-QED control layer used in this thesis is sketched in Figure. 3.2. A feed line carries microwave signals, produced by room-temperature laboratory equipment, through the device. Meandering $\lambda/4$ coplanar waveguide resonators are inductively coupled to the feed line on one end, resulting in dips in the transmission magnitude at frequencies defined by their lengths (typically $\sim 5\,\mathrm{GHz}$). On their other end, each resonator is capacitively coupled to a qubit island, providing a large shunting capacitance to ground, for increasing E_J/E_C (see Section 2.2). Epitaxially grown superconductor-semiconductor elements, with a JJ formed on them, are connected to the qubit island on one end, and grounded on the other. Gate lines extend from the vicinity of the JJ to the edge of the sample. Many resonator-qubit pairs are coupled to the single feed line (for example, two in the case of Figure 3.2) but are not designed to be coupled to each other. To enable separate readout of each qubit, the lengths of the resonators are different from each other. Everywhere else, the sample surface is covered by a superconducting ground plane. Bond wires connect the feed line, gate lines and the ground plane to a printed circuit boad (PCB), which is in turn connected to the rest of the measurement circuitry (described in Section 3.3).

The fabrication of NW-based gatemon devices is described in the following. Detailed recipe notes are attached in Appendix B. Fabrication start on high-resistivity Si substrates with the deposition of a bottom gate dielectric by low pressure chemical vapor deposition (LPCVD) and the subsequent formation of a NbN circuit-QED control layer (feed line, coplanar waveguides, readout resonators and shunting capacitors providing qubit E_C) by sputtering and reactive ion etching[1]. A second layer of gate dielectric is then deposited on top of the gates using atomic layer deposition (ALD). In the same step, dielectric for crossovers are formed. Crossovers are bridge structures connecting the ground plane across control layer feature, to eliminate electromagnetic mode that might interfere with microwave measurements.

NWs grown by VLS are then mechanically transferred from the growth substrate to the device sample as in indicated in Figure 3.3, using a micromanipu-

[1]The NW device fabrication described here is that of Device 2 (see Table A.1). The process for Device 1 is similar, with the exception that the Device 1 control layer was formed by sputtered NbTiN etched by inductively coupled plasma etching. Device 1 also lacks the LPCVD dielectric below the control layer.

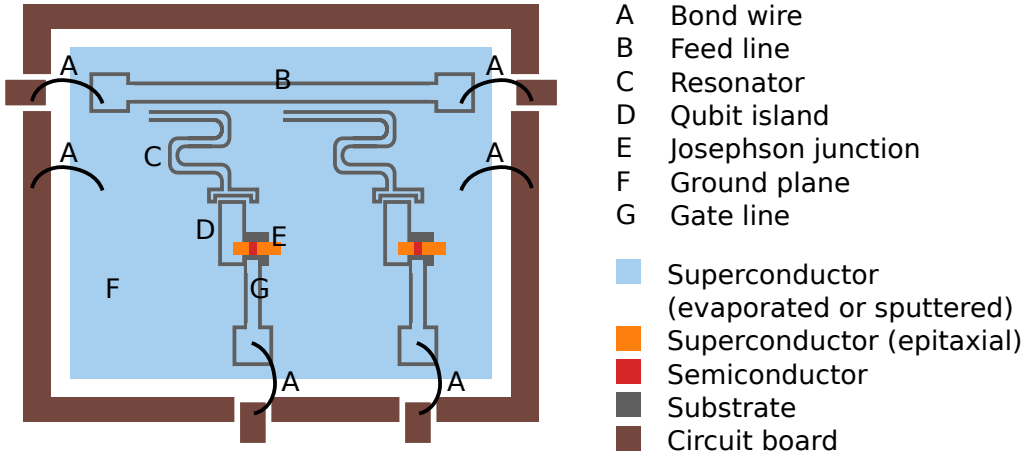

Figure 3.2: Sketch of circuit-QED control layer. Qualitative drawing showing different parts of the device layout (see main text). The drawing is not to scale (in order to capture all components in one drawing, the sizes of some are exaggerated).

lator. The NW is placed such that it will electrically connect to the qubit island (shunting capacitor) on one end and to the ground plane on the other. A Josephson junction is formed in the wire by wet etching[1].

The Al shell of the NW forms a native oxide upon exposure to air, which means that it is not sufficient to place the NW on the NbN control layer to establish electrical contact. To this end, a final fabrication step removes the native oxide by Kaufman milling in the end regions of the wire, upon which a layer of NbTiN is sputtered. This layer of NbTiN also forms the conducting parts of the aforementioned crossover structures. Following fabrication, the devices are wire bonded to a PCB, which can be mounted and loaded into a dilution refrigerator for low-temperature measurements.

[1]Recent developments in growth technology have produced Josephson junctions *in situ* by using shadow growth [53], removing the need for a wet etch step.

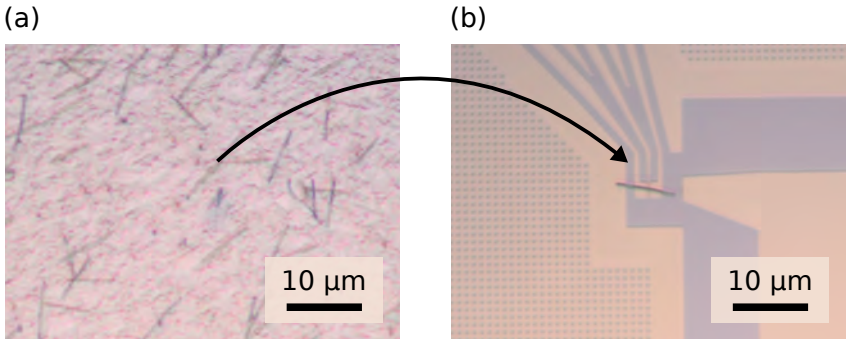

Figure 3.3: Mechanical transfer of nanowires between samples. Optical micrographs indicating the process of using a micromanipulator to transfer a nanowire from (a) the substrate on which it was grown by VLS to (b) a qubit device sample, where it is integrated into a circuit-QED control layer.

3.2 2DEG-based gatemon

By engineering the layers of stacked semiconductors, it is possible to form a high-mobility two-dimensional electron gas (2DEG) [54, Chapter 9]. This structure is of great significant in electronics (used for example in the high-electron-mobility transistor) and for experimental quantum transport where it was used in the first experimental observation of quantized conductance [55]. In Chapter 6, an experiment featuring a gatemon formed in a 2DEG JJ is presented. The 2DEG used for this experiment uses a combination of III-V materials, as depicted in Figure 3.4, and was provided by the Manfra group at Purdue University.

The device fabrication of the 2DEG-based gatemon used in this thesis follows a similar structure as the NW gatemon with a few differences. 2DEG-based gatemons have previously been demonstrated and the fabrication follows this work fairly closely [26]. A fabrication recipe is provided in Appendix C. Device fabrication here starts directly from the growth wafer of the III-V stack hosting the 2DEG. Small pieces are cut from the growth wafer where individual qubit devices are fabricated. First, Ti-Au alignment marks are created by metal evaporation and lift-off. The III-V stack is then removed across nearly the whole sample, except for small rectangular regions referred to as mesas. This is performed by wet etching, first with Transene D for the Al layer and then with specialized etchant (see Appendix C) for the III-V layers.

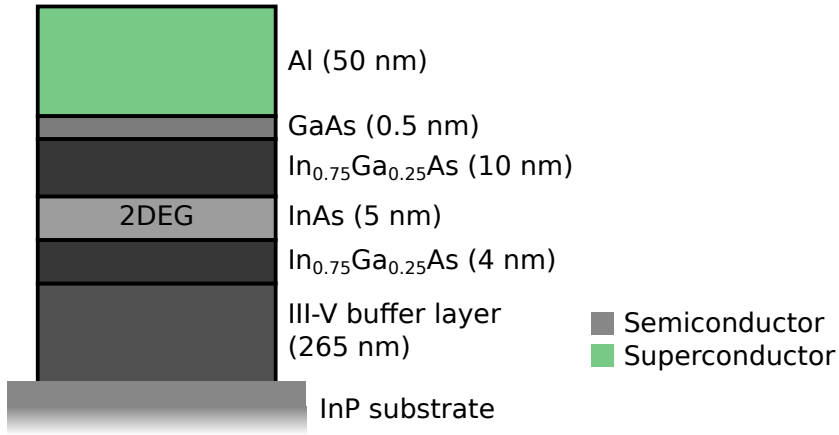

Figure 3.4: Layer structure of the material hosting a 2DEG. Different materials are indicated, with the 2DEG being hosted in the InAs layer. An Al layer at the top of the stack serves to induce superconductivity in the 2DEG by proximity effect. The drawing is not to scale. The Manfra group at Purdue University is acknowledged for providing the 2DEG material.

A circuit-QED control layer is then formed using a combination of lift-off and etch processes. It was found that using lift-off for smaller features and etch-back for larger ones produced a stable fabrication process. The control layer is made of 100 nm evaporated Al. Josephson junctions to be used as gatemons are formed on the mesas by a wet etch in Transene D. A layer of gate dielectric is deposited by ALD. Two rounds of gates are then deposited both consisting of evaporated Ti-Al, the first one producing narrow features on top of the mesa (45 nm Al thickness) and the second one climbing the mesa (390 nm Al thickness) with a Kaufman mill step preceeding it. The reason for this double-layered gates is elaborated on in Chapter 6. Finished devices are wire bonded for loading into a dilution refrigerator setup.

3.3 Dilution refrigerator and measurement setup

Low-temperature measurements are performed in a dilution refrigerator (DR). DRs use a combination of ^{3}He and ^{4}He isotopes to reach temperatures in the millikelvin range [56, Chapter 7]. For the work in this thesis, DR systems from

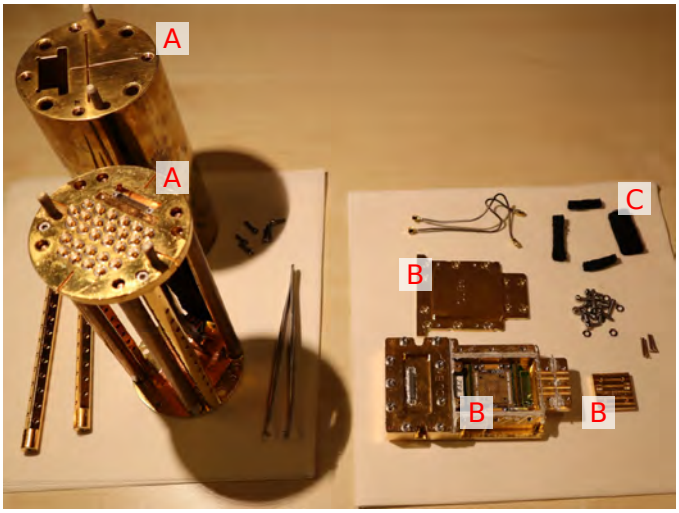

Figure 3.5: Protective sample enclosure for loading into dilution refrigerator. The photograph illustrates how samples were mounted for low-temperature measurements. A cylindrical Cu enclosure (*A*) holds a smaller CuBe box (*B*), where the wire-bonded PCB is mounted by screws and electrically connected by fuzz buttons. The box is stuffed with pieces Eccosorb (*C*) for protection against electromagnetic radiation, and is sealed by In wire.

both Oxford Instruments and Bluefors are used, usually operated at a temperature around $\sim 30\,\mathrm{mK}$. PCBs with finished qubit samples wire bonded to them are mounted in a CuBe enclosure, shown in Figure 3.5. The space surrounding the samples are filled with Eccosorb filter material to provide protection against stray electromagnetic radiation. The sample PCB is connected via fuzz buttons to a larger PCB with electric filtering, which then interfaces with the DR cold fingers allowing for room temperature instruments to apply and measure signals via wiring through the DR. The CuBe box is places in a cylindrical Cu holder ("puck"), which is bottom-loaded into the DR.

All three experiments described in this thesis (Chapters 4-6) are centered around measurements of microwave transmission. A schematic of the setup used

to facilitate these measurements is shown in Figure 3.6[1]. Room temperature instruments generate signals that are filtered and sent down through the sample via DR wiring. Having passed through the sample feed line, the high-frequency signal is amplified and recorded by other room temperature instrumentation. Single-tone transmission experiments are performed by S21 measurements on a vector network analyzer (VNA). Two-tone measurements (spectroscopy and time domain sequences as depicted in Figure 2.3) are performed by heterodyne demodulation. In such a measurement, an arbitrary waveform generator (AWG) is used to IQ modulate an radio frequency (RF) vector source before it is sent to the sample feed line. Having passed through the sample and interacted with the readout resonator, the signal is mixed with the unmodulated frequency (commonly referred to as LO for local oscillator) and recorded by a digitizer. It is then downconverted further in software producing a complex V_H, which is recorded and saved. This scheme is a conventional way of performing high-frequency measurements and is described in more detail e.g. in Reference [7].

Drive pulses intended to excite the qubit are combined with readout pulses and delivered to the qubit via the same DR wiring and sample feed line as readout pulses. Pulse shapes are programatically defined on a computer, uploaded to the AWG and generated on a separate RF vector source, which is IQ modulated by the AWG output. Gate voltages are generated on a digital-to-analog converter (DAC). Instrument control and data acquisition are achieved by the QCoDeS and Labber softwares. Some data presented in this thesis, in particular two-dimensional spectroscopy data, is shown with the background having been subtracted. This is usually achieved by subtracting each trace by the mean value of that trace in a two-dimensional data set and is not intended to alter the interpreted features in the data, but only to enhance signal visibility.

In Chapter 6, measurements of dc transports are presented in addition to the high-frequency techniques described above. For this, additional instrumentation is attached to the sample as shown in Figure 3.7. It is similar to the setup described in Reference [32, Supplemental material]. The main instrument is the lock-in amplifier, which can measure small voltages even in the presence of noise by the incorporation of a known reference signal. The logic of the transport

[1]The diagram in this figure illustrates the setup used for the experiments in Chapters 4-5. A similar setup was used in Chapter 6 except without a TWPA, with the addition of instrumentation for dc transport measurements (see Figure 3.7) and minor differences e.g. in filtering and instrument models.

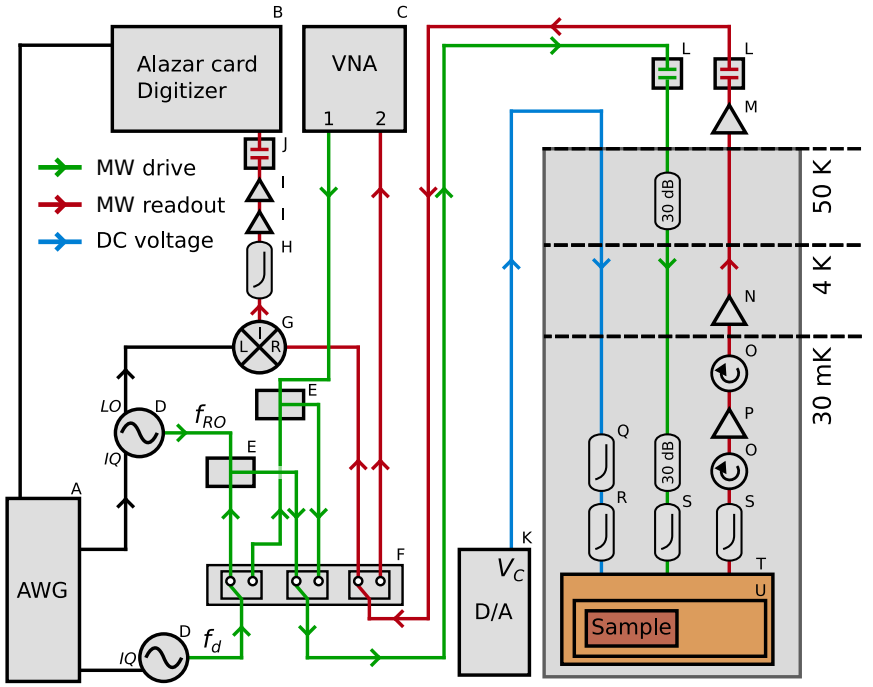

A Tektronix AWG5208
B AlazarTech ATS9360
C Rhode & Schwarz VNA ZNB20
D Rhode & Schwarz SGS100A
E Picosecond PSPL5333 Power divider
F Mini-Circuits 4SPDT RF Switch
G Marki M8-0420MS Mixer
H Picosecond LP 5915
I SR445A 350 MHz Preamplifier
J Mini-Circuits BLK-89-S+ DC block
K Custom DAC
L Midwest DCB-3511 DC block
M Miteq AFS3-04000800-10-ULN amplifier
N LNF-LNC4_8C 4-8 GHz cryogenic low noise amplifier
O Quinstar QCI-075900XM00
P Traveling-wave parametric amplifier
Q QDevil QFilter
R Mini-Circuits LFCN-80 LPF
S Marki FLP0960
T Cu Puck
U CuBe Sample box

Figure 3.6: Diagram of high-frequency measurement setup in a dilution refrigerator. A radio-frequency switch (indicated by *F*) enables the setup to be used for both VNA S21 transmission measurements, as well as time domain measurements using a digitizer (indicated by *B*).

measurement is as follows (quantities indicated in Figure 3.7). Measurements of differential resistance across the device under test (DUT) are achieved by applying a voltage bias V_{DAC} while measuring I_B through the DUT. A voltage divider combines the dc bias with the lock-in reference signal, which is then applied as a bias to the DUT through a current-to-voltage converter. The voltage divider is produced specifically for usage with the current-to-voltage converter and outputs combined ac and dc with ratios $\beta_{\mathrm{ac}} = 10^{-5}$ and $\beta_{\mathrm{dc}} = 10^{-3}$, respectively. The current I_B is converted to a voltage in the current-to-voltage converter with a conversion factor of $\alpha_b = 10^5 \mathrm{V/A}$, the ac component is measured by the lock-in amplifier and the dc component by a digital multimeter. The differential resistance of the DUT is given by $dR = dV_J/dI_B$ where

$$dV_J = \beta_{\mathrm{ac}} V_{\mathrm{amp}} - dI_B R_{\mathrm{line}} \tag{3.1}$$

and $dI_B = V_X/\alpha_b$ where V_{amp} us the chosen lock-in ampliude, R_{line} is the line resistance and V_X is the X component of the measured lock-in voltage. The dc component of I_B is computed as $V_{\mathrm{DMM}}/\alpha_b$. Taken together, this allows the computed dR to be plotted parametrically as a function of current bias I_B as V_{DAC} is swept.

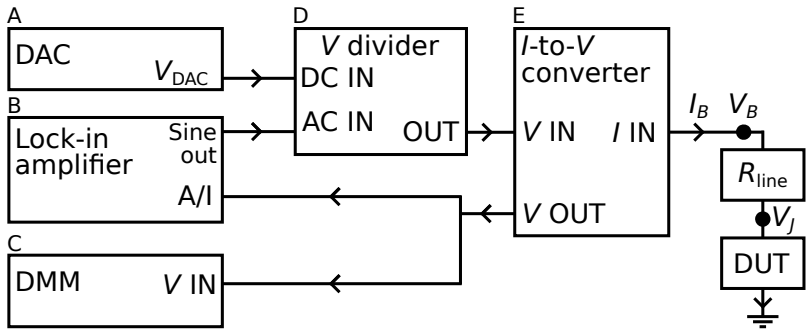

A	Custom DAC	D	Custom voltage divider
B	Stanford SR830		(1:1E3 DC, 1:1E5 AC)
C	Agilent 34400A	E	Basel SP983c

Figure 3.7: Diagram of setup for dc transport measurements. One side of a two-terminal DUT is connected to a measurement circuit and the other side is grounded. An I-to-V converter delivers a voltage bias to the DUT while converting I_B to a voltage, which is then measured by a lock-in amplifier and a DMM.

Chapter 4

Destructive Little-Parks effect in a full-shell nanowire-based transmon

In Section 2.4, a number of experiments on gatemon qubits were reviewed. Some of those experiments used NWs with a superconducting shell covering half of the facets of the wire and some experiments studied NWs with a fully-covering superconducting shell. For many purposes, in particular at zero magnetic field, these two systems show similar behavior. At finite magnetic field, however, the full-shell NWs exhibit destructive Little-Parks effect, resulting in a non-monotonic dependence of the superconducting gap on parallel magnetic field.

In this chapter, this non-monotonic dependence on magnetic field is examined in the context of a gatemon qubit and circuit-QED. The chapter is based on the following publication

- "Destructive Little-Parks effect in a full-shell nanowire-based transmon" (2020) by D. Sabonis*, **O. Erlandsson***, A. Kringhøj*, B. van Heck, T. W. Larsen, I. Petkovic, P. Krogstrup, K. D. Petersson, C. M. Marcus. *Physical Review Letters*, 125(15):156804.
  * These authors contributed equally to this work.

The text has been re-written for the context of the thesis and some additional discussion is provided.

4.1 Half-shell and full-shell nanowires

Nanowire-based gatemons have employed epitaxial Al shells covering either half of the hexagonal NW surface (two or three out of six facets) [29, 31, 33, 57] or shells that fully surround the surface (all six facets) [22, 24, 30, 32]. Implementations without a shell have also been demonstrated [23]. In half-shell NWs, the superconducting gap often follows a square-root dependence on parallel magnetic field, of the form,

$$\Delta(B) \propto \sqrt{1-(B/B_c)^2} \tag{4.1}$$

where B_c is the critical magnetic field, attributed to BCS theory [25, 57, 58]. In the transmon regime $E_J/E_C \gg 1$, Equation 2.3 then yields a qubit frequency

$$f_{01}(B) \propto \sqrt[4]{1-(B/B_c)^2}\,. \tag{4.2}$$

For NWs exhibiting this behavior, the qubit frequency monotonically decreases as B is increased, eventually collapsing to zero at $B = B_c$. However, this field-dependence is not universal in half-shell NWs, and non-monotonic $\Delta(B)$ has also been reported [33, 57, 59].

In full-shell NWs a non-monotonic $\Delta(B)$ appears due to the Little-Parks effect [45, 60]. This effect arises due to the quantization of magnetic flux through a superconducting cylinder and causes $\Delta(B)$ to exhibit periodic oscillations. Prior to NW experiments, similar observations of the effect have been made in other cylindrical superconductors [61]. A qualitative illustration of the differences in the magnetic-field-dependence of half-shell and full-shell NWs is shown in Figure 4.1.

The mathematical description of $\Delta(B)$ as governed by the Little-Parks effect can be given using the pair-breaking parameter α of the Abrikosov–Gor'kov theory [62, Section 10.2], from which other parameters such as the critical temperature T_c and the superconducting gap Δ are obtained. For the case of a superconducting cylinder (of which a full-shell nanowire is a realization), $\alpha(B)$ is given by minimizing the function [63–65],

$$\alpha(B) = \frac{4\xi^2 k_B T_{C0}}{\pi R^2}\left[\left(n-\frac{\Phi}{\Phi_0}\right)^2 + \frac{t^2}{4R^2}\left(\frac{\Phi^2}{\Phi_0^2}+\frac{n^2}{3}\right)\right] \tag{4.3}$$

in the integer winding number n at each B, where ξ is the superconducting coherence length at zero field, T_{C0} is the critical temperature at zero field, Φ is the

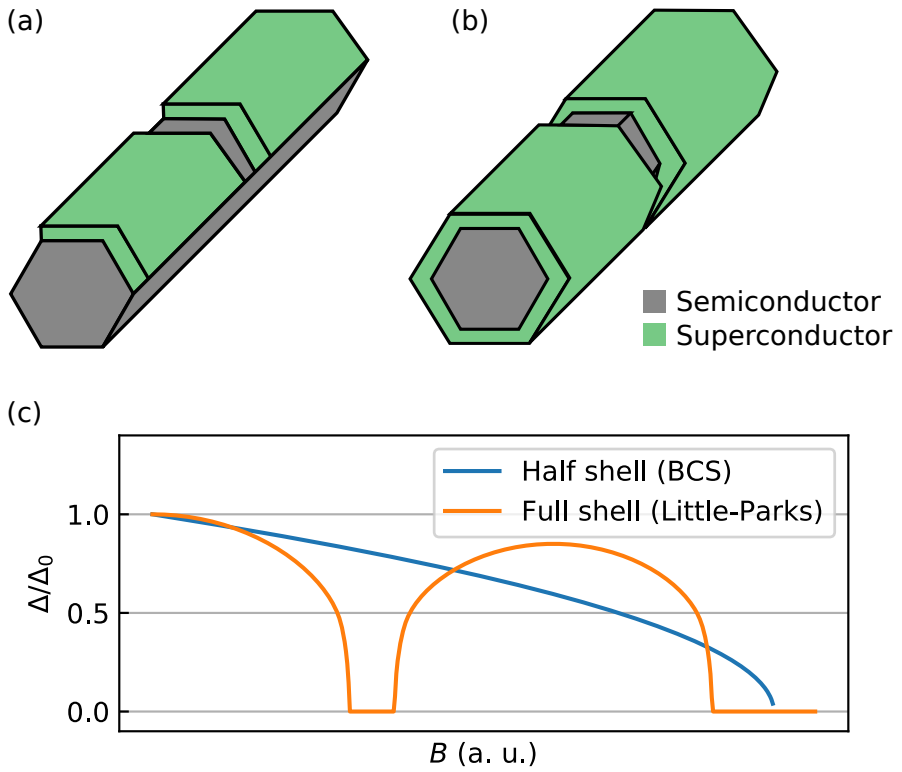

Figure 4.1: Half-shell and full-shell nanowires and the magnetic-field-dependence of their superconducting gaps. (a) Half-shell NW. Depicted here with two facets covered by the superconducting shell, although three-facet NWs are also referred to as half-shell. (b) Full-shell NW with a superconductor on all six facets. (c) Qualitative illustration of $\Delta/\Delta_0(B)$ for both types of nanowire.

applied magnetic flux, R is the radius of the superconducing shell, and t is the shell thickness. Once α is calculated, Δ can be computed from [66]

$$\log\frac{\Delta_0}{\Delta} = \begin{cases} \frac{\pi\alpha}{4\Delta}, & \text{if } \alpha < \Delta, \\ \log\left(\frac{\alpha+\sqrt{\alpha^2-\Delta^2}}{\Delta}\right) - \frac{\sqrt{\alpha^2-\Delta^2}}{2\alpha} + \frac{\alpha}{2\Delta}\arcsin\frac{\Delta}{\alpha}, & \text{if } \Delta > \alpha. \end{cases} \tag{4.4}$$

The gatemon frequency can then be modeled as $f_{01} \propto \sqrt{\Delta(B)}$. It should be noted that what is referred to as the superconducting gap Δ in the above is the pairing

strength of Cooper pairs[1] which is here taken to enter the transmon Hamiltonian in Equation 2.1.

Many parameters enter into Equations 4.3 and 4.4 and thereby influence the form of the magnetic-field-dependence of the superconducting gap in full-shell NWs. To get a better understanding for some of these, $\Delta(B)$ is computed for some variations of parameters in Figure 4.2. From this figure, a number of trends are apparent. Figure 4.2a shows the effect of varying the thickness of the superconducting shell. A thicker superconducting shell results in smaller lobes, both in terms of the span in magnetic field B and the value of Δ at a given B. Variations in the NW radius R, as shown in Figure 4.2b (where the shell thickness t is kept fixed) also affect the size of the lobes, although in a different way. Larger R increases the maximum Δ/Δ_0 for the first lobe. However, it also reduces the separation between the zeroth and first lobe maxima with only small variations in the B span of each lobe. Finally, the effect of increased superconducting coherence length ξ is to supress Δ at all B, as shown in Figure 4.2c.

Due to the hybrid superconductor-semiconductor composition of the gatemon, an experimental area of interest is the search for Majorana zero modes (MZMs) in the NWs [39] (see Section 2.5). Results from dc transport experiments possibly indicate that MZMs can appear in the first Little-Parks lobe, at around 0.1 mT [45], whereas half-shell systems might require $\sim 1\,\mathrm{T}$ to enter the topological regime [39]. In the context of attempts of circuit-QED detection having encountered issues with qubit operation in large magnetic fields [16], the full-shell NWs forms an interesting alternative materials system. Beyond the search for MZMs, the Little-Parks effect offers a platform for examining the influence of magnetic field on phenomena such as quasiparticle poisoning which is explored in Chapter 5.

In comparison to dc transport, high-frequency circuit-QED experiments provide new ways to probe MZMs beyond e.g. zero-bias peaks. The amount of overlap between the wave functions on either side of the JJ is referred to as the energy scale E_M [49, 67–69] and is an important parameter for using MZMs in a qubit. Theory predicts signatures of E_M in the charge dispersion of the qubit [49, 50]. Whereas the parity branches of the transmon Hamiltonian in Equation 2.1 normally result from incoherent tunneling of QPs across the junction [70], overlapping MZMs enable coherent transport of $1e$ charge across the junction, resulting

[1] The pairing strength of Cooper pairs is also called the gap parameter in Section 10.2 of Reference [62].

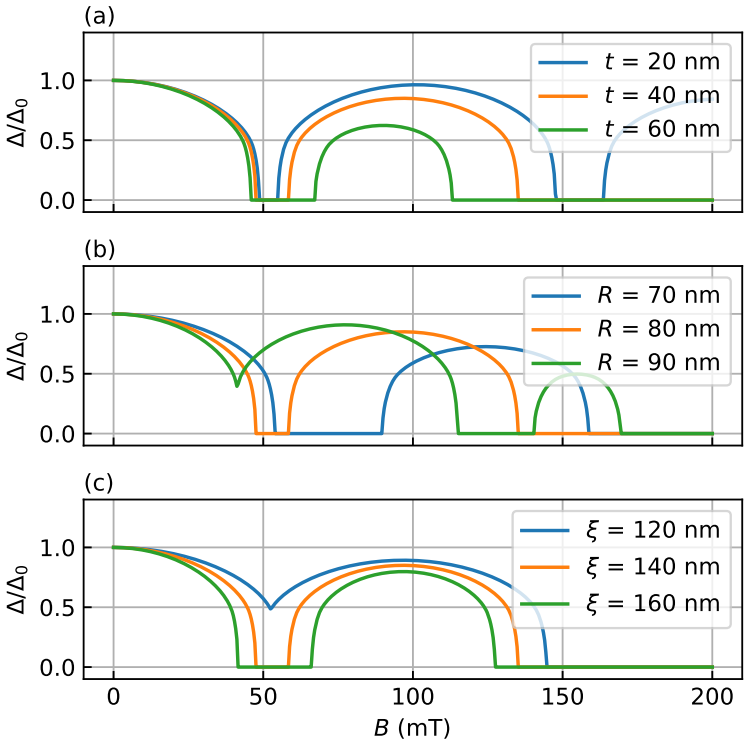

Figure 4.2: Parameters influencing the lobe structure of $\Delta(B)$ for full-shell NWs. Values of parameters are picked to be similar to experiments. The non-varied parameters are shell thickness $t = 40\,\text{nm}$, wire radius $R = 80\,\text{nm}$ and superconducting coherence length $\xi = 140\,\text{nm}$. In subfigures (a) through (c) t, R and ξ are varied, respectively.

in the simultaneous presence of both parity branches. Figure 4.3 shows a simulation of the signature of finite E_M in the circuit-QED experiment.

A gatemon with finite E_M does not constitute a topologically protected qubit. However, the detection of E_M by a circuit-QED measurement in a gatemon device would demonstrate the implementation of the topological phase in a type of sample relevant for quantum information processing. In summary, attempting to detect MZMs by circuit-QED in a full-shell NW appears worthwhile.

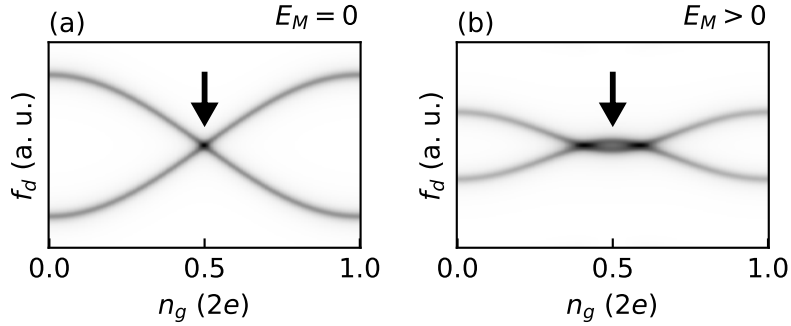

Figure 4.3: Simulation of the signature associated with a finite Majorana coupling E_M as probed by a circuit-QED experiment. (a) Trivial regime showing two qubit transition peaks, resulting from QPP. (b) Topological regime. The two peaks appearing here result from coherent $1e$-transport across the junction. in both panels, an arrow indicates a point in the charge dispersion where the trivial and topological regimes are clearly distinct.

4.2 Device considerations

In order to study the the Little-Parks effect in a gatemon qubit, NW devices are fabricated as described in Section 3.1 and detailed in Appendix B. The resulting devices are gatemons where the JJs are formed in InAs NWs with a superconducting Al shell fully surrounding the semiconductor. In this chapter, data is presented from two devices fabricated on separate physical samples, which show similar features. Micrographs of the devices are shown in Figure 4.4.

The devices are fabricated on $5\,\text{mm} \times 5\,\text{mm}$ chips cut from a high-resistivity Si wafer. A sputtered NbN plane covers most of the chip surface. Microwave lines are connected to bond pads on either end of a feed line, enabling the transmission of high-frequency signals through the device. A number of coplanar waveguides used as readout resonators are formed adjacent to the feed line.

Gate voltages are applied to the devices via fridge dc lines which, continue onto the chips via bond wires. These lines lead up to the NW JJs, as shown in Figure 4.4b, where the voltages tune the Josephson energy E_J of the qubit via channel transmissions (Equation 2.4). Patches of HfO_2 dielectric prevent gate voltages from drawing a current through the NWs. The NWs are connected to

the ground plane on one end of the JJ and to an island with a large shunting capacitance on the other side. The island geometry is designed to yield a qubit charging energy $E_c = 512\,\text{MHz}$, based on electrostatic simulations. The feed and gate lines on chip are straddled by NbTiN cross-overs to suppress standing waves that adversely affect the microwave environment.

To facilitate operation of the devices in the first Little-Parks lobe, the samples are designed to be magnetic-field-compatible. This means that the ground plane material is NbN, which is high-B_c, instead of e.g. Al. Furthermore, the ground plane is patterned with flux-trapping holes, in order to avoid moving vortices at finite field [71].

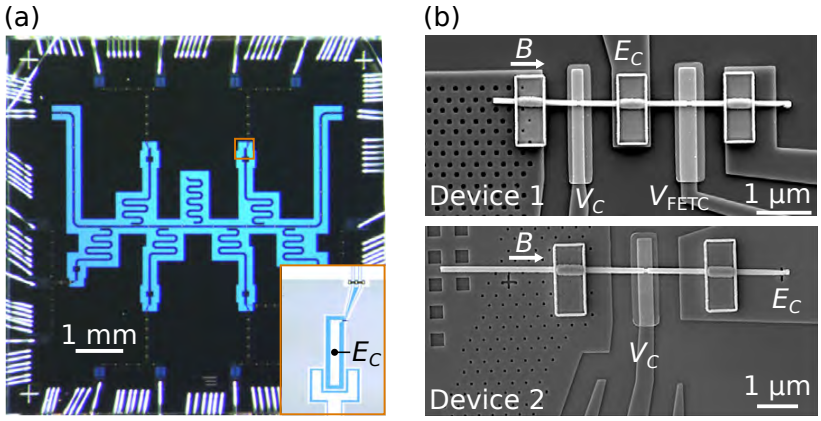

Figure 4.4: Micrographs of nanowire devices. (a) Optical micrograph showing an overview of the chip. The inset displays the qubit island, defining the charging energy E_C of the transmon. (b) Scanning electron micrographs of the NWs with JJs formed in them. The right JJ of Device 1 and the associated V_{FETC} gate is intended for *in situ* transport measurements, but is not used in the present thesis.

Like other gatemons, the devices offer *in situ* tunability of E_J. Data demonstrating this for Device 2 is shown in Figure 4.5, measured by two tone-spectroscopy. At each gate voltage V_C, an S21 transmission measurement is first performed using a VNA (Figure 4.5a). Based on the resulting transmission data, a readout frequency f_{RO} is chosen. The transmission at f_{RO} is monitored while a drive tone with frequency f_d is applied. If f_d matches f_{01}, the drive tone will excite the qubit resulting in a qubit-state-dependent shift of the readout resonator. For this reason, the heterodyne transmission measurement of V_H as a function of

f_d will show a peak around f_{01}. Multi-photon processes give rise to additional peaks, e.g. around $f_{02}/2$. Resulting data from the two-tone spectroscopy measurement are shown in Figure 4.5b. Spectroscopy measurements are performed using a high-frequency demodulation circuit based around a digitizer. More details on the measurement setup are presented in Section 3.3. The devices used here do not have a dedicated microwave drive line and drive tones are instead applied via the feed line.

4.3 Zeroth and first lobe

The Little-Parks effect is detected in circuit-QED by a field-dependent two-tone spectroscopy measurement. Fixing the gate $V_C = -2.5\,\mathrm{V}$ yields a qubit frequency $f_{01} = 4.3\,\mathrm{GHz}$ at zero magnetic field. The magnetic field B parallel to the NW is then increased to $\sim 130\,\mathrm{mT}$ with the two-tone measurement repeated at intermediate set points. The range of f_d sweeps are adjusted to capture the peak corresponding to f_{01} and its vicinity. The results are shown in Figure 4.6a. Several features in these data are interesting to note. The qubit frequency f_{01} shows a non-monotonic oscillatory dependence on B consistent with the Little-Parks effect. At certain values of B, around e.g. 80 mT, the f_{01} feature appears to split. This is interpreted as instability in the offset-charge n_g, in the sense that traces with a single peak are instances where n_g is close to the degeneracy point of the charge dispersion and vice versa. Finally, the spectroscopy peak alters between visible and invisible around 40 mT, 55 mT and 130 mT. A possible interpretation of this is decoherence caused by quasiparticle poisoning, which is revisited in the next chapter[1].

Figure 4.6b shows a fit of the data in Figure 4.6a to Equations 4.3 and 4.4 with the assumption that $f_{01} \propto \sqrt{\Delta}$. The resulting fit parameters are $R = 81\,\mathrm{nm}$, $t = 36\,\mathrm{nm}$ and $\xi = 139\,\mathrm{nm}$ with the proportionality constant $f_{01}(B=0) = 4.34\,\mathrm{GHz}$. The geometrical parameters are comparable to those observed in NW micrographs (see Fig. 3.1 and note the surrounding discussion).

Differences with respect to qubit properties in the zeroth and first lobe are examined in the measurement results displayed in Figure 4.7. As discussed in Section 2.3, T_1 is a measure of the time scale in which the qubit remains in one of the logical states. In order to probe this, Rabi and relaxation time domain

[1] In particular, see Figure 5.11 and the surrounding discussion.

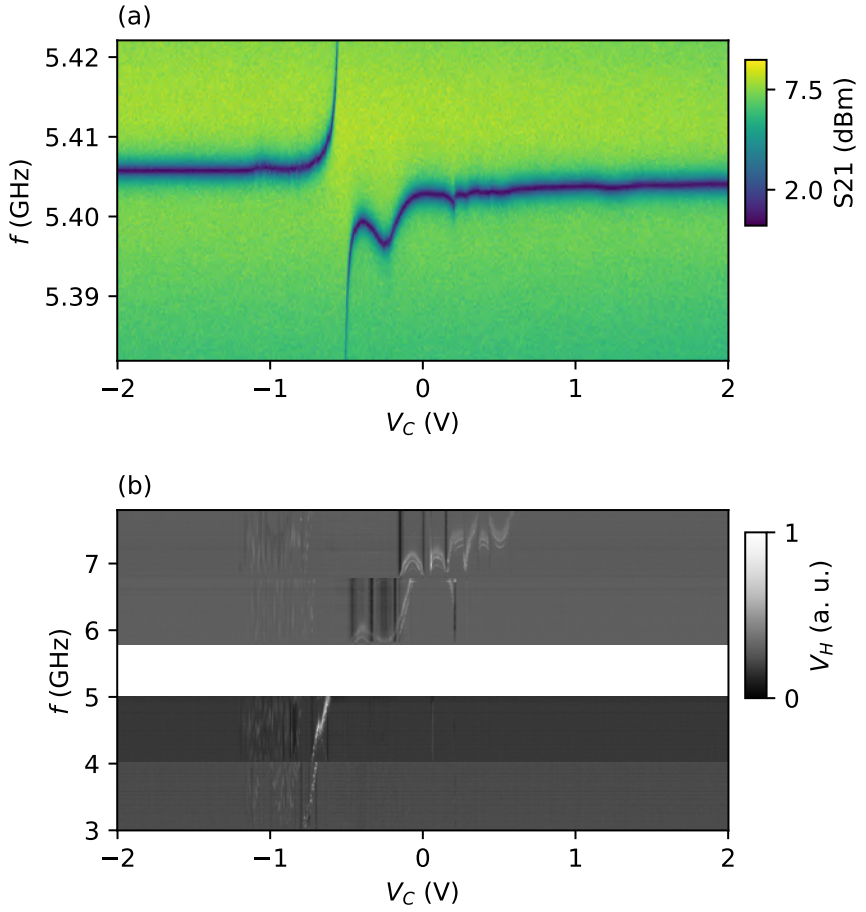

Figure 4.5: Tunability of gatemon qubit frequency. (a) Transmission measurement taken by VNA. (b) Two-tone spectroscopy measurement. The qubit frequency f_{01} can be seen to increase non-monotonically from 3 GHz to 7.5 GHz in the interval $-1\,\mathrm{V} < V_C < 1\,\mathrm{V}$. Subfigure (b) consists of several data sets displayed together, which causes the apparent discontinuities in the background, as well as in the evolution of f_{01} due to hysteresis in the gate-dependence of JJ channel transmissions. Data is not taken for $f_d \sim f_{\mathrm{RO}}$. Data from Device 2.

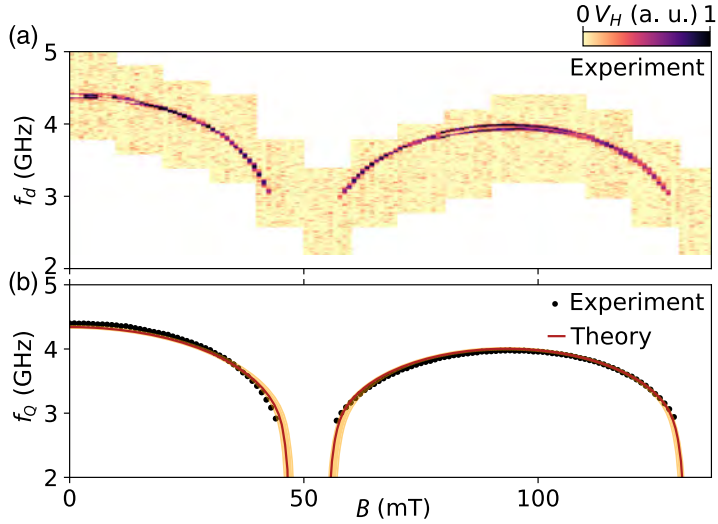

Figure 4.6: Destructive Little-Parks effect detected by circuit-QED. (a) Two-tone spectroscopy data. The qubit frequency f_{01} shows a non-monotonic dependence on the applied magnetic field B parallel to the NW, interpreted as the Little-Parks effect. (b) Values of f_{01} as extracted from the spectroscopy data in (a), along with a fit to the equations describing the Little-Parks effect. The orange band corresponds to the 3rd-97th percentile of the fit. Parameters from the fit are given in the main text. Data from Device 1.

experiments are performed in either lobes. This sequence of measurements was performed at $B = 0\,\mathrm{T}$ with $V_C = -1.4\,\mathrm{V}$ yielding $f_{01} = 4.5\,\mathrm{GHz}$. The results are shown in Figure 4.7a-b. In this regime, the fit to experimental data yields a Rabi decay time $T^R = 0.18\,\mu\mathrm{s}$ and relaxation time $T_1 = 2.5\,\mu\mathrm{s}$. Relaxation times around 1–10 µs is the state of the art of NW gatemons [22,23,25]. In the first lobe of the destructive Little-Parks effect ($B = 100\,\mathrm{mT}$), the same set of measurements at $V_C = -2.73\,\mathrm{V}$ and $f_{01} = 3.8\,\mathrm{GHz}$ yielded $T^R = 0.34\,\mu\mathrm{s}$ and $T_1 = 0.5\,\mu\mathrm{s}$ (Figure 4.7d-e). The observation of Rabi oscillations at $B = 100\,\mathrm{mT}$ confirms that the qubit is still coherent in the first lobe and time domain studies are possible in a regime where transport experiments possibly show the presence of MZMs. The reduction in T_1 indicates the presence of an energy relaxation mechanism that appears in the first lobe and not in the zeroth, or the increase in magnitude of a mechanism present in both lobes. An interpretation corresponding to the

former case would be the appearance of subgap states in the first lobe causing dissipation of energy [72].

In Figure 4.7e,f the charge dispersion of the qubit transition is probed in the zeroth and first lobe by gate-dependent two-tone spectroscopy measurements. Small changes in the gate voltage V_C allows for control of the offset-charge n_g without a large effect on E_J, keeping f_{01} nearly constant. Apparent to the eye, the structure of the charge dispersion is qualitatively similar across both lobes. The oscillations of f_{01} follow the expectation from the transmon Hamiltonian (Figure 2.2).

At each value of V_C, except at degeneracy points in n_g, two peaks can be seen in the spectroscopy trace. In the zeroth lobe the interpretation of this doubling is quasiparticle poisoning [70] and there is no expectation of any topologically non-trivial phenomena. If the system is interpreted to remain in the trivial regime in the first lobe, the origin of peak doubling is the same as for $B = 0\,\mathrm{T}$. On the other hand, if the system is interpreted to be in the topological regime, the origin of peak doubling is instead a coherent transport of $1e$ charge across the junction and the peaks correspond to different transitions within the spectrum of a Hamiltonian with a term proportional to E_M [49].

While the peak doubling itself does not indicate whether the system is in the trivial or topological regime, the structure of the charge dispersion has the potential to do so. As shown in Figure 4.3, the topological regime is expected to be concomitant with a gap replacing the crossing of parity branches at the degeneracy points in n_g. In the first lobe data shown in Figure 4.7f, no such gap can be seen. The charge dispersion data at $B = 104\,\mathrm{mT}$ is consistent with trivial superconductivity. Quantitative analysis of the data produces an experimental upper bound on the Majorana coupling $E_M/h < 10\,\mathrm{MHz}$[1].

Measurements of the evolution of T_1 as the magnetic field is increased is shown in Figure 4.8. As indicated in the figure, data are taken at different gate voltages. The trend of T_1 being suppressed in the first lobe persists across all gate voltages probed and in different values of B within either lobe.

4.4 Conclusion

In this chapter, a full-shell superconductor-semiconductor NW gatemon was studied at zero and finite magnetic field. At zero field, the qubit is coherent with

[1] See the supplemental material of Reference [73] for details of this calculation.

a T_1 similar to that reported in previous studies of similar NW devices. As the parallel magnetic field is increased, the NW enters a lobe of reentrant superconductivity. A fit to equations from theory confirms the applicability of Little-Parks theory to the data.

The charge dispersion signature of the topological regime was not observed in the first lobe. Although this does not rule out the presence of MZMs the measurement results provide an upper bound on the Majorana coupling $E_M < 10\,\mathrm{MHz}$. Vanishing or small (relative to experimental conditions) E_M could be due either to the inapplicability of the theory of topological superconductivity to the particular material at hand or because of disorder in the material reducing the overlap of MZM wavefunctions.

Although no signatures of MZMs were detected, the experiment demonstrates the integration of the Little-Parks effect, a cornerstone phenomenon of superconductivity, in a modern device oriented toward quantum information. The detection of coherent oscillations and stable charge dispersion in the first lobe confirms the suitability of the circuit-QED approach for probing the presence of MZMs and could be revisited should further input become available pertaining to topological superconductivity, e.g. from theory or materials science.

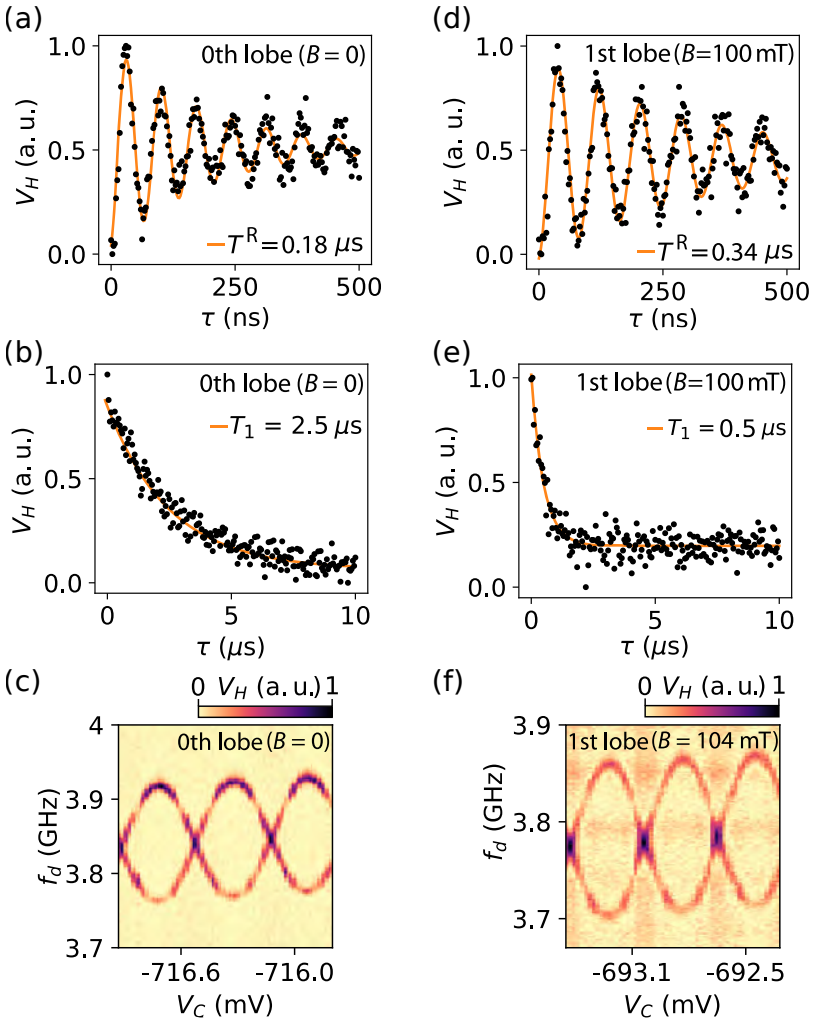

Figure 4.7: Charge dispersion and time domain experiments in zeroth and first lobe. In (a)-(c) $B = 0\,\mathrm{T}$. (a) Rabi oscillations. (b) Relaxation measurement yielding with an exponential fit yielding T_1 as indicated. (c) Charge dispersion of both parity branches of the gatemon energy transitions. Subfigures (d)-(f) show results from the same measurements taken in the first lobe ($B \sim 100\,\mathrm{mT}$). A comparison of (c) and (f) reveal no apparent signature of finite E_M in the first lobe. Data in panels (a)-(b) and (d)-(e) from Device 1 and in (c), (f) from Device 2.

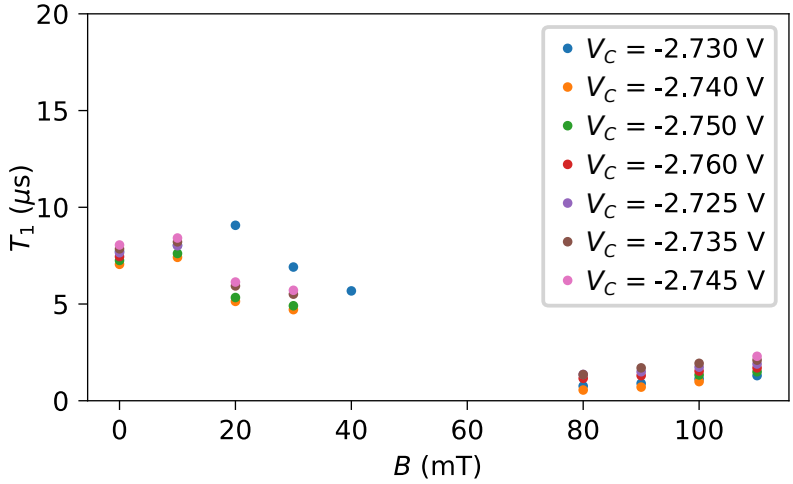

Figure 4.8: Magnetic-field-dependence of relaxation time T_1 across the zeroth and first lobe of the Little-Parks effect. For T_1 to be measured, the superconducting gap Δ needs to be finite and within the experimentally accessible range. Furthermore the spectroscopy peak corresponding to f_{01} must remain visible (for example, not too broadened by decoherence). The lack of data points for $40\,\mathrm{mT} < B < 80\,\mathrm{mT}$ result from these limitations. Data from Device 1.

Chapter 5

Parity switching in a full–shell superconductor–semiconductor nanowire qubit

In this chapter, another aspect of loss in the gatemon qubit is investigated, namely that related to uncontrolled charge-parity switching. This phenomenon is also known as quasiparticle poisoning (QPP). Depending on the rate of QPP in comparison to other loss mechanisms, the presence of QPP could limit the qubit lifetime and coherence.

The content of this chapter is based on the pre-print

- "Parity switching in a full-shell superconductor-semiconductor nanowire qubit" (in review) by **O. Erlandsson***, D. Sabonis*, A. Kringhøj, T. W. Larsen, P. Krogstrup, K. D. Petersson, C. M. Marcus.
  * These authors contributed equally to this work.

All data in this chapter is from Device 2, introduced in Chapter 4.

5.1 Quasiparticle poisoning

The operation of any qubit relies on preventing energy loss to the environment as well as keeping the parameters of the Hamiltonian stable. At present, the transmon qubit is one of the most established types of superconducting qubit. The

energy levels of its Hamiltonian are plotted in Figure 5.1. In contrast to Figure 2.2 each energy level has here two parity branches, denoted by subscripts e and o for even and odd. This doubling occurs because unpaired quasiparticles (QP) can tunnel across the JJ, which causes a shift in n_g by $1/2$ (half of a Cooper pair). Typically these events happen at a rate faster than the duration of measurement, which means that the experimenter will see both even and odd branches of the Hamiltonian [70].[1]

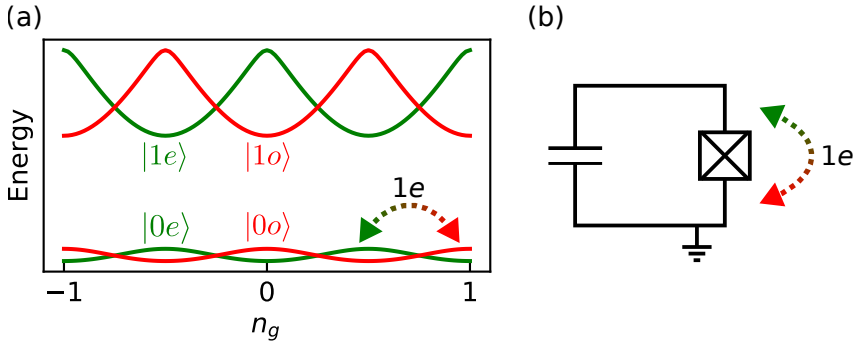

Figure 5.1: Quasiparticle poisoning and transmon energy levels. (a) Transmon energy level spectrum. In contrast to Figure 2.2, ground and excited states each have two levels resulting from QPP. (b) Schematic illustration of QPP. An unpaired QP tunneling across the junction and thereby shifting n_g by $1e$.

Apart from giving rise to the doubling of the transmon energy levels, QPP can adversely affect qubit lifetime and coherence time. As described above, the shift $n_g \to n_g + 1/2$ in the Hamiltonian alters the transition energy E_{01} and thus causes dephasing of the quantum state. However, in the transmon limit $E_J/E_C \to \infty$, the two parity branches are degenerate due to the suppression of charge dispersion. While this suppresses the aforementioned decoherence mechanism, QPP still imposes limits on qubit lifetime. This is due to the fact that QPs can carry energy either out of, or into, the qubit as they tunnel across the JJ, leading to relaxation and residual excitation, respectively. The prevalence of such QPP-induced relaxation and excitations depends on the energy distribution of the QPs [74].

[1] Note that these branches are not simultaneous solutions of the same Hamiltonian, but instead solutions of $\hat{H}$ plotted together with $\hat{H}(n_g \to n_g + 1/2)$.

Table 5.1: Transmon poisoning times T_P reported from other experiments. No discrimination based on logical state source and destination is made for the quantities listed in this table.

Year	Work	Measured T_P (order of magnitude)
2013	Ristè *et al.* [75]	50 µs – 1 ms
2018	Serniak *et al.* [74]	10 µs – 100 µs
2019	Serniak *et al.* [76]	1 ms – 10 ms
2021	Uilhoorn *et al.* [84]	50 µs – 500 µs
2022	Gordon *et al.* [77]	10 µs – 100 ms
2022	Kurter *et al.* [78]	10 µs – 1 s
2022	Pan *et al.* [79]	10 ms – 1 s

The extent to which QPP limits the performance of a given qubit depends on the time scale T_P, on which the poisoning events occurs. QPP is conventionally modeled as a random telegraph signal and the quantitative assignment of T_P can be done by fitting the Fourier transform of measured time traces to a Lorentzian function. QPP in transmons has been studied in many experiments and a wide range of values of T_P have been reported. Results from some of the key experiments are listed in Table 5.1.

Initial measurements of QPP in transmons were performed on Al devices using a Ramsey-type pulse sequence and yielded $T_P \sim 1\,\text{ms}$ [75]. The same technique was later used to probe the energy distribution of QPs and individually measure transitions across all four parity-logical states [74]. An alternative measurement scheme that relied on direct monitoring of transmission rather than pulse schemes was introduced in Reference [76], which also demonstrated an increased T_P attributed to additional microwave filtering. The influence of capacitor geometry on T_P has been studied with results indicating an advantage of small and tapered geometries [77–79]. Covering the transmon with a layer of Al has been shown to improve T_P [79]. In this chapter, QPP is investigated in a full-shell gatemon qubit. QPP was recently studied in a half-shell gatemon, where it was found that $T_P \sim 100\,\mu\text{s}$ and that T_P had a non-monotonic dependence on an applied magnetic field. In general, methods to mitigate QPP have included pumping schemes [80] and trapping QPs using vortices [81, 82] or regions of normal metal [83].

5.2 Measurement of poisoning time

A prerequisite for measuring the rate of parity switching in a transmon is resolving the separate parity branches of the qubit transition. As discussed in Section 2.2, operation in the regime $E_J/E_C \gg 1$ is part of the definition of the transmon (typically $E_J/E_C \sim 50$). For quantum computer applications, this regime is appealing because of its associated improvements of coherence. In this regime, however, it is hard to study QPP, due to the fact that the separation between the parity branches is intentionally suppressed[1]. Hence, in order to study QPP, transmons with an intermediate value of E_J/E_C, referred to as offset-charge sensitive (OCS) transmons, can be exploited.

For gatemons (and flux-tunable split-transmons), there is an extent to which the OCS regime can be tuned in and out of *in situ*. Since the gatemon E_J is voltage-controlled, then so is E_J/E_C. In practice, however, it is convenient to keep the transition frequency in the vicinity of the readout resonator. Therefore, a relatively small E_C should be chosen in the design of the sample. In the present work, $E_C = 500\,\mathrm{MHz}$ was chosen.

The fabrication of the gatemon sample and the experimental setup has been outlined in Chapter 3 with the full fabrication details provided in Appendix B. The sample used for the present experiment is the one referred to as Device 2 in Chapter 4, depicted in Figure 4.4b.

First, the switching rate was studied at base temperature and zero magnetic field. The qubit transition frequency was tuned by the gate voltage in order to obtain a large dispersive shift and to decrease E_J/E_C. By setting $V_C = -0.71\,\mathrm{V}$, a qubit frequency $f_{01} = 4.1\,\mathrm{GHz}$ was arrived at, as detected by two-tone spectroscopy. Next, a time series measurement of the transmission at the readout resonator at $f_{\mathrm{RO}} = 5.4\,\mathrm{GHz}$ was set up. To characterize the switching, the transmission has to be monitored for a long enough time so that several switching events are recorded, and using a sufficiently high time-resolution as prescribed by the Nyquist theorem. On the other hand, increasing the measurement duration and resolution eventually leads to problems due to memory limitations in the experimental instrumentation. In our case, the setup was bottlenecked by the AlazarTech ATS9360 digitizer. For example, although the setup allowed for time series data points to be collected at a rate of $\tau_C \sim 1\,\mu\mathrm{s}$, running such a mea-

[1] Note that this does not mean that the adverse effects of QPP are vanishing, since QPP can still impose limits on T_1.

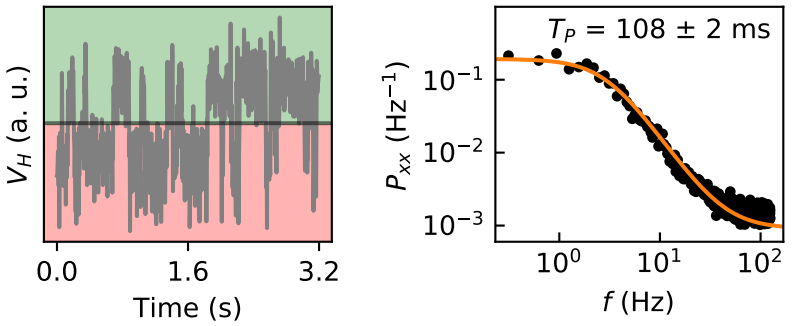

Figure 5.2: Direct monitoring of QPP and extraction of T_P. (a) Time trace of demodulated voltage V_H showing switching interpreted as QPP. (b) Average power spectral density of 40 traces as in (a). A fit to a Lorentzian function yields a poisoning time T_P as indicated.

surement for several seconds (corresponding to millions of data points) triggered a memory error in the digitizer. Since the time scale of switching events is not known *a priori*, different durations and time increments were tried until switching was observed in the resulting measurement as shown in Figure 5.2. For the trace in Figure 5.2a, the measurement lasted for 3.2 s, with adjacent data points separated by $\tau_C = 4\,\text{ms}$ (800 data points). Each data point itself consists of the average voltage recorded over a time span of $\tau_I = 100\,\mu\text{s}$. In order to increase the accuracy of the fitted T_P, the time series was measurement was repeated $N_T = 40$ times.

Taking into account both the magnitude and phase of the transmitted signal, the demodulated voltage V_H is recorded as a complex quantity. In electronics, the real and imaginary axes of the plane formed by the magnitude and phase of a signal are called *in-phase* (I) and *quadrature* (Q) respectively, and the plane is referred to as the IQ-plane. Depending on the measurement setup and non-idealities in the sample, it varies whether the measured signal lies mostly along the I or Q axis. In order to maximize the signal, the data sets were rotated in the IQ-plane to project along the axis separating the two populations, when detected. If no split population was observed in the data, which could happen for example if charge noise brings n_g to an even-odd degeneracy point, the data set was not used to extract a value of T_P (see also Figure 5.4 and surrounding discussion).

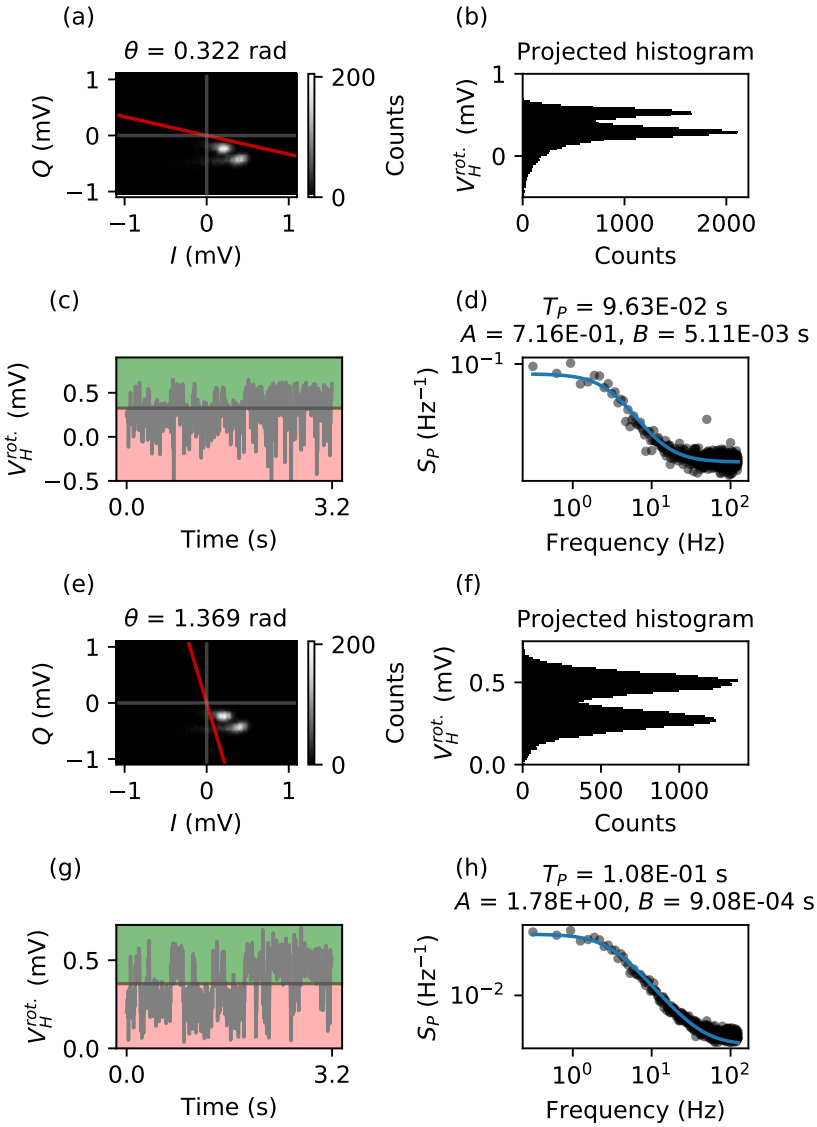

Figure 5.3: Rotation of QPP data in the IQ-plane. The parity-switching data is processed for improved signal. (a) Histogram of I and Q component of measured V_H. The line indicates a particular choice $\theta = 0.322\,\text{rad}$ of rotation angle. (b) One dimensional histogram of data projected on chosen θ. (c) Rotated data shown as time trace. (d) Fit to Lorentzian of data rotated with chosen θ. (e)-(h) Same diagrams for a different choice of θ. Based on the split population exhibiting switching appearing more isolated for $\theta = 1.369\,\text{rad}$, this angle was chosen for the data displayed here.

Figure. 5.3 shows an example of rotating data in the IQ-plane. As seen in Figure 5.3a, e the signal in this data lies mostly along the magnitude of the voltage. However, each population also has a tail-like feature, interpreted to result from residual excited-state population. The manual choice of rotation angle θ was made so that as much signal as possible was obtained, while also trying to avoid distortions such as from these tail-like features. Various automated procedures for picking such an angle were tried. It is possible that a machine learning solution could be implemented to this end; alternatively a more sophisticated measurement could be set up where all four logical-parity states are identified in the IQ-plane. However, for the purposes of the present investigation, a manual selection procedure as described above was found to be most time-efficient.

After selecting a suitable rotation angle, the data was binned following Reference [75] so that data points below the mean were set to -1 and points above the mean to 1, and the power spectral density (PSD) was computed using the FFT routine from the NumPy Python package wrapped in the following function

```
def psd(time_series, cycle_time):
    npts = len(time_series)
    nfreqs = np.fft.fftfreq(npts, cycle_time)[:(npts//2)]
    nfft = np.fft.fft(time_series)
    npsd = 2*cycle_time/npts * np.abs(nfft[:(npts//2)])**2
    return (nfreqs, npsd)
```

The mean PSD P_{xx} of all N_T traces was computed and fit to a Lorentzian form

$$S(f) = A\frac{T_P}{(\pi T_P f)^2 + 1} + B, \tag{5.1}$$

with poisoning time T_P, amplitude A and background B to account for noise in the data. The resulting P_{xx} along with the best fit is shown in Figure 5.2b.

The present measurement of $T_P \sim 100\,\mathrm{ms}$ is on the higher end of previously reported values of T_P in transmon qubits, as listed in Table 5.1. Although the factor limiting T_P was not identified, the observation of slow QPP in a gatemon sample means that it is possible to engineer large improvements of T_1 in this material system before encountering the limit set by QPP. This is an encouraging fact for the further development of nanowire gatemons as a platform for quantum information processing.

Next, the stability of T_P over time is investigated. Furthermore, the time stability of n_g is also monitored. The gate voltage is fixed at $V_C = -667\,\mathrm{mV}$,

yielding $f_{01} = 4.5\,\mathrm{GHz}$. The experiment is set up as follows. First, a two-tone spectroscopy measurement is performed. Then, the drive tone is disabled and a dispersive measurement of T_P is made as described above. This sequence is repeated for 12 h. Afterward, the T_P data is rotated in the IQ-plane, binned and fitted. The results are shown in Figure 5.4. In Figure 5.4a. The omission of T_P data points at certain segments of the diagram is due to not using data from when n_g is at the degeneracy point, as shown in Figure 5.4b. The data in Figure 5.4b reveals that n_g is fairly stable in time, showing jumps and drift on the time scale of hours. By comparing Figures 5.4a-b, it can be observed that there is no apparent correlation between T_P and n_g. Figures 5.4c-e show examples of full two-dimensional histograms of the dispersive monitoring prior to projecting onto a chosen axis. As jumps in n_g make the difference in f_{01} between the charge parities smaller (e.g. going from the situation in Figure 5.4c to the one in Figure 5.4d) the distance between the two populations decreases. This means that the driven two-tone measurement is consistent with the dispersive monitoring used for detection of T_P. At the degeneracy point (Figure 5.4e) the two populations have merged and as per the data rotation procedure, such a data set is not used for extracting T_P. In this regime, a large elongation is visible in the histogram. We presently lack an interpretation for this feature in the data. Possibly, it represents an effect favoring residual excitation or causing extra sensitivity to noise when the parities are degenerate.

5.3 Parity-selective spectroscopy

In Chapter 4, the gatemon charge dispersion was recorded in order to compare the zeroth and first Little-Parks lobes. In Figure 4.7c, the measured charge dispersion shows both parity branches of the qubit transition, due to the duration of measurement exceeding T_P. If a spectroscopy measurement can be performed faster than T_P, while still averaging enough to resolve the qubit transition, unpoisoned spectra with a single f_{01} peak can be recorded. Data from two-tone spectroscopy measurements performed in this way are shown in Figure 5.5. In Figure 5.5a, V_C is swept over a range of 1 mV, revealing the oscillatory charge dispersion of f_{01}. In this measurement, each column of data consists of 101 points in f_d, separated in time by $\tau_C = 8\,\mu\mathrm{s}$ and averaged 50 times, meaning that a single column takes a total of $101 \times 8\,\mu\mathrm{s} \times 50 = 40.4\,\mathrm{ms}$ to acquire. Since $40.4\,\mathrm{ms} < T_P \sim 100\,\mathrm{ms}$, most columns reveal only one parity branch of the qubit

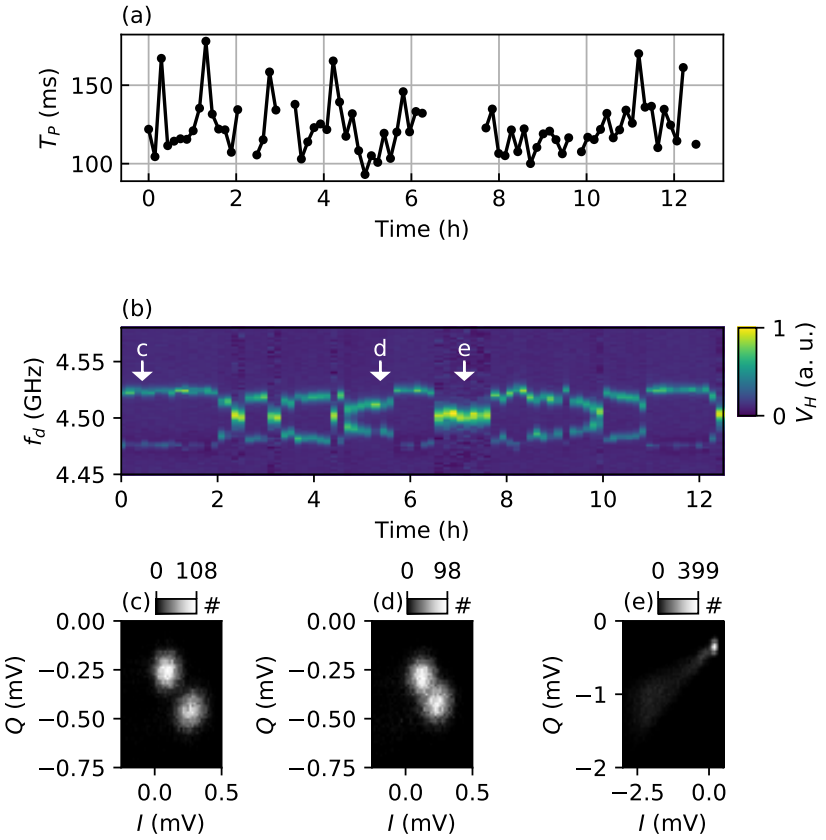

Figure 5.4: Time dependence of T_P and offset charge. Data taken over the course of several hours. (a) Variations of T_P as extracted from a fit of dispersive monitoring data to a Lorentzian function. (b) Driven two-tone spectroscopy data taken between QPP measurements in (a). Shifts in f_{01} are interpreted as charge jumps on the sample affecting the offset charge n_g. (c-e) IQ-plane histograms of QPP data from the points in time indicated in (b). The reduction of population separation from (c) through (e) is as expected from n_g in (b). Elongated features in the histogram populations, such as in (e), can generally be interpreted as resulting from residual qubit excitation. However, the reason for this feature appearing, in this case, only near the degeneracy point, is currently unknown.

transition. A few columns do exhibit the level doubling, reflecting the fact that a parity switch might occur during the period of data acquisition. In Figure 5.5b, $V_C = -656\,\mathrm{mV}$ is fixed, and the same spectroscopy measurement is repeated several times. Here, the measurement parameters are chosen such that the time taken to acquire each column of data is $51 \times 8\,\mu\mathrm{s} \times 20 = 8.16\,\mu\mathrm{s}$. Since this is smaller than in Figure 5.5a, fewer instances of doubling are expected in this case, which appears to match the observed data.

If the two-tone spectroscopy measurement is setup properly, even the gate-dependent charge dispersion of individual parity branches can be probed in isolation. To this end, the DAC controlling V_C is replaced with a waveform generator (Agilent 33600A), allowing the voltage to be rapidly ramped. A sawtooth pattern was applied from the generator with an amplitude $\Delta V_C = 1\,\mathrm{mV}$ and offset $-0.33\,\mathrm{V}$, centering the qubit frequency around 4.4 GHz.

Given the measured $T_P \sim 100\,\mathrm{ms}$, several periods of the charge dispersion is ramped (set by $\Delta V_C = 1\,\mathrm{mV}$) with a period of $\tau_R = 2\,\mathrm{ms}$, repeated and averaged 15 times for improved signal-to-noise. Accordingly, one averaged ramp takes $\tau_R \times 15 = 30\,\mathrm{ms}$. Since this is smaller than T_P, the system is likely to remain within a given parity branch for the duration of the averaged ramp. At each spectroscopy drive frequency f_d, a total of 200 such averaged ramps were recorded. The full data set, with all 200 traces averaged at each f_d, is shown in Figure 5.6a.

Due to long T_P, data can be sorted by charge-parity using post-selection. To achieve this, sorting criteria are specified, as indicated in Figure 5.6b. In this figure, the horizontal lines marked by single letters divide the data into segments (for example, the values of f_d between A and B). For ramp traces in a given segment, a vertical line indicates a value of ΔV_C associated with this segment (for example, the line labeled AB at $\Delta V_C = 0.05\,\mathrm{mV}$). For each ramp trace, the value of measured V_H at the associated ΔV_C is used to post-select that trace into either even or odd parity, depending on whether V_H at that point is above or below the mean of that trace[1]. Criteria points (vertical lines) are chosen at features unique to one of the parity branches. The result of the post-selection is shown in Figure 5.7.

As seen in Figure 5.7, the two different charge-parity branches of the qubit transition now appear in isolation from each other. This further demonstrates that the present measurement setup is capable of performing two-tone spectroscopy

[1]Note that since the charge-parity concerns the relative offset between either side of the qubit JJ, populations between which switching occurs are labeled even and odd arbitrarily.

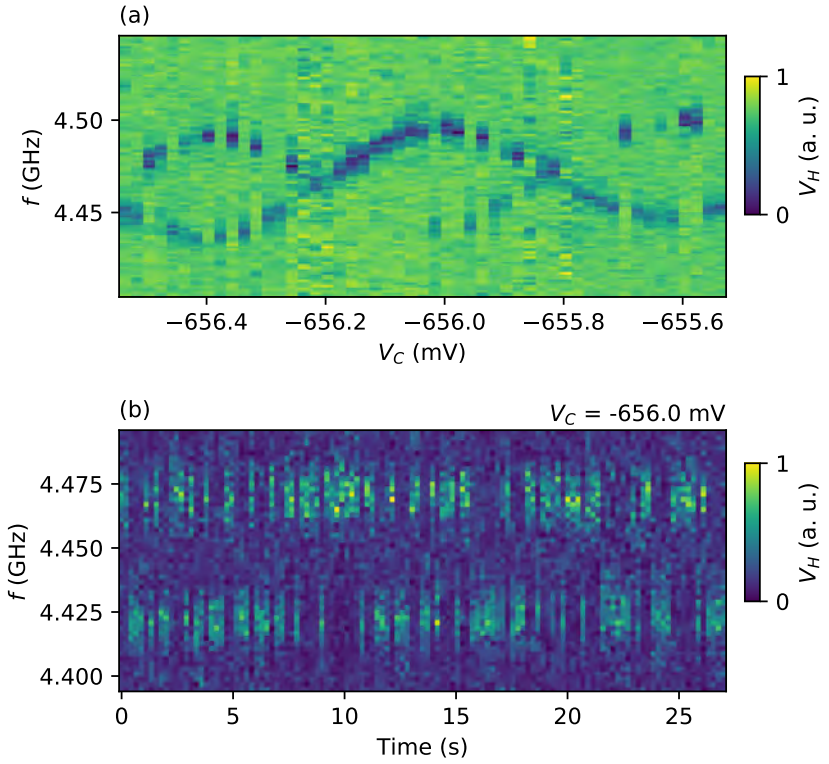

Figure 5.5: Fast spectroscopy measurements revealing an unpoisoned spectrum. Averaging is reduced to speed up the spectroscopy measurement. Measuring faster than the poisoning time T_P yields mostly single f_{01} peaks in contrast to the QPP-induced doubling. (a) Charge dispersion of f_{01}. (b) Repeated spectroscopy measurement taken away from the n_g degeneracy point.

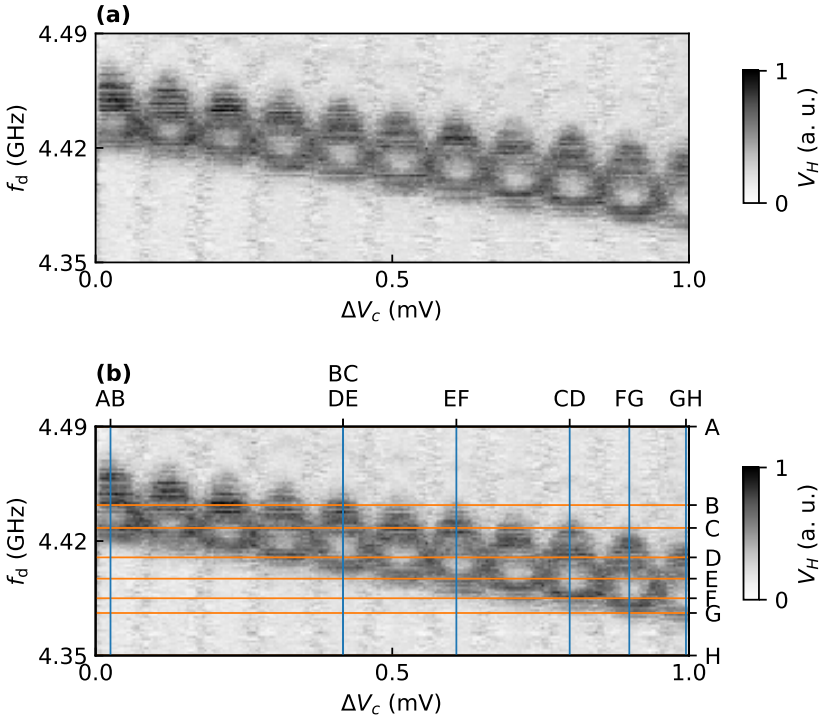

Figure 5.6: Diagram of criteria used for post-selection of spectroscopy data by parity. (a) All data. (b) Same as in (a) but including lines indicating the selection criteria used for post-selecting data by charge-parity (see main text).

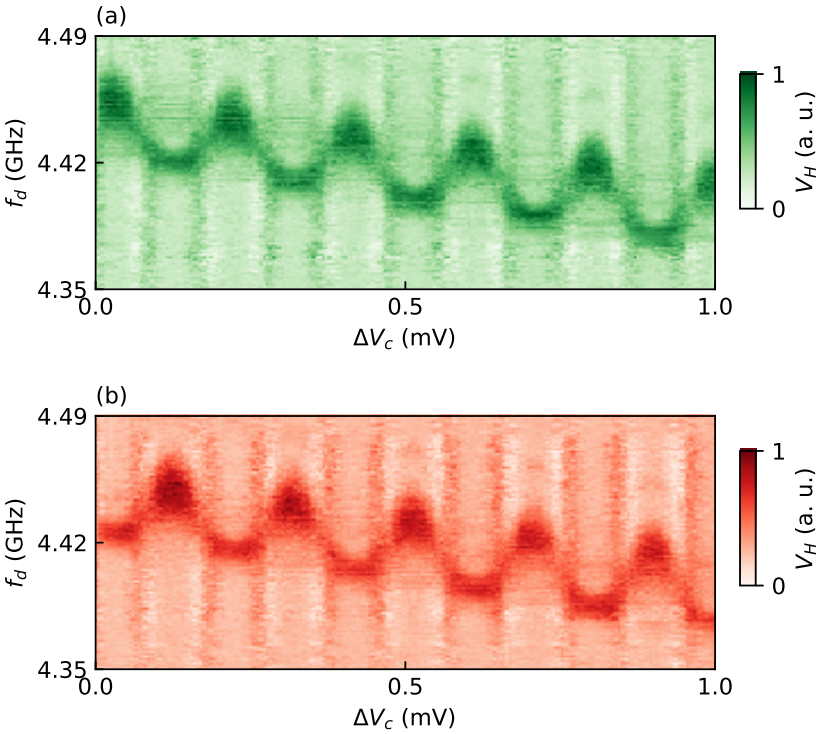

Figure 5.7: Two-tone spectroscopy data featuring the qubit transition and post-selected based on parity. (a) and (b) show the post-selected results from either parity. Vertical lines are artifacts from column average subtraction which is used for enhanced visibility.

faster than QPP and that this can be done even while probing the dependence on another quantity (here the gate voltage). The measurement of individual charge-parity states is interesting for example in the study of Andreev bound states, where another technique for parity selection was recently demonstrated [85].

5.4 Temperature-dependence of parity switching

In order to probe the nature of the QP population in the gatemon device, a temperature-dependent measurement of T_P is performed. Due to the nature of the Fermi-Dirac distribution, it is expected that the rate of QPP will increase at higher temperatures, since more QPs will be available to tunnel across the junction above the superconducting gap. In an effort to probe T_P over a wide range, different combinations of N_T, τ_C and τ_I were used at different temperatures, determined by trial and error. To avoid conflating the QPP signal with switching related to residual qubit excitation, τ_I is kept larger than the expected T_1 ($\tau_I > 20\,\mu s$ is used for all measurements of T_P, as compared to measurements yielding $T_1 \sim 5\,\mu s$, described in the subsequent section). At $V_C = -0.71\,V$, the same gate voltage as in Figure 5.2, the mixing chamber temperature was swept from base $\sim 30\,mK$ up to 140 mK and at each temperature setpoint T_P was measured after a wait time of 10 min (to allow for thermalization). As for the data in Figure 5.2, each measurement of T_P involved processing the complex raw switching data to a scalar V_H by rotation in the IQ-plane (if a split population was not observed, no T_P was assigned to this setpoint), binning, PSD computation and fit to Equation 5.1. The resulting T_P as a function of temperture T is shown in Figure 5.8. Figures 5.8b, c illustrate the fact that this measurement series involved detecting charge-parity switching over many orders of magnitude.

The behavior of $T_P(T)$ observed in Figure 5.8a is similar to what has been reported in previous transmon measurements (see e.g. References [74, 84]). As the temperature is first increased from 30 mK, T_P remains constant. At around 80 mK, it starts to decrease exponentially. The present data is interpreted in the same way as in the works cited above. At low temperatures, no thermally activated QPs are contributing to QPP. Hence, if all excited QPs in the system were due to temperature, T_P at 30 mK would be larger than observed. Saturation of T_P at low temperatures is interpreted to arise due to the existence of a non-equilibrium QP population, existing alongside thermal QPs. Non-equilibrium QPs are not suppressed by decreasing the temperature.

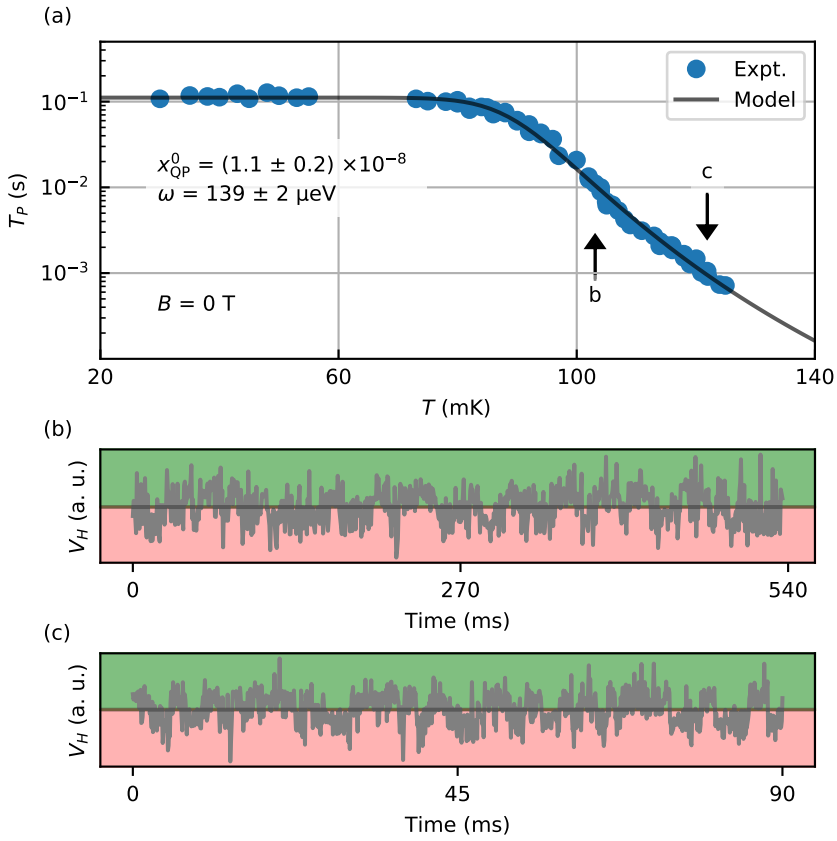

Figure 5.8: Temperature dependence of T_P. (a) Data points of measured T_P as the refrigerator temperature is increased from base temperature $\sim 30\,\mathrm{mK}$. (b) and (c) show examples of time traces as indicated in (a), showing the observation of switching at different orders of magnitude of T_P.

The total QP density x_{QP}, normalized by the density of Cooper pairs, with contributions both from non-equilibrium and thermally activated QPs can be written [86, Equation 21] as

$$x_{\mathrm{QP}} = x_{\mathrm{QP}}^{0} + \sqrt{2\pi k_B T/\omega}\exp\left(-\omega/k_B T\right) \tag{5.2}$$

where x_{QP}^{0} is the contribution from non-equilibrium QPs and ω is the superconducting gap. Assuming that the rate of charge-parity switching is proportional to the QP density, $1/T_P = C x_{\mathrm{QP}}$, and fitting to the logarithm of data points yields the solid curve in Figure 5.8a with

$$x_{\mathrm{QP}} = x_{\mathrm{QP}}^{0} = (1.1 \pm 0.2) \times 10^{-8} \quad \text{and} \quad \omega = (139 \pm 2)\,\mu\mathrm{eV}\,. \tag{5.3}$$

In comparison to similar measurements [74, 84], the measured $x_{\mathrm{QP}}^{0} \sim 10^{-8}$ is about an order of magnitude smaller, likely indicating a well-shielded sample space. The value $\omega = 139\,\mu\mathrm{eV}$ from the fit is in rough agreement with the bulk superconducting gap of Al. Note that in using Equation 5.3 to model the data, the temperature-dependence of ω is neglected. This is justified since the upper end of the temperature range in Figure 5.8a corresponds to only $\sim 10\,\%$ of the critical temperature of bulk Al.

5.5 Magnetic field evolution

Due to the full superconducting shell of the NW used for the qubit JJ, the qubit frequency exhibits destructive Little-Parks oscillations as a function of parallel magnetic field (see Chapter 4). A data set demonstrating the presence of the Little-Parks effect in the present sample is shown in Figure 5.9. Although taken with lower resolution than the data set in Figure 4.6a, it similarly shows destructive Little-Parks oscillations with the first lobe centered around 100 mT.

As discussed earlier in this thesis, the operation in a finite magnetic field is a significant aspect of the gatemon qubit. To examine the role of QPP in this context, the magnetic-field dependence of T_P can be investigated. In Figure 5.9, $f_{01}(B)$ shows oscillations reflecting the evolution of E_J. However, the pair-breaking term $\alpha(B)$ also controls the spectral gap ω, affecting the QP density of states. Therefore, QPP is expected to increase as ω is suppressed. To provide further insight into the influence of QPP on the operation of the qubit, measurements of f_{01} and relaxation time T_1 are included in the data set.

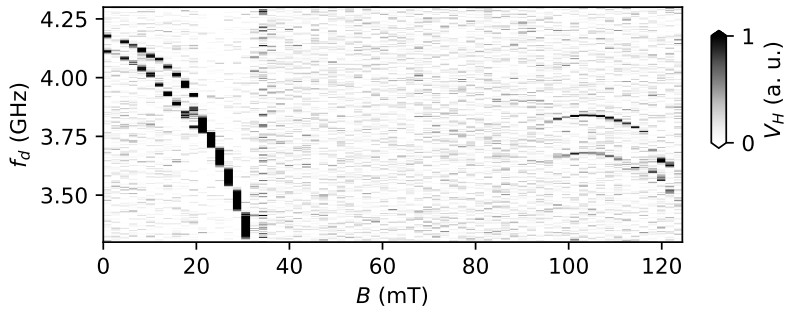

Figure 5.9: Little-Parks oscillations as measured for Device 2. For completeness, a data set featuring Little-Parks oscillations in the device for which QPP is studied is shown here. The behavior is similar to that of Device 1, as shown in Figure 4.6.

The magnetic-field dependent data set was taken as follows. At each setpoint of B, a two-tone spectroscopy measurement was first performed. From these data, f_{01} was automatically extracted. At the computed f_{01}, a Rabi pulse sequence was applied. The Rabi data was fit to exponentially damped oscillations and the π-pulse duration was extracted from the fit. A relaxation pulse sequence was then applied at the same f_{01} using this π-pulse duration. By fitting an exponential function to the relaxation data, T_1 is extracted. Finally, a dispersive measurement of T_P is performed, including the steps of data processing previously described. The resulting f_{01}, T_P and T_1 as functions of B are shown in Figure 5.10.

In Figure 5.10, the span of setpoints for B terminates in the zeroth lobe around 30 mT. As the zeroth lobe closes, all quantities become too small to measure. For f_{01}, this corresponds to no detectable peak being observed in the two-tone spectroscopy data (also resulting in no proper T_1 measurement), and for T_p it corresponds to no split population detected for any combination of N_T, τ_C and τ_I used. While f_{01} recovers around 100 mT, as shown in Figure 5.9, T_P remains too low to measure using our method. Within the zeroth lobe, the f_{01} data in Figure 5.10a exhibits the expected suppression. This data is fit to equations describing the Little-Parks effect in the same way as the data in Figure 4.6b, here yielding a NW radius $R = 90$ nm, Al shell thickness $t = 4$ nm and superconducting coherence length $\xi = 165$ nm. These values are reasonably close to those

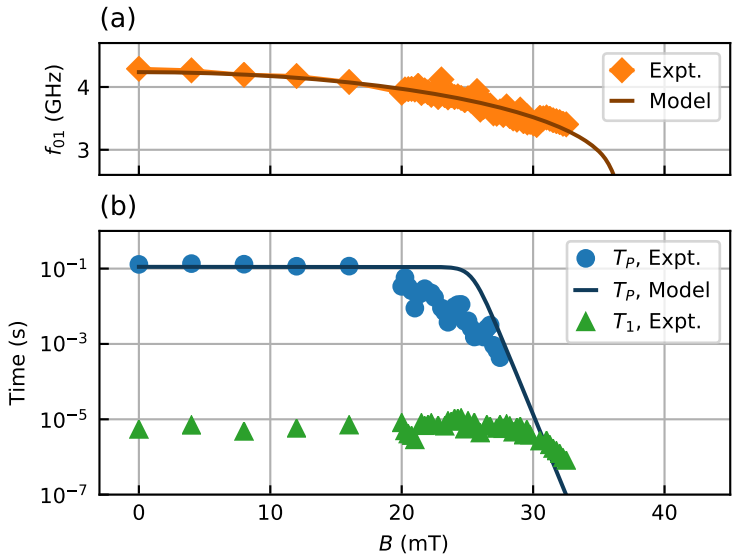

Figure 5.10: Dependence on magnetic field of T_P. Data shown here of f_{01}, T_P and T_1 are taken in a single ramp of magnetic field B by interleaved measurements. (a) Qubit transition frequency f_{01} as extracted from two-tone spectroscopy measurements. (b) Measurements of T_P by dispersive monitoring and T_1 by relaxation pulse sequence.

from the fit in Figures 4.6a, as well as those from NW TEMs in Fig. 3.1 (note the surrounding discussion), although t is significantly smaller here. Furthermore the fit involves a large number of free parameters which constrain each other, potentially resulting in fitting artifacts[1]. Nevertheless, Equation 4.3 captures the behavior of $f_{01}(B)$ for this device with reasonable parameters from the best fit.

Similar to the temperature-dependent data, the measured T_P in Figure 5.10b start at $\sim 0.1\,\mathrm{s}$ at $B = 0\,\mathrm{T}$ and initially remains constant as B is increased. Around 20 mT, there is an onset of exponential suppression of T_P as a function of B. A likely interpretation of this behavior is similar to that related to temperature-dependent data: as long as the spectral gap $\omega(B)$ remains large, the contribution to QPP from non-equilibrium QPs dominates. At larger B, thermally activated

[1]For more details, see the computational notebook attached to Reference [73].

QPs overtake and T_P is exponentially suppressed. As a rough model for this behavior, Equation 5.3 can be used with $\omega \to \omega(B)$ as governed by the pair-breaking term in Equation 4.3. Here, it is important to note that at finite magnetic field, the spectral gap ω and the pairing energy Δ are distinct quantities[1] related by [66]

$$\omega = \left(\Delta^{2/3} - \alpha^{2/3}\right)^{3/2}. \tag{5.4}$$

It is assumed here that Δ enters into Equation 2.4 and therefore controls f_{01}, while ω is the QP DOS gap in Equation 5.3. Using the values of $\omega(B=0)$, x_{QP}^0 and C from the fit in Figure 5.8a, as well as R, t and ξ from the fit in Figure 5.10a, yields the model curve for $T_P(B)$ in Figure 5.10b. As seen in the figure, the model is in rough agreement with the measured T_P data. In the data, the onset of exponential suppression of T_P occurs at slightly lower B than predicted by the simple model. One reason for this discrepancy could be that the model does not take into account changes in the functional form of QP DOS at finite magnetic field. Theory predicts a suppression and broadening of the coherence peaks with growing α (see Figure 10.2 and related discussion in Reference [62]). In Equation 5.3, the zero field DOS is assumed throughout. Softening of the superconducting gap in a finite magnetic field could lead to elevated rates of QPP, although earlier experiments indicate that the NW gap remains hard [87]. Overall, a more refined model is needed to capture the detailed behavior of the experimentally measured $T_P(B)$. To gain insight into this, a future experiment could use a gatemon device with a dc transport lead to monitor the QP DOS *in situ* and correlate this with measurements of T_P.

Figure 5.10b furthermore shows the field-dependence of T_1. This quantity undergoes a similar field evolution as T_P; it is first constant around 10 µs, and then exponentially suppressed at around 30 mT. As discussed in the beginning of the chapter, QPs tunneling across the junction carrying an energy matching the qubit transition can act to excite or relax the system. Note that the measurement of T_P reported here is specifically the rate of transition between $|0e\rangle$ and $|0o\rangle$, whereas the QPP rates relax (excite) the qubit are $|1e\rangle \to |0o\rangle$ and $|1o\rangle \to |0e\rangle$ ($|0e\rangle \to |1o\rangle$ and $|0o\rangle \to |1e\rangle$). The ratios between these rates depend on the energy distribution of QPs [74]. Nevertheless, all of the rates are affected by the QP DOS and can be expected to increase as the spectral gap is suppressed. The similar magnetic fields at which T_P and T_1 starts to exponentially decrease sug-

[1] See Figure 10.3 and the related discussion in Reference [62].

gests that QPP becomes the limiting factor for T_1 above $\sim 30\,\mathrm{mT}$ in the zeroth lobe. A measurement of T_P was attempted at the maximum of first Little-Parks lobe $B \sim 100\,\mathrm{mT}$. In this regime, a measurement of $T_1 = 0.4\,\mu\mathrm{s}$ was made, but no split population was observed in the dispersive monitoring used for measurement of T_P. This is interpreted as T_P being below the threshold of detectability in our setup, meaning not sufficiently exceeding the data integration time $\tau_I = 30\,\mu\mathrm{s}$ (here $N_T = 5$, $N_P = 2000$ and $\tau_C = 100\,\mu\mathrm{s}$). Attempts to resolve T_P in this regime of B were performed at different V_C, but no split population was observed in the V_H data. Increased rate of QPP in this regime could be caused by the appearance of subgap states associated with the the first Little-Parks lobe, as previously studied in Reference [72]. An alternative interpretation of no split population being observed in the first lobe could be a finite Majorana coupling energy E_M in the system, giving rise to the simultaneous existence of both parity branches without switching. However, reduced T_1 in the first lobe, lack of spectroscopy signatures of E_M (as investigated in Chapter 4) and previously observed increased subgap DOS [72] favors the interpretation of a small T_P.

The data in Figure 5.10 shows T_1 starting to decrease above 30 mT. As B is increased and T_1 falls below $\sim 1\,\mu\mathrm{s}$, it is not possible to keep tracking f_{01}. This is because the linewidth of the qubit transition as measured by two-tone spectroscopy is proportional to $1/T_2$ (at drive powers below the power-broadened regime) [88, p. 164]. Due to the condition $T_2 \leq 2T_1$, the peak will smear out completely as $T_1 \to 0$. Figure 5.11 shows this smearing of the spectroscopy signal around $B \sim 30\,\mathrm{mT}$. In order to further establish the connection between the suppression of T_P and T_1, Figure 5.11 shows the smearing of transition at different values of V_C. Altering V_C places the qubit transition at different frequencies. The fact that the transition appears to broaden at a similar B suggests that the decrease in T_1 is not determined by the value of f_{01}, in line with the interpretation that QPP is limiting T_1 above $\sim 30\,\mathrm{mT}$ in the zeroth Little-Parks lobe.

5.6 Conclusion

In this chapter, results from a study of QPP in a gatemon based on a full-shell NW have been presented. At base temperature, a Lorentzian fit to switching data yields $T_P \sim 100\,\mathrm{ms}$. This value is on the higher end of T_P reported in transmons and is far from limiting gatemon coherence in the near term. This observation is encouraging for the future development of gatemons as a platform for quan-

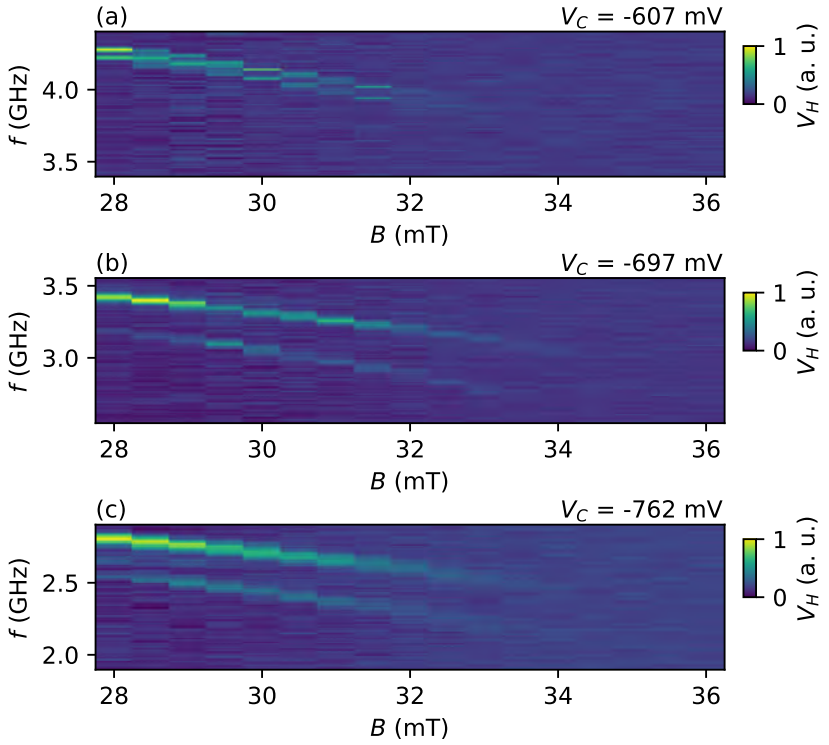

Figure 5.11: Qubit transition becoming unresolvable by spectroscopy as the magnetic field is increased. Panels (a)-(c) show two-tone spectroscopy measurements of f_{01} as a function of magnetic field B, taken at different gate voltages V_C, hence yielding different f_{01}. The disappearance of f_{01} at a similar B in all panels supports the interpretation of T_1 becoming limited by T_P around this B.

tum computation. Large T_P compared to the duration needed for spectroscopy measurements that resolve f_{01} enables post-selection based on parity, as demonstrated in this chapter.

A temperature-dependent measurement revealed a T_P that is first constant and then exponentially suppressed, supporting the picture of non-equilibrium quasiparticles limiting T_P at low temperatures. Similar behavior is observed as the magnitude of a magnetic field parallel to the NW is increased. As T_P starts to exponentially decrease around $B \sim 20\,\mathrm{mT}$, interspersed relaxation measurements

reveal a similar behavior in T_1, interpreted as the latter being limited by QPP. For future studies of QPP, the possibility of tuning into a regime where T_1 is limited by T_P could be useful. In the first lobe of the destructive Little-Parks effect $B \sim 100\,\mathrm{mT}$, a split population of V_H is not observed and hence no values of T_P are extracted from the data. The lack of a split population is interpreted as T_P being too small too resolve (similar to $B \sim 30\,\mathrm{mT}$). A likely reason for this is the increased subgap density of states in the first lobe, as observed in a separate experiment on gatemon devices based on similar full-shell NWs.

Chapter 6

Geometric control of the potential in a 2DEG-based gatemon

In situ tunability of the Josephson energy via a gate voltage is a defining feature of the gatemon qubit. This gate control has often been implemented as a single gate inducing an overall effect on channel transmissions. In this chapter, early results from ongoing work are presented, related to extending the number of gates for the purpose of detailed geometric control of the potential around the qubit Josephson junction. This could be beneficial for qubit coherence, as will be described in the beginning of the chapter. The work presented here was carried out in collaboration with A. Kringhøj, S. Budtz (it is discussed in part in Reference [89]), M. Kjaergaard and C. M. Marcus. For sample fabrication, S. N. Themadath and S. Kallatt are acknowledged. The 2DEG material was provided by the Manfra group at Purdue University.

Gatemons typically feature a single gate at the JJ, that controls the Josephson energy E_J [22, 23]. Recent exceptions to this have included NW-based devices where gating the proximitized wire segments was found to alter $f_{01}(B)$ [57] as well as with dot-forming gates used to observe the singlet-doublet transition [90]. Potentially, a gatemon with multiple gates, that form either a quantum point contact or a quantum dot in the Josephson junction, could be used to controllably achieve unity channel transmission [91,92]. In the latter case, unity transmission arises due to resonant tunneling via an energy level of the quantum dot. The

ability to fabricate gatemon devices that produce unity channel transmission under controllable conditions may offer improved ways to suppress decoherence, as outlined below.

The benefit of the conventional transmon is the exponential suppression of charge dispersion at large E_J/E_C. This suppression is advantageous to qubit coherence because charge noise causes variations in the offset charge n_g, which induces decoherence to the extent that the qubit transition f_{01} is a function of n_g. If the charge dispersion is suppressed, the qubit is protected against this source of decoherence. In the transmon, however, the exponential suppression of charge dispersion comes at the cost of decreased anharmonicity. The decrease in anharmonicity is algebraic and so for each amount of anharmonicity that is lost due to an increase in E_J/E_C, a relatively large suppression of charge dispersion can be obtained. Still, decreasing the anharmonicity limits the speed at which quantum gates can be applied. Using high-power signals to deliver faster microwave gate pulses causes leakage out of the computational states if the anharmonicity is small. For the purposes of quantum information processing, therefore, the qubit charge dispersion should ideally be suppressed without decreasing the anharmonicity. In fact, such a mechanism exists and is relevant for the gatemon platform. Due to the Landau-Zener transition between Andreev levels, the charge dispersion is expected to vanish as one of the junction channels reaches unity transmission [94]. This effect is not captured by Equation 2.1 and occurs regardless of the value of E_J/E_C.

Single-gate NW gatemons have demonstrated the suppression of charge dispersion described above [29, 30]. In these experiments, unity transmission was achieved by resonant tunneling via a level of an accidentally formed quantum dot. Accidental dots arise due to disorder in the NW material. Transport measurements have revealed a similar modulation of I_c attributed to a quantum dot resonance in carbon nanotubes [93]. In both cases, the JJ resonance is modeled using a Breit-Wigner transmission probability. If a quantum dot could be controllably formed using multiple gates at the JJ, the mechanism of suppressed charge dispersion could potentially be used at an arbitrary qubit frequency and not fixed at an uncontrolled energy associated with an accidental dot. This would be advantageous for scaling the use of this mechanism to devices with many qubits.

Based on the fact that vanishing charge dispersion is achieved when a channel reaches unity transmission, a quantum point contact could be a sufficient structure for leveraging this effect. There is, however, an advantage to forming

a controllable quantum dot in the JJ, related to the flexibility in operating parameters of the qubit. To see this, consider a gatemon with a single transmitting channel that has unity transmission. Such a qubit would have vanishing charge dispersion. The approximate energy difference is given by

$$E_{01} \approx \sqrt{8E_C E_J} - E_C \left(1 - \frac{3}{4}\frac{\sum \eta_i^2}{\sum \eta_i}\right) = \sqrt{2\Delta E_C} - E_C/4 \tag{6.1}$$

where it was used that $E_J = \Delta/4 \sum \eta_i = \Delta/4$. For a single channel with unity transmission, Equation 2.5 yields $|\alpha| = E_C/4$. Therefore the qubit transition frequency

$$hf_{01} = \sqrt{8\Delta|\alpha|} - |\alpha|\,. \tag{6.2}$$

In these calculations, the case of a single channel with unity transmission has been considered. The presence of any additional channels (whether or not they possess unity transmission) would tend to increase the qubit frequency. The expression in Equation 6.2 therefore represents the lowest possible qubit frequency, as a function of anharmonicity, in the case of vanishing charge dispersion due to a channel with unity transmission. This function is plotted in Figure 6.1 with the value of Δ chosen as that of Al. As shown in this figure, as the desired anharmonicity starts to surpass $\sim 100\,\mathrm{MHz}$ the minimum f_{01} starts to exceed the frequencies used in a typical circuit-QED measurement setup. Evidently, while achieving unity transmission in a gatemon channel is predicted to completely suppress charge dispersion, it places an experimental constraint on the qubit frequency, which might become prohibitively large depending on the desired magnitude of the anharmonicity.

Forming a controlled quantum dot in the gatemon JJ presents an opportunity to circumvent such a constraint. In the modeling of resonant tunneling via a dot level, the Δ that enters into expressions controlling f_{01} is an effective gap which can be tuned by the dot parameters [30, Supplemental material]. In this way, a quantum dot could offer a way to achieve arbitrary anharmonicity even at vanishing charge dispersion. For the present study of geometric control of the JJ potential in gatemons, the gate geometry was chosen with the formation of a quantum dot in mind.

While NWs have been the most common experimental platform for realizing gatemon qubits, the Josephson junctions in this work are formed in 2DEGs. For the purpose of forming geometrical structures in the electric potential and thereby the carrier concentration, the 2DEG material offers greater flexibility,

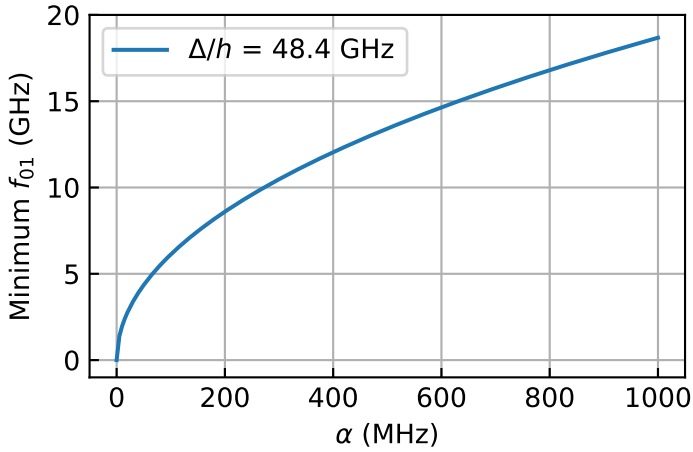

Figure 6.1: Lower bound on qubit frequency for a gatemon featuring a channel with unity transmission, assuming $\Delta/h = 48.4\,\mathrm{GHz}$ (bulk Al). A fully transmitting channel, while suppressing charge dispersion, also contributes to E_J and therefore to f_{01}. At larger anharmonicity α (achieved by increasing E_C), the lower bound on f_{01}, set by this contribution, is increasing.

since the JJ width (the dimension orthogonal to the junction) can be lithographically controlled, unlike for the NW. In general, the 2DEG is also a more scalable experimental platform, since it alleviates the need for deterministic transfer of NWs from growth wafer to device sample.

6.1 Multi-gate 2DEG gatemon

Fabrication of gatemon devices from which results are presented starts from a full 2 inch wafer with a stack of III-V materials hosting a 2DEG and grown by MBE on an InP substrate. This source material is illustrated in Figure 3.4 and is similar to that used in Reference [26]. The fabrication process is described in Section 3.2 and a technical recipe is provided in Appendix C. After cutting the wafer into $5\,\mathrm{mm} \times 5\,\mathrm{mm}$ samples, the grown III-V layers are removed by selective etching everywhere except for small patches (mesas) on the scale of $10\,\mu\mathrm{m}$. Following mesa formation, a circuit-QED control layer made up of thermally evaporated

Al is fabricated, which features a microwave feed line, readout resonators, gate lines and qubit islands. A design was used that includes three qubit-resonator pairs per sample. Josephson junctions are formed on the mesas by removing the MBE-grown Al using a wet etch process and a HfO_2 dielectric layer is deposited by ALD. Finally, Al gates climbing up the mesa are formed and interconnected by pre-deposition Kaufman milling.

In order to match the small length of the JJ, the gates in the JJ have a width on the order of 100 nm, whereas the height of the mesas are several 100 nm. Due to limitations in fabrication technology with respect to the aspect ratio of deposited metal, it is not feasible to create the narrow gates with a deposition thickness sufficiently large to climb the mesa height. Therefore, a 400 nm thick deposition is used for climbing the mesa and is connected to narrow gates on top. The resulting mesa profile is illustrated in Figure 6.2a.

The data presented in this chapter stem from measurements on three different devices. Continuing from the device labeling in preceeding chapters, these are labeled Devices 3 through 5[1]. Two of these have multiple gates shaped with the intention of forming a quantum dot in the JJ (Devices 3 and 4) as depicted in Figures 6.2b-c. In this design of the gates left and right cutter gates (V_{LC}, V_{RC}) are intended to form tunnel barriers defining the horizontal extent of the gate, depletion and plunger gates (V_D, V_H) to vertical confinement and level tuning and a helper gate (V_H) to screen the intended dot area from depletion. Device 5 has only a single gate. All devices are integrated into a circuit-QED control layer as shown in Figure 6.2d.

6.2 Initial tests

Following fabrication, the devices are mounted and loaded into a dilution refrigerator measurement setup as described in Section 3.3. As a first test of device operability, individual gates are checked for Device 3. At a high bias of $V_B = 6.8\,\mathrm{mV}$, the bias current is monitored as gates are swept to negative voltages. The results are shown in Figure 6.3. As seen in the figure, all gates show signs of carrier depletion as they become negative (increased resistance leading to lower current I_B at a fixed voltage bias). This confirms that the basic gate control of the device works as intended. As a further sign of intended device op-

[1] See Table A.1 for an overview.

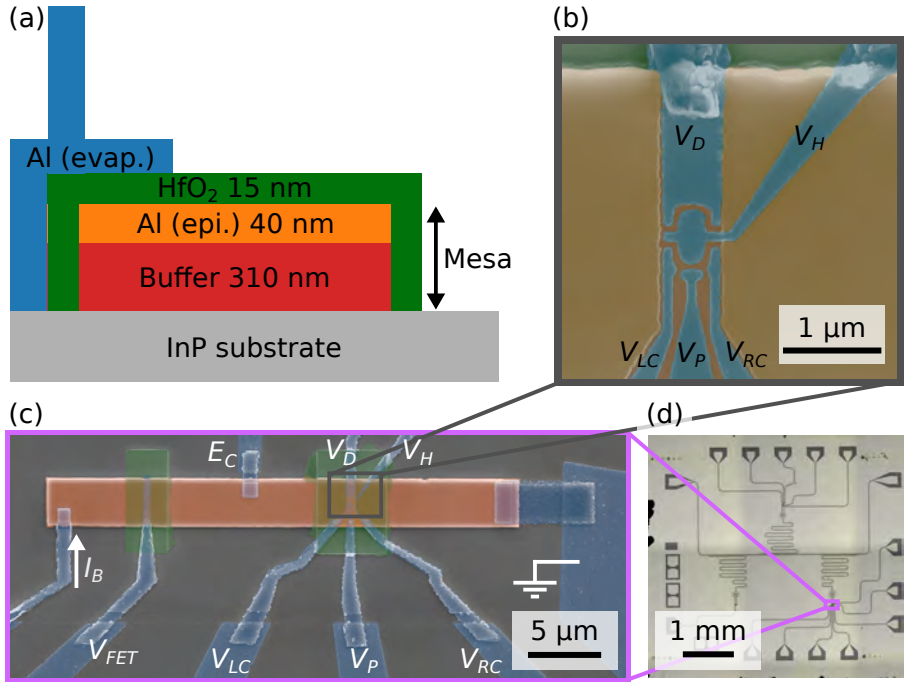

Figure 6.2: Multi-gate superconductor-semiconductor qubit formed in a 2DEG. Micrographs depict structures lithographically similar to Device 3. Device 4 does not feature the V_{FET} gate and dc transport lead. (a) Schematic of mesa profile with climbing Al gate (not to scale). (b) False-color SEM of device JJ and gates. (c) Zoomed out SEM with gates indicated. (d) Optical micrograph of surrounding circuit-QED control layer.

eration, comparing Figures 6.2b and 6.3, the degree to which each gate reduces I_B appears to match with the vertical extension of that gate.

Next, the circuit-QED operation of a similar device (Device 4) is studied. By VNA S21 measurements, the readout resonator coupled to the qubit is identified at 5.66 GHz. Several of the gates are swept to negative voltages in Figure 6.4a. Around -0.5 V, the resonator frequency starts to decrease while the linewidth is increasing. Around -0.7 V, the resonator leaves the measurement range and re-appears on the other end, decreasing in frequency as gate voltages become more negative. This behavior is interpreted as negative gates reducing E_J via

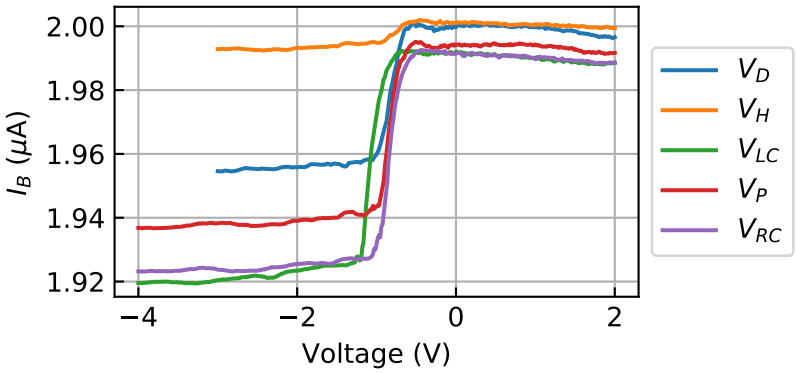

Figure 6.3: Individual gates depleting the 2DEG semiconductor. The current I_B through the JJ is monitored at a fixed voltage bias as each gate of the multi-gate 2DEG-based gatemon depicted in Figure 6.2 is swept to a negative voltage. For all gates, I_B rapidly decreases around $\sim -1\,\mathrm{V}$, interpreted as depletion of carriers in the semiconductor. Non-swept gates are set to 0 V. Data from Device 3.

channel transmissions, leading to a reduced qubit frequency via Equation 2.3. The is reflected in the frequency of the resonator through its qubit-frequency-dependent dispersive shift and an avoided crossing as the qubit and resonator frequencies coincide. Jitter in the dependence of resonator frequency on gate voltages likely reflects disorder in the material. Fixing the gates in a regime where the qubit frequency is below the bare resonator frequency, the power of the readout tone is swept in Figure 6.4b. The transition from a bare resonator frequency at high readout power, to a frequency shifted by the qubit at lower powers, is a characteristic indication that the qubit is functional and coupled to the resonator as intended.

In Figure 6.5, microwave transmission measurements are performed to probe the effect of the cutter gates on the dispersively shifted resonator, and as a starting point for using the gates to form a quantum dot in the junction. In these measurements, all other gates are fixed at negative values, in line with depleting the semiconductor everywhere except for the region under the oval-shaped part of the helper gate V_H. Here, data are taken with the digitizer through the demodulation circuit shown in Figure 3.6. The readout frequency is fixed around the center of the resonator $f_{\mathrm{RO}} = 5.661\,\mathrm{GHz}$. The transmission at f_{RO} is measured

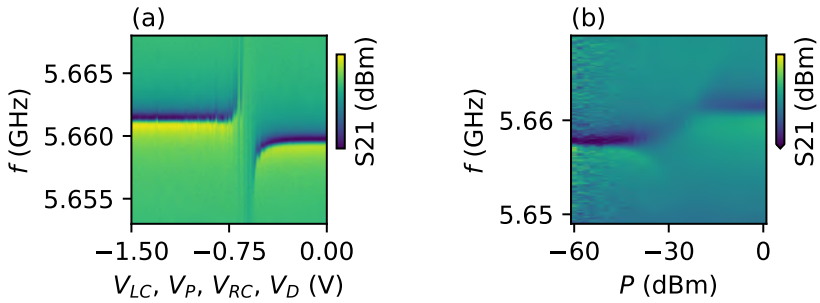

Figure 6.4: Basic demonstration of circuit-QED operation of multi-gate 2DEG gatemon device. (a) Gate-dependence of readout resonator coupled to qubit. The helper gate is fixed at $V_H = -0.6\,\mathrm{V}$ and other gates are swept together. As the qubit frequency passes through the bare resonator frequency, an avoided crossing is observed. (b) Power-dependence of resonator in a gate regime where $f_{01} > f_{\mathrm{RO}}$; here $V_D = V_P = -0.68\,\mathrm{V}$ and $V_{LC} = V_{RC} = -0.25\,\mathrm{V}$. Data from Device 4.

as a function of V_{LC} and V_{RC}. The results reveal that the cutter gates can be used to suppress f_{01}, at least to the extent that can be probed by the dispersive shift at f_{RO}, given that the other gates are sufficiently negative, as in Figure 6.5c. As V_{LC} and V_{RC} become more negative in Figure 6.5c, less gate-dependent features appear in the data, indicating a suppression of E_J, since f_{01} has presumably been so detuned from f_{RO} that the dispersive shift is undetectable. In Figure 6.5, no periodic diagonal features are observed close to the depleted regime. Such features could be associated with the presence of a quantum dot in the junction. This is because levels successively tuned onto resonance would cause increased f_{01} due to large transmission and those levels should be tunable by any gate near the quantum dot (cf. the gate-dependence of I_c reported in Reference [93]). The absence of such features in Figure 6.5c suggests that more careful tuning is necessary to form a quantum dot in the junction. A large degree of non-monotonicity as a function of either gate can be observed, indicative of noise in the material.

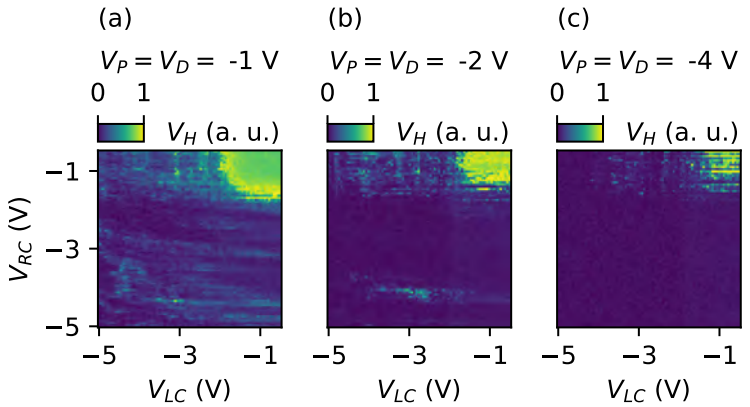

Figure 6.5: Circuit-QED response to depleting gate voltages on either side of the Josephson junction. Features at negative cutter gates indicate non-monotonicity in the gate-dependence of critical current. Panels (a)-(c) show the same measurement repeated at progressively more negative values of V_P and V_D. In all panels $V_H = -0.6\,\mathrm{V}$. Data from Device 4.

6.3 Time domain

The investigation of multi-gate 2DEG gatemon is motivated by the possibility of forming a quantum dot and using it to increase the qubit coherence time. A demonstration of enhanced coherence time due to suppression of charge dispersion presupposes that other mechanisms of energy and phase relaxation do not dominate, and especially that the qubit is coherent enough for T_1 and T_2 to be measured in the first place. To determine the state of coherence in the 2DEG device, a series of time domain measurements is performed.

On Device 3, the FET gate is set to $-4\,\mathrm{V}$ in order to isolate the qubit from the DC circuitry for high-frequency measurements. Time domain measurements are performed at a qubit frequency of $f_{01} = 2.8\,\mathrm{GHz}$. To place the qubit transition at this value, a gate configuration is applied as follows: $V_H = -0.8\,\mathrm{V}$, $V_D = -3\,\mathrm{V}$, $V_P = -3.27\,\mathrm{V}$, $V_{LC} = V_{RC} = -1.75\,\mathrm{V}$. After determining f_{01} by two-tone spectroscopy, a Rabi pulse sequence is applied as a function of drive frequency f_d in the vicinity of f_{01}. This two-dimensional measurement resulted in the "chevron" patterned oscillations as shown in Figure 6.6a. With a π-pulse duration extracted

from the trace at $f_d = 2.84\,\text{GHz}$ (Figure 6.6b), a relaxation experiment is performed at this drive frequency, yielding a decay shown in Figure 6.6c. Also shown in this figure is the best fit to an exponential function, with $T_1 = 0.15\,\mu\text{s}$. Next, using a Ramsey pulse sequence, an attempt to measure the coherence time T_2 was made. Figure 6.6 shows the results of this measurement. In the measured data, Ramsey fringes are observed, but the signal-to-noise ratio is deemed too poor to attempt a fit to the data; by eye, it appears that $T_2 \sim 10\,\text{ns}$. Although not quantitatively characterized, the signal-to-noise ratio in the two-tone measurement data (as seen e.g. in Figure 6.6a) appears smaller than in corresponding measurements on other types of samples in similar measurement setups.

The measured relaxation and coherence time are significantly smaller than the corresponding values for the 2DEG-based gatemon measured by Casparis *et al.*, who reported $T_1 \sim 1\,\mu\text{s}$ and $T_2 \sim 0.4\,\mu\text{s}$ [26]. The small time scales measured here approach the limit of what can be readily measured by the standard instrumentation currently used in our laboratory for circuit-QED measurements. This presents a problem for studying effects enhancing T_2, such as the resonant tunneling regime of interest to the present investigations. There could be several possible reasons for poor qubit performance as compared to Casparis *et al.*. In order to rule out any mechanisms of decoherence imposed by the measurement setup, an externally fabricated all-metal transmon reference sample was loaded into the same setup used for 2DEG gatemon devices. Time domain measurements on this all-metal transmon device yielded $T_1 \sim 100\,\mu\text{s}$ and $T_2 \sim 20\,\mu\text{s}$, establishing that neither the refrigerator hardware nor instrumentation are bottlenecking the coherence times.

The devices discussed so far have multiple gates near the Josephson junction, whereas those studied by Casparis *et al.* had only a single one. It is possible that additional gates could limit T_1 by providing a means for energy to be transported away from the qubit to the environment. A reference device (Device 5, fabricated on the same physical sample as Device 3) featuring only a single gate was used to test whether small T_1 and T_2 could be attributed to the large number of gates. A micrograph and time domain measurements of this reference device are shown in Figure 6.7. The measured $T_1 = 0.18\,\mu\text{s}$ is similar to that of the multi-gate device. A Ramsey pulse sequence measurement (not shown) on Device 5 further revealed poor-signal fringes with an apparent $T_2 \sim 20\,\text{ns}$, also similar to the multi-gate device. These results indicate that the presence of many additional gates is not the cause of small coherence times in the 2DEG-based

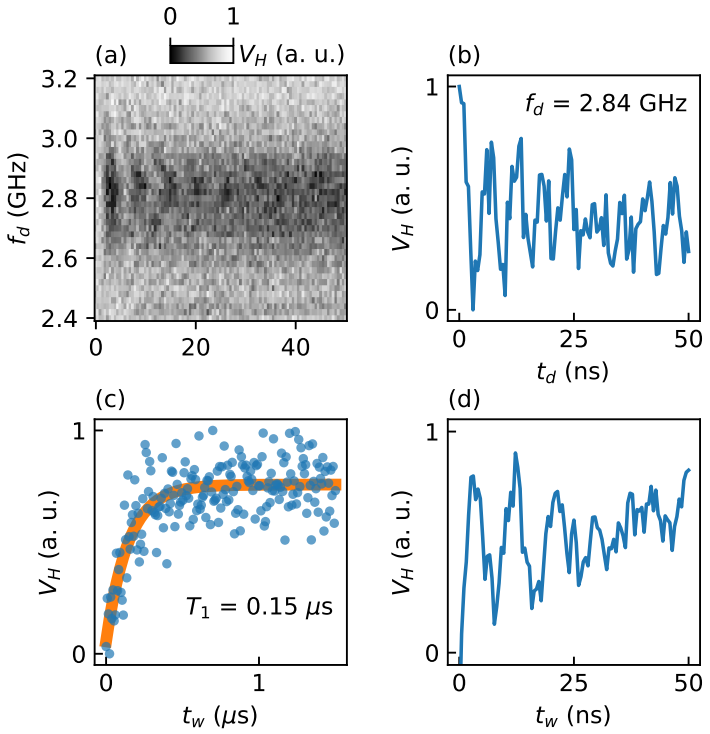

Figure 6.6: Time domain measurements of multi-gate 2DEG gatemon. (a) Rabi oscillations probed at different drive frequencies f_d yielding a characteristic "chevron" pattern. (b) Line cut of (a) at indicated drive frequency. (c) Relaxation experiment at $f_d = 2.84\,\text{GHz}$, displayed along with a fit to an exponential decay giving a relaxation time $T_1 = 0.15\,\mu\text{s}$. (d) Ramsey experiment. A three-point moving average filter has been applied to these data for improved signal visibility. Due to low signal-to-noise ratio, no fit is applied to data. Data from Device 3.

gatemon devices studied here.

Time domain measurements on the single-gate device were repeated at different qubit frequencies; at $V_G = -557\,\text{mV}$ yielding $f_{01} = 6.8\,\text{GHz}$ and at $V_G = -539\,\text{mV}$ yielding $f_{01} = 8.9\,\text{GHz}$. Larger T_1 or T_2 were not measured in either of these two regimes of f_{01}. This observation likely means that low coherence

times measured for the present devices are not a result of picking an unfavorable gate regime, and also not due to a temporary effect, since these measurements were spaced out by several hours.

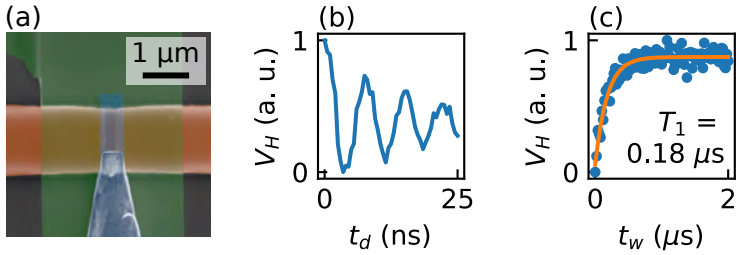

Figure 6.7: Reference measurement of relaxation time in single-gate 2DEG qubit. (a) False-color micrograph of single-gate device. (b) Coherent oscillations measured by applying a Rabi pulse sequence to the qubit. (c) Relaxation measurement yielding $T_1 = 0.18\,\mu s$. Here $V_G = -572\,mV$ and $f_d = 3.85\,GHz$. Data from Device 5.

Measurements in dc transport could offer insights into the reason for small coherence times and overall device behavior. To this end, the FET gate of Device 3 is opened by setting $V_{FET} = 0\,V$, which connects the qubit Josephson junction to the transport-measurement circuitry as shown in Figure 3.7. The differential resistance dR was then studied as a function of current bias I_B, as the qubit JJ was closed by applying negative values on a pair of gates on either side of the JJ, here chosen as V_{LC} and V_D. Resulting data are shown in Figure 6.8. These measurement data reveal characteristics of the device as the JJ nears depletion and the channel transmissions are approaching zero as V_{LC} and V_D become more negative. At $V_H = -0.6\,V$ (Figure 6.8a) and before depletion (at $V_{LC} = V_D = -1.20\,V$), $dR = 0\,k\Omega$ around zero bias, due to the superconducting state of the junction. As I_B is increased, dR suddenly increases. This is interpreted as I_B reaching the switching current I_S of the system. At $I_B > I_S$, the JJ has a finite resistance associated with the normal state of the material. The switching current I_S is directly related to the critical current $I_c = 2eE_J/\hbar$, affecting the qubit frequency f_{01} via Equation 2.3. The exact conversion between I_S and I_c depends on the details of the system and the setup [32].

In Figure 6.8a, an initial decrease in I_S is followed by a saturation around $V_{LC} = V_D = -1.35\,V$. A likely interpretation of this is that the I_S at which satu-

ration occurs corresponds to the area under the V_{LC} and V_D gates being depleted, while the small area between them are still populated with carriers and screened by the Al of the V_H gate. This screening prevents further depletion of the JJ, at least in the experimental range of Figure 6.8a. As V_H is tuned more negatively in Figure 6.8b, an increased reduction of I_S is observed, as expected from the effect of depletion from V_H. At $V_H = -1\,\mathrm{V}$ (Figure 6.8c) zero channel transmission is reached around $V_{LC} = V_D < -1.35\,\mathrm{V}$. Qubit operation of the device is performed at finite I_c. In previous experiments, qubit transition frequencies suitable for standard high-frequency operation have been associated with $I_S \sim 5\,\mathrm{nA}$ [32]. However, examining the present device behavior in this regime (Figure 6.8b, d) a finite resistance at zero bias is observed. The origin of this resistance at finite I_S is not presently understood. This resistance is potentially linked to poor coherence in the devices, as qubit operation relies on the dissipationless nature of the superconduting state, and loss of energy through dissipation could limit T_1. Further investigation into the origin of the zero bias resistance could possibly improve the performance of these qubit devices.

For completeness, the zero bias differential resistance is measured as the junction is depleted using a variety of gates as shown in Figure 6.9. In these measurements, the same behavior is observed regardless of the choice of gates used to close the junction. Ideal behavior here should appear as a single switch to very high resistance as $I_S = 0$. Instead, Figure 6.9a-f show slow onsets of resistance as the gates voltage become more negative. In Figure 6.9g-i, sudden transitions to high resistance are observed, however, this is likely due to V_H already having depleted all of the semiconductor not covered by the gates swept on the axes.

6.4 Conclusion

As mentioned in the beginning of this chapter, the work presented here is part of an ongoing study. Further research is necessary to answer the question of whether a 2DEG-based gatemon can be used to controllably host a gate-defined quantum dot, which could potentially be leveraged to extend the qubit coherence time. In particular, efforts to tune the gate and confirm the presence of a quantum dot are in progress and not reported on here. Furthermore, time domain measurements reveal that the coherence time of the present devices seems shorter than what has been reported in the past for similar samples.

Despite the principal question regarding controlled resonant tunneling being unresolved, the work performed so far produces a number of insights into the problem. The observation of coherent oscillations, albeit concomitant with small T_1 and T_2, shows that the presence of several additional gates do not prohibitively reduce qubit coherence beyond detectability by standard instrumentation. This is engouraging of experimental efforts to engineer improvements to the devices, e.g. by different choice of materials, modifications of the geometric design or changes to the fabrication procedure. The observation of finite differential resistance at zero bias, in a regime of switching current relevant for qubit operation, might be an indication of the origin of low coherence times. Since it has been demonstrated that the relevant quantities can be readily measured, it is straightforward to conduct tests of whether any given alteration of the fabrication process produces improved or deteriorated performance.

One aspect of device fabrication that could be linked to reduced coherence is the Kaufman milling. In the current device design, the wide gate segments that climb the III-V mesa are connected to narrow gate terminals on top of the mesas. The Al making up the gates forms an insulating native oxide, which needs to be removed for the subsequently deposited Al to make electrical contact. This removal is achieved by Kaufman milling immediately prior to the second evaporation of Al. While effectively facilitating the connection of Al layers, milling produces disorder in the surface, which could expose the qubit Josephson junction to additional TLSs that could limit T_1. To the extent possible, it is therefore advantageous to avoid milling close to the JJ. There are at least two feasible ways to achieve this for the type of devices considered in this experiment. First, the geometry could simply be changed so that the connection between wide and narrow gate segments is made further away from the JJ. This would require longer narrow gates on top of the mesas but would reduce the exposure of the JJ to regions of milled Al. Second, by engineering the mesa etch process it could be possible to achieve a slanted mesa profile, which would relieve the requirements on deposition thickness for the Al layer climbing the mesa. If a sufficiently gradual profile was achieved, it would be possible to eliminate the need for milling in the vicinity of the mesa altogether, potentially improving qubit coherence.

For the issue of low signal-to-noise ratio in two-tone measurements, a systematic and quantitative analysis of the setup and data is needed to gain a better understanding of the problem. A straightforward way to achieve some improvement could be to integrate a travelling-wave parametric amplifier into the readout

line of the refrigerator, which was not available in the laboratory at the time of the experiment. Another venue through which signal-to-noise ratio could potentially be increased is by improving the microwave environment of the circuit-QED system by including crossovers in the control layer. Initial tests of this, however, did not demonstrate an improvement for the devices studied in this experiment [89]. It should be noted that the devices used in the study by Casparis *et al.* did not feature crossovers.

In conclusion, 2DEG-based gatemon devices with multiple gates have been fabricated and the basic operation of these devices have been demonstrated, including the observation of coherent oscillations and *in situ* dc transport measurements. Further work is necessary to investigate the possibility of using the gates to form a quantum dot as well as to engineer improvements to T_1 and T_2. Given further progress, the type of devices introduced here could potentially be used to implement novel ways of enhancing qubit coherence.

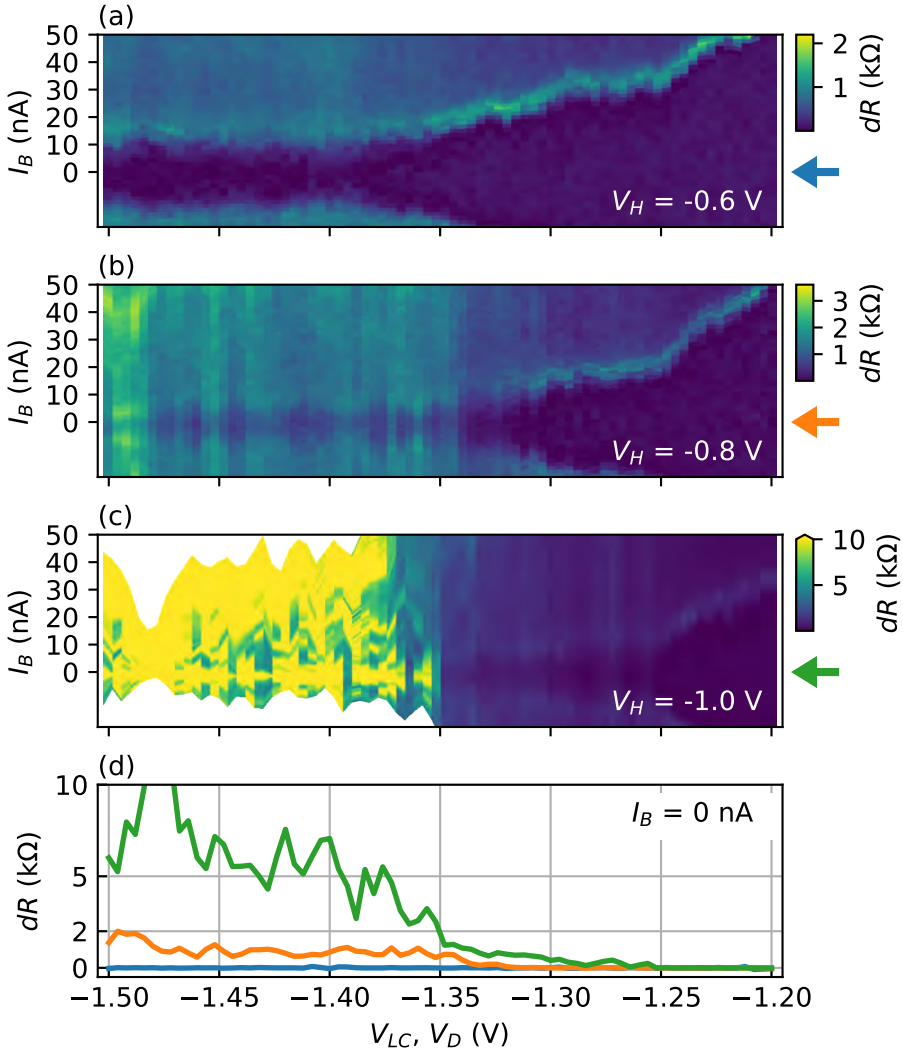

Figure 6.8: Current-bias transport measurent of closing gates Panels (a)-(c) show the same measurement at different values of V_H as indicated. For all measurements $V_{RC} = V_P = 0\,\mathrm{V}$. The gates V_{LC} and V_D depleting the semiconductor JJ shows up as a decrease of the switching current, detected in each column as the I_B for which dR suddenly increases. Note that the color scale of (c) is capped at $10\,\mathrm{k\Omega}$. Panel (d) shows line cuts at $I_B = 0\,\mathrm{nA}$. Data from Device 3.

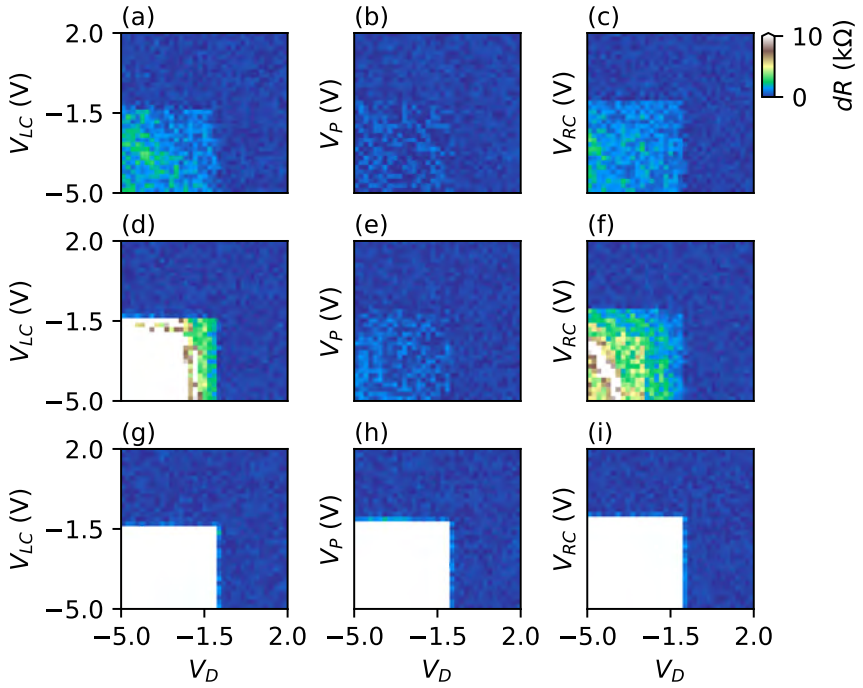

Figure 6.9: Differential resistance dR at zero bias with different pairs of gates depleting the junction. Each column in the grid of panels show V_D paired with a gate on the opposite side of the mesa (a)-(c) $V_H = 0\,\mathrm{V}$. No selection of gates fully closes the junction ($dR >\sim 10\,\mathrm{k\Omega}$). (d)-(f) $V_H = -0.5\,\mathrm{V}$. Only V_D paired with V_{LC} closes the junction. (g)-(i) $V_H = -1\,\mathrm{V}$. At this value of V_H, any pair of gates closes the junction. Data from Device 3.

Chapter 7

Outlook

In this thesis, results from three experiments related to decoherence in gatemons have been presented. None of them directly involves the engineering of improved coherence times but all of them have consequences for how this could be approached in future research.

In Chapter 4, the absence of a signature of Majorana zero modes (MZMs) in a full-shell gatemon was reported. The ability to place an upper bound on the Majorana coupling energy E_M means that in this case, the gatemon platform was able to deliver information about the extent to which MZMs are present in the sample. While MZMs in this case seemed absent within the detectable range of the experiment, the platform is ready for another test if a breakthrough in theroretical understanding of MZMs or materials science is achieved. The upper bound established in the present experiment hopefully sheds light on the conditions needed for observing E_M in a circuit-QED experiment.

Chapter 5 investigated quasiparticle poisoning (QPP) in a full-shell nanowire-based gatemon. The observation of a large poisoning time

$$T_P \sim 100\,\mathrm{ms} \gg T_1 \sim 10\,\mu\mathrm{s} \tag{7.1}$$

at low temperatures means that QPP is not an inevitable near-term barrier in the engineering of coherence times of nanowire-based gatemons. Further research might consider ways in which superconductor-semiconductor hybrid elements could be used to mitigate QPP. For such experiments, it is of interest to be able to tune into a regime where T_P appears to limit T_1, as was observed at finite magnetic field in this experiment.

The 2DEG-based gatemon project in Chapter 6 needs more work to resolve the questions it set out to answer. However, the results presented form a proof of principle regarding the possibility to concentrate a large number of gates near the Josephson junction without completely suppressing qubit coherence. The data from transport measurements may be helpful for improving the coherence times of the devices. If developed further, it is possible that 2DEGs could become a preferred choice over NWs as a superconductor-semiconductor material for applications in quantum information, due to the inherent benefit in terms of scalability.

Appendices

Appendix A

Table of devices

Table A.1 provides a list of devices discussed in the thesis. Each device represents an individual gatemon qubit. The devices are fabricated on separate physical samples, except for Device 3 and Device 5, which appear on the same sample.

Table A.1: Table of devices. An overview of devices discussed in this thesis.

Device name	**Note**
Device 1	VLS NW gatemon. Chapter 4.
	Internal lab label `IEc_05A_SWnw (Q6)`.
Device 2	VLS NW gatemon. Chapters 4 and 5.
	Internal lab label `IEc_05ESP_Q018C_NWsw (Q5)`.
Device 3	2DEG gatemon (multi-gate, with dc lead). Chapter 6.
	Internal lab label `M04-16-20_1-M15_qubit2 (Q3)`.
Device 4	2DEG (multi-gate, no dc lead). Chapter 6.
	Internal lab label `M04-16-20_1-M11_qubit1 (Q2)`.
Device 5	2DEG (single-gate, no dc lead). Chapter 6.
	Internal lab label `M04-16-20_1-M15_qubit2 (Q1)`.

Appendix B

Fabrication recipe: NW device

This appendix outlines the fabrication of Device 2, discussed in Chapters 4 and 5. The steps below describe the fabrication at local facilities, starting from a Si wafer with a layer of NbN patterned into a circuit-QED control layer and with gate dielectric below the gates. This initial fabrication was performed at Espoo, for which Mahesh Kumar, Rizwan Ali, Tommi Riekkinen, and Pasi Kostamo are acknowledged. For the subsequent fabrication Marina Hesselberg, Karthik Jambunathan, Robert McNeil, Karolis Parfeniukas, Agnieszka Telecka, Shivendra Upadhyay and Sachin Yadav are acknowledged.

Top gate dielectric and crossover dielectric

- Spin EL13, 45 s, 4000 rpm. Bake 60 s, 185 °C.
- Spin A4.5, 45 s, 4000 rpm. Bake 60 s, 185 °C.
- EBL pattern exposure, 10 nA.
- Develop MIBK:IPA 1:3 60 s, IPA 15 s. Ash, 60 s.
- ALD, HfO_2, 150 cycles, 110 °C.
- Lift-off, NMP, 2 h. Additional wet processing for lift-off completion.
- Ash, 120 s.

Nanowire deposition and junction etch

- Micromanipulator, deterministic NW transfer.
- Ash, 60 s.
- Spin AR300-80 New, 45 s, 4000 rpm. Bake 120 s, 115 °C.
- Strip Dioxolane 120 s, Acetone 120 s, IPA 30 s.

- Spin EL9, 45 s, 4000 rpm. Bake 180 s, 185 °C.
- EBL pattern exposure, 3 nA.
- Develop MIBK:IPA 1:3 $\sim$ 20 s, IPA 20 s. Ash 60 s.
- Bake (Re-flow), 60 s, 125 °C.
- Etch MF321 53 s. Milli-Q 30 s (Ultra-sound 80 kHz, 30 % Power). Dioxolane 120 s, Acetone 120 s, IPA 30 s. Ash 60 s.

Crossover crosslink

- Spin A4, 45 s, 4000 rpm. Bake 120 s, 115 °C.
- EBL pattern exposure (large dose), 100 nA.
- Develop MIBK:IPA 1:3 60 s, IPA 10 s, Milli-Q 30 s.

Contacts and crossover metal

- Spin A4, 45 s, 4000 rpm. Bake 120 s, 115 °C.
- Spin A4 (second layer), 45 s, 4000 rpm. Bake 120 s, 115 °C.
- EBL pattern exposure, 10 nA.
- Develop MIBK:IPA 1:3, 75 s, IPA 10 s. Ash 120 s.
- Kaufman mill. Sputtering NbTiN $\sim$ 170 nm.
- Lift-off NMP 4 h, 80 °C. Additional wet processing for lift-off completion.

Dicing and wire bonding

- Spin AZ9260m, 45 s, 4000 rpm.
- Bake 60 s, 115 °C.
- Dicing into samples suitable for dilution refrigerator measurements.
- Rinse IPA 5–10 s, Acetone 5–10 s.
- Strip Acetone 10 min, IPA 60 s. Ash 120 s.
- Glue to PCB using Epoxy, let dry 60–90 min.
- Wire bonding.

Appendix C

Fabrication recipe: 2DEG device

In this appendix, the fabrication steps of Device 3 are provided. This device appears in Chapter 6. The processing starts from a sample cut out from the III-V growth wafer hosting a 2DEG, for which the Manfra group at Purdue University is acknowledged. Sangeeth Kallatt and Smitha Nair Themadath are acknowledged for subsequent fabrication at local facilities as detailed here.

Alignment marks

- Spin A4, 45 s, 4500 rpm. Bake 120 s, 185 °C.
- EBL pattern exposure, 500 pA.
- Develop MIBK:IPA 1:3, 60 s, IPA 20 s. Ash 60 s.
- Metal evaporation, Ti 5 nm, Au 40 nm.
- Lift-off Dioxolane 1 h, IPA 30 s.

Mesa etch

- Spin A4, 45 s, 4500 rpm. Bake 120 s, 185 °C.
- EBL pattern exposure, 45 nA.
- Develop MIBK:IPA 1:3 30 s, IPA 10 s. Ash 60 s.
- Bake (Re-flow) 120 s, 115 °C.
- Al etch. Transene D 14 s, 50 °C. Milli-Q 20 s, 50 °C. Milli-Q 40 s (Room temperature).
- III-V etch. Etch 10 min in mix of 220 mL citric acid, 55 mL Milli-Q, 3 mL H_3PO_4 and 3 mL H_2O_2. Rinse twice in Milli-Q, 30 s each.
- Strip Dioxolane 30 min, Acetone 5 min, IPA 30 s.

Control layer Inner parts (Lift-off)

- Spin EL9, 45 s, 4500 rpm. Bake 120 s, 185 °C.
- Spin A4, 45 s, 4500 rpm. Bake 120 s, 185 °C.
- EBL pattern exposure, 1 nA and 20 nA.
- Develop MIBK:IPA 1:3 $\sim$ 30 s, IPA 5 s. Ash 60 s.
- Metal evaporation, Al 100 nm.
- Lift-off Dioxolane overnight. Additional wet processing for lift-off completion.

Control layer Outer parts (Etch)

- Spin A4, 45 s, 4500 rpm. Bake 120 s, 185 °C.
- EBL pattern exposure, 500 pA, 1 nA and 20 nA.
- Develop MIBK:IPA 1:3 $\sim$ 30 s, IPA 10 s. Ash 60 s
- Bake (Re-flow) 120 s, 115 °C.
- Al etch. Transene D 15 s, 50 °C. Milli-Q 20 s, 50 °C. Milli-Q 60 s (Room temperature).
- Strip Dioxolane 30 min, Acetone 5 min, IPA 2 min.

Junction etch

- Spin A4, 4500 rpm. Bake 120 s, 185 °C.
- EBL pattern exposure, 100 pA.
- Develop MIBK:IPA 1:3 45 s, IPA 10 s. Ash 60 s.
- Bake (Re-flow) 120 s, 115 °C.
- Al etch. Transene D 10 s, 50 °C. Milli-Q 20 s, 50 °C. Milli-Q 40 s (Room temperature).
- Strip Dioxolane 1 h, Acetone 5 min, IPA 30 s.

Gate dielectric

- Spin A4, 45 s, 4500 rpm. Bake 120 s, 185 °C.
- EBL pattern exposure, 500 pA.
- Develop MIBK:IPA 1:3 45 s, IPA 10 s. Ash 60 s.
- ALD HfO_2, 150 cycles, 90 °C.
- Lift-off Dioxolane overnight. Additional wet processing for lift-off completion.

Inner gates (Thin)

- Spin A4, 45 s, 4500 rpm. Bake 120 s, 185 °C.
- EBL pattern exposure, 100 pA.

- Develop MIBK:IPA 1:3 $\sim$ 45 s, IPA 5 s. Ash 60 s.
- Metal evaporation Ti 5 nm, Al 45 nm.
- Lift-off Dioxolane overnight. Additional wet processing for lift-off completion.

Outer gated (Thick)

- Spin EL9, 45 s, 4500 rpm. Bake 120 s, 185 °C.
- Spin EL9 (second layer), 45 s, 4500 rpm. Bake 120 s, 185 °C.
- Spin A4, 45 s, 4500 rpm. Bake 120 min, 185 °C.
- EBL pattern exposure, 500 pA.
- Develop MIBK:IPA 1:3 60 s, IPA 10 s. Ash 60 s.
- Kaufman mill. Metal evaporation Ti 10 nm, Al 390 nm.
- Lift-off Dioxolane overnight. Additional wet processing for lift-off completion.

Wire bonding

- Glue to PCB using A4, let dry overnight.
- Wire bonding.

Bibliography

[1] R. P. Feynman. Simulating physics with computers. *International Journal of Theoretical Physics*, 21(6/7):467, 1982.

[2] S. Savin. Physicists criticise University of Copenhagen's new NATO ties. *University Post*, 2022.

[3] L. Degn and M. P. Sørensen. From collegial governance to conduct of conduct: Danish universities set free in the service of the state. *Higher Education*, 69(6):931–946, 2015.

[4] Hofmann. *Solid State Physics An Introduction*. 2015.

[5] B. Josephson. Possible new effects in superconductive tunnelling. *Physics Letters*, 1(7):251–253, 1962.

[6] M. H. Devoret and R. J. Schoelkopf. Superconducting Circuits for Quantum Information: An Outlook. *Science*, 339(6124):1169–1174, 2013.

[7] P. Krantz, M. Kjaergaard, F. Yan, T. P. Orlando, S. Gustavsson, and W. D. Oliver. A quantum engineer's guide to superconducting qubits. *Applied Physics Reviews*, 6(2):021318, 2019.

[8] F. Arute, K. Arya, R. Babbush, D. Bacon, J. C. Bardin, R. Barends, R. Biswas, S. Boixo, F. G. S. L. Brandao, D. A. Buell, B. Burkett, Y. Chen, Z. Chen, B. Chiaro, R. Collins, W. Courtney, A. Dunsworth, E. Farhi, B. Foxen, A. Fowler, C. Gidney, M. Giustina, R. Graff, K. Guerin, S. Habegger, M. P. Harrigan, M. J. Hartmann, A. Ho, M. Hoffmann, T. Huang, T. S. Humble, S. V. Isakov, E. Jeffrey, Z. Jiang, D. Kafri, K. Kechedzhi, J. Kelly, P. V. Klimov, S. Knysh, A. Korotkov, F. Kostritsa,

D. Landhuis, M. Lindmark, E. Lucero, D. Lyakh, S. Mandrà, J. R. McClean, M. McEwen, A. Megrant, X. Mi, K. Michielsen, M. Mohseni, J. Mutus, O. Naaman, M. Neeley, C. Neill, M. Y. Niu, E. Ostby, A. Petukhov, J. C. Platt, C. Quintana, E. G. Rieffel, P. Roushan, N. C. Rubin, D. Sank, K. J. Satzinger, V. Smelyanskiy, K. J. Sung, M. D. Trevithick, A. Vainsencher, B. Villalonga, T. White, Z. J. Yao, P. Yeh, A. Zalcman, H. Neven, and J. M. Martinis. Quantum supremacy using a programmable superconducting processor. *Nature*, 574(7779):505–510, 2019.

[9] V. Bouchiat, D. Vion, P. Joyez, D. Esteve, and M. H. Devoret. Quantum coherence with a single Cooper pair. *Physica Scripta*, 1998(T76):165, 1998.

[10] Y. Nakamura, Y. A. Pashkin, and J. S. Tsai. Coherent control of macroscopic quantum states in a single-Cooper-pair box. *Nature*, 398(6730):786–788, 1999.

[11] J. Koch, T. M. Yu, J. Gambetta, A. A. Houck, D. I. Schuster, J. Majer, A. Blais, M. H. Devoret, S. M. Girvin, and R. J. Schoelkopf. Charge-insensitive qubit design derived from the Cooper pair box. *Physical Review A*, 76(4):042319, 2007.

[12] A. Blais, R.-S. Huang, A. Wallraff, S. M. Girvin, and R. J. Schoelkopf. Cavity quantum electrodynamics for superconducting electrical circuits: An architecture for quantum computation. *Physical Review A*, 69(6), 2004.

[13] A. Blais, A. L. Grimsmo, S. M. Girvin, and A. Wallraff. Circuit quantum electrodynamics. *Reviews of Modern Physics*, 93(2):025005, 2021.

[14] M. A. Nielsen and I. L. Chuang. *Quantum Computation and Quantum Information*. 10th anniversary edition, 2010.

[15] I. Siddiqi. Engineering high-coherence superconducting qubits. *Nature Reviews Materials*, 6(10):875–891, 2021.

[16] O. Erlandsson. *Circuit QED Devices for Probing Majorana Zero Modes.* Master's thesis, 2018.

[17] R. Aguado. A perspective on semiconductor-based superconducting qubits. *Applied Physics Letters*, 117(24):240501, 2020.

[18] T. W. Larsen. *Mesoscopic Superconductivity towards Protected Qubits*. PhD thesis, 2018.

[19] A. Kringhøj. *Exploring the Semiconducting Josephson Junction of Nanowire-based Superconducting Qubits*. PhD thesis, 2020.

[20] M. F. Goffman, C. Urbina, H. Pothier, J. Nygård, C. M. Marcus, and P. Krogstrup. Conduction channels of an InAs-Al nanowire Josephson weak link. *New Journal of Physics*, 19(9):092002, 2017.

[21] A. Kringhøj, L. Casparis, M. Hell, T. W. Larsen, F. Kuemmeth, M. Leijnse, K. Flensberg, P. Krogstrup, J. Nygård, K. D. Petersson, and C. M. Marcus. Anharmonicity of a superconducting qubit with a few-mode Josephson junction. *Physical Review B*, 97(6), 2018.

[22] T. W. Larsen, K. D. Petersson, F. Kuemmeth, T. S. Jespersen, P. Krogstrup, J. Nygård, and C. M. Marcus. Semiconductor-Nanowire-Based Superconducting Qubit. *Physical Review Letters*, 115(12), 2015.

[23] G. de Lange, B. van Heck, A. Bruno, D. J. van Woerkom, A. Geresdi, S. R. Plissard, E. P. A. M. Bakkers, A. R. Akhmerov, and L. DiCarlo. Realization of Microwave Quantum Circuits Using Hybrid Superconducting-Semiconducting Nanowire Josephson Elements. *Physical Review Letters*, 115(12), 2015.

[24] L. Casparis, T. W. Larsen, M. S. Olsen, F. Kuemmeth, P. Krogstrup, J. Nygård, K. D. Petersson, and C. M. Marcus. Gatemon Benchmarking and Two-Qubit Operations. *Physical Review Letters*, 116(15):150505, 2016.

[25] F. Luthi, T. Stavenga, O. W. Enzing, A. Bruno, C. Dickel, N. K. Langford, M. A. Rol, T. S. Jespersen, J. Nygård, P. Krogstrup, and L. DiCarlo. Evolution of Nanowire Transmon Qubits and Their Coherence in a Magnetic Field. *Physical Review Letters*, 120(10), 2018.

[26] L. Casparis, M. R. Connolly, M. Kjaergaard, N. J. Pearson, A. Kringhøj, T. W. Larsen, F. Kuemmeth, T. Wang, C. Thomas, S. Gronin, G. C. Gardner, M. J. Manfra, C. M. Marcus, and K. D. Petersson. Superconducting gatemon qubit based on a proximitized two-dimensional electron gas. *Nature Nanotechnology*, 13(10):915–919, 2018.

[27] J. G. Kroll, W. Uilhoorn, K. L. van der Enden, D. de Jong, K. Watanabe, T. Taniguchi, S. Goswami, M. C. Cassidy, and L. P. Kouwenhoven. Magnetic field compatible circuit quantum electrodynamics with graphene Josephson junctions. *Nature Communications*, 9(1):4615, 2018.

[28] L. Casparis, N. J. Pearson, A. Kringhøj, T. W. Larsen, F. Kuemmeth, J. Nygård, P. Krogstrup, K. D. Petersson, and C. M. Marcus. Voltage-controlled superconducting quantum bus. *Physical Review B*, 99(8):085434, 2019.

[29] A. Bargerbos, W. Uilhoorn, C.-K. Yang, P. Krogstrup, L. P. Kouwenhoven, G. de Lange, B. van Heck, and A. Kou. Observation of Vanishing Charge Dispersion of a Nearly Open Superconducting Island. *Physical Review Letters*, 124(24):246802, 2020.

[30] A. Kringhøj, B. van Heck, T. W. Larsen, O. Erlandsson, D. Sabonis, P. Krogstrup, L. Casparis, K. D. Petersson, and C. M. Marcus. Suppressed Charge Dispersion via Resonant Tunneling in a Single-Channel Transmon. *Physical Review Letters*, 124(24):246803, 2020.

[31] T. W. Larsen, M. E. Gershenson, L. Casparis, A. Kringhøj, N. J. Pearson, R. P. G. McNeil, F. Kuemmeth, P. Krogstrup, K. D. Petersson, and C. M. Marcus. Parity-Protected Superconductor-Semiconductor Qubit. *Physical Review Letters*, 125(5):056801, 2020.

[32] A. Kringhøj, T. W. Larsen, B. van Heck, D. Sabonis, O. Erlandsson, I. Petkovic, D. I. Pikulin, P. Krogstrup, K. D. Petersson, and C. M. Marcus. Controlled dc Monitoring of a Superconducting Qubit. *Physical Review Letters*, 124(5):056801, 2020.

[33] A. Kringhøj, T. W. Larsen, O. Erlandsson, W. Uilhoorn, J. G. Kroll, M. Hesselberg, R. P. G. McNeil, P. Krogstrup, L. Casparis, C. M. Marcus, and K. D. Petersson. Magnetic-Field-Compatible Superconducting Transmon Qubit. *Physical Review Applied*, 15(5):054001, 2021.

[34] M. Hays, G. de Lange, K. Serniak, D. J. van Woerkom, D. Bouman, P. Krogstrup, J. Nygård, A. Geresdi, and M. H. Devoret. Direct Microwave Measurement of Andreev-Bound-State Dynamics in a Semiconductor-Nanowire Josephson Junction. *Physical Review Letters*, 121(4):047001, 2018.

[35] L. Tosi, C. Metzger, M. F. Goffman, C. Urbina, H. Pothier, S. Park, A. L. Yeyati, J. Nygård, and P. Krogstrup. Spin-Orbit Splitting of Andreev States Revealed by Microwave Spectroscopy. *Physical Review X*, 9(1), 2019.

[36] M. Hays, V. Fatemi, K. Serniak, D. Bouman, S. Diamond, G. de Lange, P. Krogstrup, J. Nygård, A. Geresdi, and M. H. Devoret. Continuous monitoring of a trapped superconducting spin. *Nature Physics*, 16(11):1103–1107, 2020.

[37] M. Kjaergaard, M. E. Schwartz, J. Braumüller, P. Krantz, J. I.-J. Wang, S. Gustavsson, and W. D. Oliver. Superconducting Qubits: Current State of Play. *Annual Review of Condensed Matter Physics*, 11(1):369–395, 2020.

[38] M. Leijnse and K. Flensberg. Introduction to topological superconductivity and Majorana fermions. *Semiconductor Science and Technology*, 27(12):124003, 2012.

[39] R. M. Lutchyn, E. P. A. M. Bakkers, L. P. Kouwenhoven, P. Krogstrup, C. M. Marcus, and Y. Oreg. Majorana zero modes in superconductor–semiconductor heterostructures. *Nature Reviews Materials*, 3(5):52–68, 2018.

[40] A. Y. Kitaev. Unpaired Majorana fermions in quantum wires. *Physics-Uspekhi*, 44(10S):131–136, 2001.

[41] R. M. Lutchyn, J. D. Sau, and S. Das Sarma. Majorana Fermions and a Topological Phase Transition in Semiconductor-Superconductor Heterostructures. *Physical Review Letters*, 105(7):077001, 2010.

[42] Y. Oreg, G. Refael, and F. von Oppen. Helical Liquids and Majorana Bound States in Quantum Wires. *Physical Review Letters*, 105(17):177002, 2010.

[43] V. Mourik, K. Zuo, S. M. Frolov, S. R. Plissard, E. P. A. M. Bakkers, and L. P. Kouwenhoven. Signatures of Majorana Fermions in Hybrid Superconductor-Semiconductor Nanowire Devices. *Science*, 336(6084):1003–1007, 2012.

[44] M. T. Deng, S. Vaitiekėnas, E. B. Hansen, J. Danon, M. Leijnse, K. Flensberg, J. Nygård, P. Krogstrup, and C. M. Marcus. Majorana bound state in a

coupled quantum-dot hybrid-nanowire system. *Science*, 354(6319):1557–1562, 2016.

[45] S. Vaitiekėnas, G. W. Winkler, B. van Heck, T. Karzig, M.-T. Deng, K. Flensberg, L. I. Glazman, C. Nayak, P. Krogstrup, R. M. Lutchyn, and C. M. Marcus. Flux-induced topological superconductivity in full-shell nanowires. *Science*, 367(6485):eaav3392, 2020.

[46] C. Ohm and F. Hassler. Microwave readout of Majorana qubits. *Physical Review B*, 91(8):085406, 2015.

[47] F. Hassler, A. R. Akhmerov, and C. W. J. Beenakker. The top-transmon: A hybrid superconducting qubit for parity-protected quantum computation. *New Journal of Physics*, 13(9):095004, 2011.

[48] T. Hyart, B. van Heck, I. C. Fulga, M. Burrello, A. R. Akhmerov, and C. W. J. Beenakker. Flux-controlled quantum computation with Majorana fermions. *Physical Review B*, 88(3):035121, 2013.

[49] E. Ginossar and E. Grosfeld. Microwave transitions as a signature of coherent parity mixing effects in the Majorana-transmon qubit. *Nature Communications*, 5(1), 2014.

[50] K. Yavilberg, E. Ginossar, and E. Grosfeld. Fermion parity measurement and control in Majorana circuit quantum electrodynamics. *Physical Review B*, 92(7):075143, 2015.

[51] J. Ávila, E. Prada, P. San-Jose, and R. Aguado. Majorana oscillations and parity crossings in semiconductor nanowire-based transmon qubits. *Physical Review Research*, 2(3):033493, 2020.

[52] P. Krogstrup, N. L. B. Ziino, W. Chang, S. M. Albrecht, M. H. Madsen, E. Johnson, J. Nygård, C. M. Marcus, and T. S. Jespersen. Epitaxy of semiconductor–superconductor nanowires. *Nature Materials*, 14(4):400–406, 2015.

[53] S. A. Khan, C. Lampadaris, A. Cui, L. Stampfer, Y. Liu, S. J. Pauka, M. E. Cachaza, E. M. Fiordaliso, J.-H. Kang, S. Korneychuk, T. Mutas, J. E. Sestoft, F. Krizek, R. Tanta, M. C. Cassidy, T. S. Jespersen, and P. Krogstrup. Transparent Gatable Superconducting Shadow Junctions, 2020.

[54] Davies. *The Physics of Low-dimensional Semiconductors An Introduction*. 1998.

[55] B. J. van Wees, H. van Houten, C. W. J. Beenakker, J. G. Williamson, L. P. Kouwenhoven, D. van der Marel, and C. T. Foxon. Quantized conductance of point contacts in a two-dimensional electron gas. *Physical Review Letters*, 60(9):848–850, 1988.

[56] F. Pobell. *Matter and Methods at Low Temperatures*. Third, revised and expanded edition, 2007.

[57] A. Danilenko, D. Sabonis, G. W. Winkler, O. Erlandsson, P. Krogstrup, and C. M. Marcus. Few-mode to mesoscopic junctions in gatemon qubits. *arXiv:2209.03688*, 2022.

[58] D. Laroche, D. Bouman, D. J. van Woerkom, A. Proutski, C. Murthy, D. I. Pikulin, C. Nayak, R. J. J. van Gulik, J. Nygård, P. Krogstrup, L. P. Kouwenhoven, and A. Geresdi. Observation of the 4π-periodic Josephson effect in indium arsenide nanowires. *Nature Communications*, 10(1):245, 2019.

[59] K. Zuo, V. Mourik, D. B. Szombati, B. Nijholt, D. J. van Woerkom, A. Geresdi, J. Chen, V. P. Ostroukh, A. R. Akhmerov, S. R. Plissard, D. Car, E. P. A. M. Bakkers, D. I. Pikulin, L. P. Kouwenhoven, and S. M. Frolov. Supercurrent Interference in Few-Mode Nanowire Josephson Junctions. *Physical Review Letters*, 119(18):187704, 2017.

[60] W. A. Little and R. D. Parks. Observation of Quantum Periodicity in the Transition Temperature of a Superconducting Cylinder. *Physical Review Letters*, 9(1):9–12, 1962.

[61] Y. Liu, Y. Zadorozhny, M. M. Rosario, B. Y. Rock, P. T. Carrigan, and H. Wang. Destruction of the Global Phase Coherence in Ultrathin, Doubly Connected Superconducting Cylinders. *Science*, 294(5550):2332–2334, 2001.

[62] M. Tinkham. *Introduction to Superconductivity*. Second edition, 1996.

[63] I. Sternfeld, E. Levy, M. Eshkol, A. Tsukernik, M. Karpovski, H. Shtrikman, A. Kretinin, and A. Palevski. Magnetoresistance Oscillations of

Superconducting Al-Film Cylinders Covering InAs Nanowires below the Quantum Critical Point. *Physical Review Letters*, 107(3):037001, 2011.

[64] S. Vaitiekėnas, P. Krogstrup, and C. M. Marcus. Anomalous metallic phase in tunable destructive superconductors. *Physical Review B*, 101(6):060507, 2020.

[65] V. H. Dao and L. F. Chibotaru. Destruction of global coherence in long superconducting nanocylinders. *Physical Review B*, 79(13):134524, 2009.

[66] A. I. Larkin. Superconductor of Small Dimensions in a Strong Magnetic Field. 1965.

[67] A. Keselman, C. Murthy, B. van Heck, and B. Bauer. Spectral response of Josephson junctions with low-energy quasiparticles. *SciPost Physics*, 7(4):050, 2019.

[68] D. M. T. van Zanten, D. Sabonis, J. Suter, J. I. Väyrynen, T. Karzig, D. I. Pikulin, E. C. T. O'Farrell, D. Razmadze, K. D. Petersson, P. Krogstrup, and C. M. Marcus. Photon-assisted tunnelling of zero modes in a Majorana wire. *Nature Physics*, 16(6):663–668, 2020.

[69] J. Ávila, E. Prada, P. San-Jose, and R. Aguado. Superconducting islands with topological Josephson junctions based on semiconductor nanowires. *Physical Review B*, 102(9):094518, 2020.

[70] J. A. Schreier, A. A. Houck, J. Koch, D. I. Schuster, B. R. Johnson, J. M. Chow, J. M. Gambetta, J. Majer, L. Frunzio, M. H. Devoret, S. M. Girvin, and R. J. Schoelkopf. Suppressing charge noise decoherence in superconducting charge qubits. *Physical Review B*, 77(18), 2008.

[71] J. Kroll, F. Borsoi, K. van der Enden, W. Uilhoorn, D. de Jong, M. Quintero-Pérez, D. van Woerkom, A. Bruno, S. Plissard, D. Car, E. Bakkers, M. Cassidy, and L. Kouwenhoven. Magnetic-Field-Resilient Superconducting Coplanar-Waveguide Resonators for Hybrid Circuit Quantum Electrodynamics Experiments. *Physical Review Applied*, 11(6):064053, 2019.

[72] A. Kringhøj, G. W. Winkler, T. W. Larsen, D. Sabonis, O. Erlandsson, P. Krogstrup, B. van Heck, K. D. Petersson, and C. M. Marcus. Andreev

Modes from Phase Winding in a Full-Shell Nanowire-Based Transmon. *Physical Review Letters*, 126(4):047701, 2021.

[73] D. Sabonis, O. Erlandsson, A. Kringhøj, B. van Heck, T. W. Larsen, I. Petkovic, P. Krogstrup, K. D. Petersson, and C. M. Marcus. Destructive Little-Parks Effect in a Full-Shell Nanowire-Based Transmon. *Physical Review Letters*, 125(15):156804, 2020.

[74] K. Serniak, M. Hays, G. de Lange, S. Diamond, S. Shankar, L. D. Burkhart, L. Frunzio, M. Houzet, and M. H. Devoret. Hot Nonequilibrium Quasiparticles in Transmon Qubits. *Physical Review Letters*, 121(15), 2018.

[75] D. Ristè, C. C. Bultink, M. J. Tiggelman, R. N. Schouten, K. W. Lehnert, and L. DiCarlo. Millisecond charge-parity fluctuations and induced decoherence in a superconducting transmon qubit. *Nature Communications*, 4(1), 2013.

[76] K. Serniak, S. Diamond, M. Hays, V. Fatemi, S. Shankar, L. Frunzio, R. Schoelkopf, and M. Devoret. Direct Dispersive Monitoring of Charge Parity in Offset-Charge-Sensitive Transmons. *Physical Review Applied*, 12(1):014052, 2019.

[77] R. T. Gordon, C. E. Murray, C. Kurter, M. Sandberg, S. A. Hall, K. Balakrishnan, R. Shelby, B. Wacaser, A. A. Stabile, J. W. Sleight, M. Brink, M. B. Rothwell, K. P. Rodbell, O. Dial, and M. Steffen. Environmental radiation impact on lifetimes and quasiparticle tunneling rates of fixed-frequency transmon qubits. *Applied Physics Letters*, 120(7):074002, 2022.

[78] C. Kurter, C. E. Murray, R. T. Gordon, B. B. Wymore, M. Sandberg, R. M. Shelby, A. Eddins, V. P. Adiga, A. D. K. Finck, E. Rivera, A. A. Stabile, B. Trimm, B. Wacaser, K. Balakrishnan, A. Pyzyna, J. Sleight, M. Steffen, and K. Rodbell. Quasiparticle tunneling as a probe of Josephson junction barrier and capacitor material in superconducting qubits. *npj Quantum Information*, 8(1):31, 2022.

[79] X. Pan, Y. Zhou, H. Yuan, L. Nie, W. Wei, L. Zhang, J. Li, S. Liu, Z. H. Jiang, G. Catelani, L. Hu, F. Yan, and D. Yu. Engineering superconducting qubits to reduce quasiparticles and charge noise. *Nature Communications*, 13(1):7196, 2022.

[80] S. Gustavsson, F. Yan, G. Catelani, J. Bylander, A. Kamal, J. Birenbaum, D. Hover, D. Rosenberg, G. Samach, A. P. Sears, S. J. Weber, J. L. Yoder, J. Clarke, A. J. Kerman, F. Yoshihara, Y. Nakamura, T. P. Orlando, and W. D. Oliver. Suppressing relaxation in superconducting qubits by quasiparticle pumping. *Science*, 354(6319):1573–1577, 2016.

[81] U. Vool, I. M. Pop, K. Sliwa, B. Abdo, C. Wang, T. Brecht, Y. Y. Gao, S. Shankar, M. Hatridge, G. Catelani, M. Mirrahimi, L. Frunzio, R. J. Schoelkopf, L. I. Glazman, and M. H. Devoret. Non-Poissonian Quantum Jumps of a Fluxonium Qubit due to Quasiparticle Excitations. *Physical Review Letters*, 113(24):247001, 2014.

[82] C. Wang, Y. Y. Gao, I. M. Pop, U. Vool, C. Axline, T. Brecht, R. W. Heeres, L. Frunzio, M. H. Devoret, G. Catelani, L. I. Glazman, and R. J. Schoelkopf. Measurement and control of quasiparticle dynamics in a superconducting qubit. *Nature Communications*, 5(1), 2014.

[83] U. Patel, I. V. Pechenezhskiy, B. L. T. Plourde, M. G. Vavilov, and R. McDermott. Phonon-Mediated Quasiparticle Poisoning of Superconducting Microwave Resonators. *Physical Review B*, 96(22):220501, 2017.

[84] W. Uilhoorn, J. G. Kroll, A. Bargerbos, S. D. Nabi, C.-K. Yang, P. Krogstrup, L. P. Kouwenhoven, A. Kou, and G. de Lange. Quasiparticle trapping by orbital effect in a hybrid superconducting-semiconducting circuit. *arXiv:2105.11038*, 2021.

[85] J. J. Wesdorp, L. Grünhaupt, A. Vaartjes, M. Pita-Vidal, A. Bargerbos, L. J. Splitthoff, P. Krogstrup, B. van Heck, and G. de Lange. Dynamical polarization of the fermion parity in a nanowire Josephson junction. *arXiv:2112.01936*, 2021.

[86] G. Catelani, R. J. Schoelkopf, M. H. Devoret, and L. I. Glazman. Relaxation and frequency shifts induced by quasiparticles in superconducting qubits. *Physical Review B*, 84(6):064517, 2011.

[87] W. Chang, S. M. Albrecht, T. S. Jespersen, F. Kuemmeth, P. Krogstrup, J. Nygård, and C. M. Marcus. Hard gap in epitaxial semiconductor–superconductor nanowires. *Nature Nanotechnology*, 10(3):232–236, 2015.

[88] D. I. Schuster. *Circuit Quantum Electrodynamics*. PhD thesis, 2007.

[89] S. Budtz. *Circuit Quantum Electrodynamics of a Two-dimensional Electron Gas Based Gatemon Qubit Hosting a Quantum Dot.* Master's thesis, 2022.

[90] A. Bargerbos, M. Pita-Vidal, R. Žitko, J. Ávila, L. J. Splitthoff, L. Grünhaupt, J. J. Wesdorp, C. K. Andersen, Y. Liu, L. P. Kouwenhoven, R. Aguado, A. Kou, and B. van Heck. Singlet-doublet transitions of a quantum dot Josephson junction detected in a transmon circuit. *arXiv:2202.12754*, 2022.

[91] C. W. J. Beenakker and H. van Houten. Josephson current through a superconducting quantum point contact shorter than the coherence length. *Physical Review Letters*, 66(23):3056–3059, 1991.

[92] C. W. J. Beenakker and H. van Houten. Resonant Josephson Current Through a Quantum Dot. In K. von Klitzing, I. P. Kaminov, W. Engl, T. Sugano, H. K. V. Lotsch, H. Koch, and H. Lübbig, editors, *Single-Electron Tunneling and Mesoscopic Devices*, volume 31, pages 175–179. Springer Berlin Heidelberg, Berlin, Heidelberg, 1992.

[93] P. Jarillo-Herrero, J. A. van Dam, and L. P. Kouwenhoven. Quantum supercurrent transistors in carbon nanotubes. *Nature*, 439(7079):953–956, 2006.

[94] D. V. Averin. Coulomb Blockade in Superconducting Quantum Point Contacts. *Physical Review Letters*, 82(18):4, 1999.